XMM-Newton Survey Of The Magellanic Bridge

Ryan Le Roux

Supervisors: Lee Townsend, Vanessa McBride, Patrick Woudt

September 8, 2020

Contents

Abstract

We aim to characterise the X-ray binary population as a function of the local stellar population (in terms of age, metallicity, and stellar density) in the Magellanic Bridge, the interconnecting region between the Small and Large Magellanic Cloud. Gardiner and Noguchi (1996) suggest that closest approach between Small and Large Magellanic Cloud, as evidenced by dramatic phase shift in star formation, occurred approximately 200 Myr ago. During the approach, gas had been tidally stripped (most likely from the Small Magellanic Cloud) into the interconnecting Bridge. According to models of star formation history (Harris, 2007), alongside optical surveys of the Bridge (Skowron et al., 2014), there is strong evidence to suggest that the young, low metallicity stellar population formed *in situ*, rather than being tidally stripped from either Magellanic Cloud. Three fields located near the Western Bridge observed by Harris (2007) were also observed with the XMM-Newton. Cross-matching between optical and X-ray sources was performed, and any interesting matches were followed up with spectroscopic analysis, using the 1.9 m telescope located in Sutherland. A Be/X-ray Binary (BeXRB) candidate is discussed, and if confirmed, will be the furthest known BeXRB from the SMC.

Acknowledgements

I would like to thank my supervisors, Dr. Lee Townsend and Assoc. Prof. Vanessa McBride, for their continuous support, assistance and feedback. Dr. Lee Townsend organised an observing trip at the South African Astronomical Observatory 1.9 m spectrograph, which constitutes a significant portion of this work. Assoc. Prof. Vanessa McBride acquired funding for said trip. They have always been willing to assist me despite their own workload.

Prof. Patrick Woudt has helped immensely with administrative issues, and I am grateful that he has always assisted in that regard.

I would also like to thank Dr. David Buckley, the South African Gamma-Ray Astronomy Programme and Dr. Retha Pretorius for sponsoring my trip to the X-ray conference in Bologna, Italy, where I had the opportunity to present this work.

To my family and Jeanne, thank you for all your love, emotional and financial support throughout my academic career. I would not be where I am without them.

Chapter 1

Introduction

1.1 Magellanic Clouds

The Large and Small Magellanic Clouds (LMC and SMC, respectively) are satellite galaxies located between 50 - 60 kpc from the Milky Way (Pietrzyński et al., 2013; Hilditch et al., 2005). Their close proximity allow for the observation of resolvable sources. Both galaxies are located in the Southern Celestial Hemisphere, and lie outside of the Galactic plane, meaning observations are less affected by Galactic extinction. Although the close proximity allows for the study of resolvable objects, the large area of sky occupied by both Magellanic Clouds make it difficult and time consuming to complete full multi-wavelength observations.

Although both galaxies appear to be irregular, they contain a bar structure with a single spiral arm. This led to form an additional morphology of galaxies called the Magellanic spiral, for which the LMC is a prototype of this class (de Vaucouleurs and Freeman, 1972). Since the Magellanic Clouds are tidally interacting with each other, as well as the Milky Way (MW), this may have led them to become distorted, barred spiral galaxies. Pardy et al. (2016) show that the bar and photometric centre become mismatched due to gravitational interactions with neighbouring dwarf galaxies, which take

several billion years to realign.

The mass of the LMC is difficult to constrain using its rotation curve, since there is a dispute over the extent of the radial curve that should be included in the calculation. Both Meatheringham et al. (1988) and Schommer et al. (1992) obtain the same rotation velocities, but arrive at different masses due to differing radii used in their calculations (with masses of 3×10^8 $M_\odot$ and 1.5×10^{10} $M_\odot$, respectively). A study on the perturbations of stars in the Orphan stream (a tidal stream of stars located in the Galactic Halo) yielded a more accurate mass of $1.38^{+0.27}_{-0.24} \times 10^{11}$ $M_\odot$ (Erkal et al., 2019).

StarFISH is an algorithm used for creating synthetic colour-magnitude diagrams in order to fit isochrones to photometric data. This algorithm was developed and used by Harris and Zaritsky (2009) to study the star formation history of the LMC using data from the Magellanic Clouds Photometric Survey (MCPS). They found that prior to 12 Gyr ago, there was a burst of star formation. Between 12 - 5 Gyr ago, there was a quiescent phase, which was followed by a regular star formation rate of 0.2 $M_\odot$/yr. It is suggested that the quiescent phase ended after an interaction occurred between the Magellanic Clouds, as evidenced by an increase in star formation in the SMC around the same time. There have been several star burst epochs since then, most notably around 2 - 0.5 Gyr ago, where there appears to be star bursts in the SMC around the same time, and may be a result of gravitational interactions between the Magellanic Clouds and the Milky Way.

The mass of the SMC has also been difficult to determine, due to a dark matter halo which has the majority of its mass lying beyond the optical radius of the galaxy (Bekki and Stanimirović, 2009). The authors suggest that the initial dark matter halo has a mass of $\sim 6.5 \times 10^9$ $M_\odot$ with a core radius of $r_0 \sim 3.2$ kpc, and that the stellar mass-to-light ratio (in the V-band) is $M_s/L_V \sim 2 - 4$. However, a larger stellar mass-to-light implies that younger stellar populations do not dominate the mass of the SMC. Further evidence of this can be found by Harris and Zaritsky (2004), who showed that

approximately half of the stellar populations were formed before 8.4 Gyr ago.

There also appeared to be a very low star formation rate between 8.4 - 3 Gyr ago, and since then there has been a rise in the mean star formation rate, alongside three star burst episodes. These episodes occurred 2.5, 0.4, and 0.06 Gyr ago, the first two episodes coinciding with the previous closest approaches of the SMC with the MW.

Using the Magellanic Cloud Photometric Survey (MCPS) and Optical Gravitational Lensing Experiment (OGLE III) surveys, Choudhury et al. (2016, 2018) estimated the average metallicity of the Magellanic Clouds (MCs). The estimated metallicity from MCPS and OGLE III of the LMC are found to be [Fe/H] = -0.37 ± 0.12 dex and [Fe/H] = -0.39 ± 0.10 dex, respectively (Choudhury et al., 2016). Similarly, the estimated metallicity from MCPS and OGLE III of the SMC are found to be [Fe/H] = -0.94 ± 0.09 dex and [Fe/H] = -0.95 ± 0.08, respectively (Choudhury et al., 2018). From these values, it can be seen that the SMC is more metal poor than the LMC. For reference, several galaxies in the Local Group have metallicities around [Fe/H] $\sim$ -0.5 to -2 (McConnachie et al., 2005), thus the SMC is not as metal poor as other local galaxies. Regardless, the resolvability of sources allows for studying the evolution of metal poor galaxies.

A thorough X-ray point-source catalogue of the SMC was compiled by Sturm et al. (2013), using the XMM-Newton telescope. It covers a 5.6 $\deg^2$ area of the sky, in the 0.2 keV to 12 keV range. The Science Analysis System software (European Space Agency, a) was used in order to search for point sources using maximum-likelihood techniques. In this paper, a total of 3053 unique X-ray sources are obtained from observations, with a median position uncertainty of 1.3″, and a lower flux limit of approximately 10^{-14} erg cm^{-2} s^{-1} in the 0.2 - 4.5 keV range. The sources detected are high-mass X-ray binaries (HMXBs), super-soft sources (SSS), active galactic nuclei (AGN) and foreground stars in the MW. These sources were identified using their hardness ratios (HR, a ratio of the energy output in different bands) and

time variability.

A 'first light' X-ray survey of the LMC was performed by Trümper et al. (1991) using the Röntgen Observatory Satellite (ROSAT), which contained various astrophysical systems, such as supernova remnants (SNR), X-ray binaries, and a cluster of hot stars. A more recent survey by Grebenev et al. (2013) was performed on the LMC, which looked at the hard X-ray band using the INTEGRAL observatory. A long, 7 Ms exposure allowed for the detection of 21 sources. Ten of these sources belong to the LMC, which are comprised of 7 HMXBs, 2 pulsars and 1 low-mass X-ray binary. The rest of the sources belong to either the SMC and Milky Way, with the rest located beyond the Local Group.

1.2 Magellanic Bridge

1.2.1 Interaction Between Magellanic Clouds

The Magellanic Bridge is a region between the SMC and LMC, which contains a gaseous and stellar component. The gaseous component was first discovered by Hindman et al. (1963) through H_I radio observations, and the stellar component was first observed by Irwin et al. (1985).

Computer simulations by Gardiner and Noguchi (1996) suggest that a close encounter between the Clouds occurred 200 Myr ago, which allowed the gaseous component of the Bridge to form via minor galactic interactions. The stellar component, however, is believed to have formed *in situ*, meaning the stellar component formed from tidally-stripped gas. If stars were stripped from either Cloud, their age should match the age distribution of their host galaxy. Both Magellanic Clouds show a dominant red giant branch and red clump horizontal branch in their colour-magnitude diagrams (Harris, 2007), which would thus be tracers for these tidally-stripped stars. However, the stars observed in the Bridge are young blue-type stars (Skowron et al., 2014).

A uniformly sampled photometric survey of the Bridge by Harris (2007)

revealed that the region contains a young stellar population that was formed 200 - 300 Myr ago and that continual star formation occurred up until 40 Myr ago. Any older stars observed in these fields were found to belong to the halo of either Clouds.

Dwarf galaxies have been found to have H_I extend two to three times beyond their stellar component, and since the LMC is ten times greater in mass than the SMC, this may explain why a weak gravitational force was able to tidally-strip the gas from the SMC, while leaving any stars from either Cloud only slightly perturbed. The tidal interactions between the Large and Small Magellanic Clouds may have induced star formation long after the initial formation of the Bridge.

1.2.2 Star Formation In Magellanic Bridge

Evidence for recent star formation can be found in OB associations, which are blue giants of spectral class O and B. Approximately 100 OB associations were discovered in the western Bridge (closest to SMC) by Bica and Schmitt (1995). Since the lifetime of these objects is much less than the last close approach between both Clouds (200 Myr ago), they would have had to be formed recently. Thus, the existence of molecular clouds (discovered by Mizuno et al., 2006) supports the idea of ongoing star formation in the Bridge.

In the fields observed by Harris (2007), the stellar component age was determined by matching the color-magnitude of the observed stars to theoretical isochrones. In one field observed near the SMC, prolonged star formation occurred approximately 300 - 80 Myr ago, and in another region star formation occurred on a shorter timescale, between 100 - 200 Myr ago. Some fields were sparsely populated, thus determining a constraint on their age was difficult.

Further detailed observations of the Bridge were performed by OGLE. A spatial density map can be found in figure 1.1. Observations covering 270

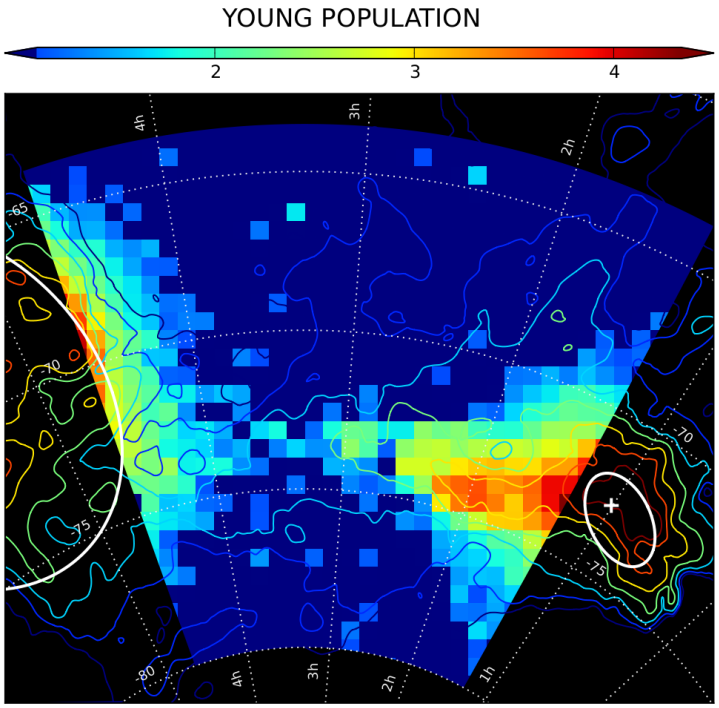

Figure 1.1: Young stellar spatial density map of the LMC (left), SMC (right) and Bridge (center). Each pixel shown is calculated as *log*(stars/area [square degree]), illustrated by the bar above the figure. Contours represent the H_I density (Skowron et al., 2014).

deg^2 of the Magellanic Bridge area confirmed that a young stellar population forms a continuous bridge between the LMC and SMC. This confirms previous studies (such as Harris, 2007) that have shown a young population in the western Bridge (closer to the SMC), however the density map shows that there is also a young population in the center and eastern Bridge (LMC side), which was previously not well studied. The young population observed by OGLE is defined as younger than 1 Gyr (Skowron et al., 2014, see pg. 8), where detections greater than 2σ were plotted in figure 1.1.

1.3 X-ray Astronomy

X-rays are high energy photons with wavelengths of the order of several nanometers to subnanometers. They are more commonly referred to by their energies, which range from a hundred electron volts (eV) to 100 keV.

The first paper published on X-rays was written by Röntgen (1896), which details the effects of X-rays on a barium platinocyanide coated paper. The medical benefit of X-rays was shortly discovered after Röntgen created an image of his wife's hand on a photographic plate. Since the atmosphere is opaque to X-ray radiation, observations of X-ray sources were only possible once rocket flights began.

Half a decade after Röntgen's discovery, solar X-rays were studied by using V-2 sounding rockets containing a scientific payload (several missions were conducted from 1958 onward; Frederick et al., 1966). It was only in 1962 that an extrasolar X-ray was detected during one of these missions, a source located in the Scorpius constellation, named Scorpious X-1 (Giacconi et al., 1962), subsequently discovered to be an X-ray binary with an accreting neutron star. This was done using large area Geiger counters placed on an Aerobee rocket (an unguided, suborbital rocket; Wade, 1997-2019). These missions only allow for short period observations ($\sim$5 minutes), therefore it is better to create an instrumental payload that stays beyond Earth's atmosphere for extended periods of time, such as a satellite.

X-ray satellite telescopes are thus better options for long term monitoring missions. One well known X-ray telescope is the XMM-Newton (European Space Agency, f), which launched in late-1999, initially set out to operate for 2 years, it has been operational since then, and its conclusion is subject to a mid-term review in mid-2020 (European Space Agency, h).

1.4 XMM-Newton

XMM-Newton is an X-ray and optical/UV telescope created by the European Space Agency (ESA) and launched on the 10th of December 1999 (European Space Agency, h). It is a 3.8 tonne telescope that is on an elliptical orbit around Earth, this allows for observations to occur without the interference of the van Allen Belt. A sketch of XMM-Newton is shown in figure 1.2.

XMM-Newton is equipped with three European Photon Imagining Camera (EPIC) CCD arrays, two Reflection Grating Spectrometers (RGS) and an Optical Monitor (OM). The EPIC CCD arrays are used for X-ray photometry and provide moderate resolution spectroscopy. The RGS provides high resolution X-ray spectroscopy and spectro-photometry. The OM is used for optical/UV imaging and low resolution spectroscopy. EPIC and RGS are located in the focal plane of XMM-Newton, whereas OM is housed separately.

Concentrically placed mirrors (called X-ray mirror modules) at the entrance of the telescope are required to focus the X-ray photons. Unlike conventional mirrors used to focus light in IR and optical astronomy, X-ray photons need to be slightly deflected by the use of these shells to a focal point, since they can only be reflected at very high incidence angles. XMM-Newton makes use of a paraboloid shaped mirror module at the entrance, followed by a hyperboloid shaped mirror module placed immediately after. The placement of the second mirror module allows for further deflection of X-ray photons, shortening the focal length (and therefore shortening the length needed of XMM-Newton).

1.4.1 European Photon Imaging Camera

There are two different types of EPIC CCD arrays: Metal Oxide Semiconductor (MOS) and PN cameras. In XMM-Newton, two of the EPIC arrays are MOS, and the other is PN. The ‘PN’ refers to the implanted junction semiconductor technology used in its production (Lumb et al., 2012, see

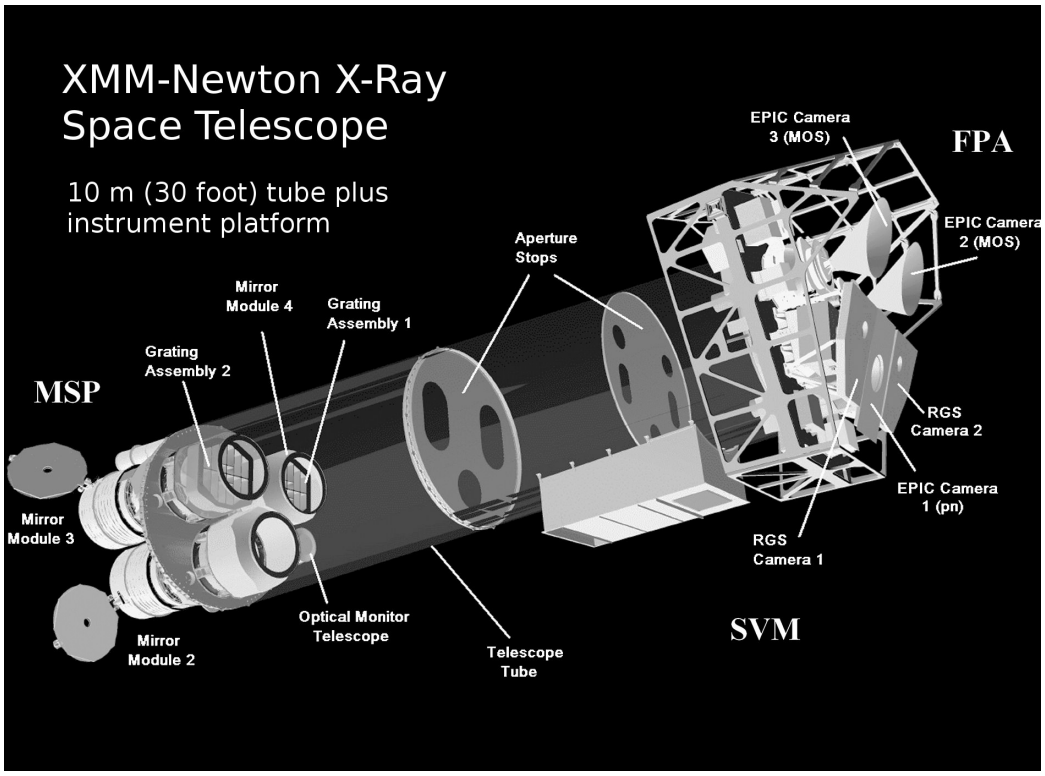

Figure 1.2: A sketch of XMM-Newton, displaying internal instruments. Three mirror modules are located in the bottom right, two are equipped with Reflection Grating Arrays. The EPIC MOS and PN cameras are found on the right hand side. Illustration Credit: ESA/XMM-Newton.

pg. 2).

The EPIC cameras have a relatively large field of view (approximately $30'$) in the 0.15 - 15 keV range, with a spectral resolution of $E/\Delta E$ between 20-50 (Lumb et al., 2012, see pg. 5).

Both camera types allow for imaging between 0.2-12 keV, with the quantum efficiency (QE) of the MOS array averaging 50% and tapering off at low and high energies, and the PN array averaging 90%, both shown in figure 1.3.

The angular resolution of the EPIC CCDs are determined by the X-ray point spread function (PSF) of the mirror modules. This is essentially the quality of focusing X-ray photons by the mirror module. For the mirror modules within XMM-Newton, the PSF is narrow over the energy range 0.1 - 6 keV, and becomes only slightly energy dependent for energies > 6 keV. Given the pixel size of the MOS CCDs (40 μm) and focal length of the telescope (7.5 m), the Nyquist theorem allows for the images to be fully sampled. The pixel size of the PN CCDs is 150 μm, and by Nyquist theorem, images are undersampled (larger pixel size has a lower resolution than the resolution of the telescope).

There are two different types of background that interfere with the onboard instruments, these are the cosmic X-ray background and the instrumental background. Factors that contribute to the cosmic X-ray background are low energy photons from the stellar background, higher energy photons from unresolved objects, and solar wind. Factors that contribute to instrumental background are the usual CCD noise, such as readout noise and hot pixels, but also external high energy particles that are able to penetrate the satellite and interfere with the internal components, i.e. cosmic rays.

Further efforts are required when dealing with cosmic rays, this is done in the form of event grade selection. It is common that X-rays and cosmic rays may be detected in multiple neighbouring pixels. It is the instrumental software that is required to distinguish between a genuine X-ray signal and

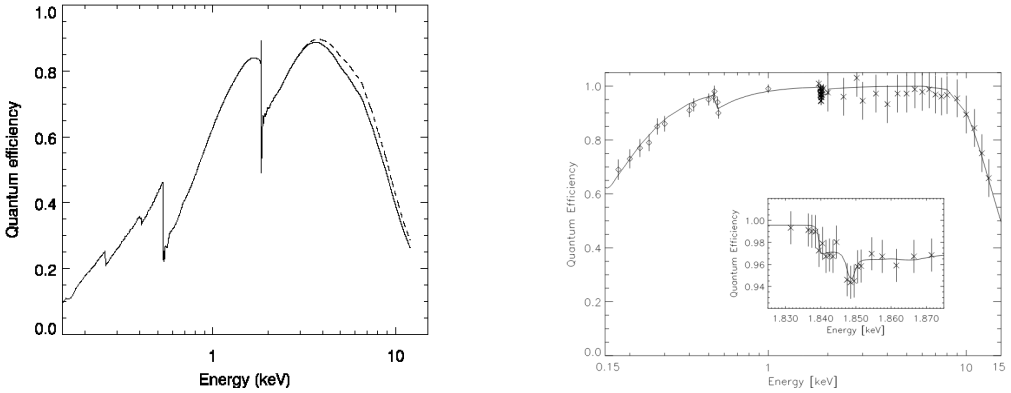

Figure 1.3: Quantum efficiency (QE) as a function of energy for the EPIC MOS (left) and EPIC PN (right) CCD array. The solid and dashed lines for the MOS array represent the QE of the central MOS chip in MOS1 and MOS2, respectively.

a cosmic ray. Genuine X-ray signals are generally detected in either a single pixel (single event) or are spread into two neighbouring pixels (double event; Grant, 2007). Cosmic rays may be detected on two or more neighbouring pixels, these are double, triple, quadruple and higher, (XMM-Newton Science Operations Centre, a). When reducing data, it is possible to select single and/or double events only, and discard any cosmic rays that are detected as triple, quadruple or higher events.

1.5 X-ray Survey of the Magellanic Bridge

The aim of this project is to observe regions of the Magellanic Bridge using the XMM-Newton, in fields where photometric data (Harris, 2007) are available, and to characterise recent star formation through tracers, such as HMXBs and SNR. Similar data may then be used for potential large-scale observations of the rest of the Bridge. The timing and spectral modes on the XMM-Newton allow for the rudimentary classifications of sources, and mark interesting sources for rigorous follow-up studies in all wavebands. In

low source-count cases, hardness ratios may still be deduced from Bayesian estimations (Park et al., 2006).

Available photometric data of the Bridge, alongside neutral hydrogen data (Putman et al., 2003) can be used to determine if the X-ray binary population follows the gas density in the western wing of the Magellanic Bridge (MB), this result can determine whether a wider survey should be conducted to search for an X-ray binary population eastwards.

Diffuse X-ray regions of OB associations and SNRs are other interesting sources to study, notably SNRs. Since the distance to the MB is known within a 20% error, the size of a SNR may be used as an age estimation, and thus may be interpreted in the context of Hα nebulosity in these regions (Muller and Parker, 2007).

Using XMM-Newton for Surveying the Bridge

Three fields close to the SMC (coinciding with Harris, 2007) were observed for 30 ks per field. X-ray binaries in the SMC achieve luminosities of $\sim 10^{37}$ erg s^{-1} in the 2 - 10 keV range during outburst (Haberl and Sturm, 2016). Taking the distance into account, this can be converted to a flux of 3×10^{-12} erg cm^{-2} s^{-1}. Assuming a photon index of 1.5 and neutral hydrogen density of 6×10^{20} cm^{-2}, will result in an estimated count rate on the EPIC MOS and PN cameras as 0.2 - 0.5 counts per second in the 0.5 - 10 keV band, respectively. Using full frame mode, these rates do not approach the levels required for pile-up to occur (XMM-Newton Science Operations Centre, b). With the given exposure time, XMM-Newton is able to detect luminosities as low as $\sim 10^{33}$ erg s^{-1} at the $\gtrsim 3\sigma$ level (which is the expected luminosity of a quiescent BeXRB, low-mass X-ray binaries and supersoft sources).

In order to find the expected flux of SNR and other diffuse emission, available Chandra observations of SNR in the LMC can be used (Williams and Chu, 2005). The average flux of these objects in the LMC are 0.15 counts s^{-1} arcmin^{-2} in the 0.3 keV to 8 keV range. Taking a temperature of

1.4 keV into account, this becomes 0.07 - 0.17 counts s^{-1} $arcmin^{-2}$ for the EPIC MOS - PN cameras in the 0.5 keV to 10 keV range, respectively. Since all observations will occur outside of the plane of the MW, the background contribution to diffuse emission are expected to be as low as 0.004 counts s^{-1} $arcmin^{-2}$ in the 0.5 - 10 keV range for both cameras.

Available X-ray surveys of the Magellanic Clouds in softer bands show that there is a significant number of background AGN that can contaminate the fields. Low count sources may still be identified with Bayesian hardness ratios.

1.6 Sources of X-ray Emission

The three fields observed by the XMM-Newton may contain a wide variety of celestial bodies, which include foreground stars (located in the Milky Way), background galaxies and stars located within the Magellanic Bridge. These objects are distinguishable from each other by radiation output in various energy bands.

1.6.1 K Stars and M Dwarfs

The X-ray emission from late-type stars (such as K and M stars) is believed to be the result of a hot coronal plasma, with temperatures of $\log(T) \sim 6-7$ K (Gudel, 1992). Factors such as the presence of a strong magnetic field or rapidly rotating star may produce the X-ray emission that has been observed, which ranges in luminosity as $\log(L_X) \sim 27 - 29.6$ erg s^{-1}. It has been theorised that the strong magnetic field traps matter in giant coronal loops (similar to the Sun, but much larger). This leads to gyrosynchrotron emission, meaning electrons are accelerated to relativistic speeds by the magnetic field.

A proportional correlation between the X-ray luminosity and radio luminosity has also been observed in late-spectral type stars, that exists over

three orders of magnitude (Güdel et al., 1993).

1.6.2 Active Galactic Nuclei

Active Galactic Nuclei (AGN) are a class of galaxies whose central supermassive black hole is actively accreting material. The black hole radiates up to 10^4 times the energy of a non-active galaxy, and is emitted from a region smaller than $1\,\mathrm{pc}^3$ (Massi, 2013). The radiation can be seen at various wavelengths, and thus are detectable by X-ray telescopes.

Although there are several categories of AGN (classified according to spectra), it is believed that they all share the same structure, and the observed spectra is dependent on the viewing angle (Urry, 2004).

Relativistic jets may also be observed being emitted from certain AGNs. The jets are perpendicular to the accretion disk, and can span from several astronomical units to megaparsecs (Blandford et al., 2019). Strong magnetic fields from the accretion disk cause the jet to be collimated near the black hole. These jets can be observed in the radio due to synchrotron radiation.

1.6.3 Supernova Remnants

When the gravitational force of a massive star ($> 8\ \mathrm{M}_\odot$) exceeds the radiative pressure, a core-collapse occurs resulting in a supernova. Material surrounding the core rapidly expands at a fraction of the speed of light. The friction between this material and the interstellar medium becomes plasma and radiation is emitted in several energy bands (Vink, 2012). The plasma shell can be seen as an extended object through an X-ray telescope (spanning over several pixels), as opposed to a point source.

Due to the immense gravitational force that precedes the supernova, either a neutron star or black hole is created. A binary star system (containing large hydrogen-rich stars) may have one star go supernova, resulting in binary where the companion becomes either a neutron star or a black hole. These

systems are known as High Mass X-ray Binaries (HMXBs). The existence of a supernova remnant (specifically core-collapse supernova) may reveal either a neutron star or black hole at the centre of the shell, making it easier to locate potential HMXBs.

The supernova remnant (SNR) is an important celestial object for studying stellar and galactic evolution. One example of their importance are the higher than expected numbers of SNRs located in the region between the Milky Way and the Magellanic Clouds (Stanimirovic et al., 1999), this increase is evidence for tidal interactions between the galaxies, giving rise to a starburst period.

1.6.4 Be/X-ray Binaries

High Mass X-ray Binaries (HMXBs) are binary systems containing a donor star (O- and B-spectral types) that is orbited by a compact object (such as a neutron star or a black hole). X-ray outbursts are caused by accretion of material from the donor star onto the compact object, not by Roche-lobe filling, but rather from stellar winds from the donor star.

A particular subclass of HMXBs are known as Be/X-ray Binaries (BeXRBS). These systems contain a Be star (B star with Hα emission), with a neutron star companion. The donor star is rapidly rotating, which allows for material to accumulate into a circumstellar disk, this disk is responsible for the Hα emission. In some systems, the compact object is on a highly eccentric orbit around the donor star, such that during periastron passage, the compact object is able to accrete material triggering an X-ray outburst. These outbursts are periodic, and the orbital period of the compact object may be derived from this information, and are categorised as type I outbursts, with energies between 10^{36-37} erg s^{-1}.

Stronger outbursts may also be triggered when the donor star emits solar winds, or caused by an evolution of the structure within the circumstellar disk, such as a phase of massive disc loss (Okazaki et al., 2013). These

outbursts may exceed 10^{37} erg s^{-1} in emission, and are classified as type II outbursts.

The progenitors of these systems are OB binary stars, and are believed to evolve through mass transfer, proposed by Rappaport and van den Heuvel (1982) in a model called rejuvenation. Mass transfer occurs from the primary to the secondary B star. The transfer increases the rotation speed of both stars, resulting in the primary star forming a circumstellar disc. This suggests that the primary star is not born as a fast rotator, nor is it a result of increased rotation speed during the evolution off the main-sequence (Coe, 2000).

The secondary star then undergoes a supernova event, which has several outcomes depending on the mass of the star. If the primary star is less than $\sim$ 8 $M_\odot$, it is ejected from orbit by a supernova kick. Otherwise, if the primary star is greater than $\sim$ 22 $M_\odot$, it becomes a supergiant, resulting in a supergiant HMXB (van den Heuvel, 1983; Verbunt and van den Heuvel, 1995). Evidence to support this can be found when comparing the spectral distribution of isolated Be stars to Be stars in BeXRBs within the Milky Way. The spectral distribution in BeXRBs are found to be narrower, ranging from 09V ($\sim$ 22 $M_\odot$) to B2V ($\sim$ 8 $M_\odot$) (McBride et al., 2008).

The MW is greater in mass than the SMC by a factor of 50, thus it is expected that the MW would harbour more HMXB systems (by a similar factor). However, there are roughly 50 known HMXBs located in the MW, along with 35 known in the SMC, majority of which are BeXRBs (Coe et al., 2005, 2009). This substantial difference is evidence of tidal interaction between the MW and Magellanic Clouds (McBride et al., 2008).

In the Bridge, there are three known HMXBs, the first was discovered in the SMC wing (Kahabka and Hilker, 2005). Two other systems were later discovered by McBride et al. (2010), along with three candidate HMXBs. The nature of these BeXRBs will be discussed in detail, in section 4.2.2.

HMXBs as Tracers of Star Formation

When quantifying stellar formation history in a galaxy, High Mass X-ray Binaries (HMXBs) are used as tracers (Grimm et al., 2003a). Grimm et al. (2003a) used a large sample size of galaxies, these include nearby sources that are resolvable by Chandra, as well as distant galaxies found within the Hubble Deep-Field, where the majority of the X-ray luminosity is a result of HMXBs. Any galaxies exhibiting AGN-like properties were discarded, since the purpose was to search for a relationship between HMXBs and the star formation rate (SFR).

It was found that there exists a relationship between the X-ray luminosity (dominated by HMXBs) of a galaxy with the SFR. The presence of HMXBs may be used to infer a star formation rate, since they are rapidly evolving, short-lived systems. It is expected to find these systems in the Magellanic Bridge if it is a star forming region. The only three confirmed systems are still located near the SMC, however a population of HMXBs further east (closer to the LMC) are expected to exist.

SFR and HMXB Relation in the MB

The effects of gravitational interaction on intergalactic regions is difficult to perform in distant systems. The resolvability of the Bridge allows for the probing of star formation rates.

There exists a correlation between the number of HMXBs that are in a galaxy, and the galaxy's star formation rate (SFR) (Grimm et al., 2003b). This was found by studying nearby galaxies, where a significant portion of the X-ray luminosity is the result of HMXBs.

This relation is also found in galaxies with low SFR, where it is below 4.5 $M_\odot$ yr^{-1}; it has been found to be non-linear ($L_X \propto SFR^{\sim 1.7}$). However, it is difficult to make a direct comparison to the star formation within the Magellanic Bridge, due to the lower gas and stellar density (since it is an intergalactic region). The HMXBs observed in Grimm et al. (2003b) were

also X-ray active, with luminosities greater 10^{38} erg s^{-1}, and is difficult to use in comparison with the Magellanic Bridge if not all HMXBs are X-ray active.

An approximation of BeXRBs per square degree in the Magellanic Bridge was performed by Kahabka and Hilker (2005). This was done by using the initial mass function for B stars in the Bridge, then applying a Be/B ratio to obtain a total number of Be stars. To arrive at a BeXRB area density, an assumption was made for the amount of Be stars that have a neutron star companion. A value of 0.68 - 0.98 BeXRBs per square degree was obtained, and varied depending on the initial mass function of B stars. Further investigation by McBride et al. (2010) suggests that the BeXRB area density may be larger than one BeXRB per square degree.

This dissertation is structured as follows: chapter 2 will present the X-ray data obtained from XMM-Newton in three separate fields in the Magellanic Bridge that coincide with photometric data obtained by Harris (2007), with information on the X-ray sources extracted. Chapter 3 will present optical spectroscopic observations of objects in Harris (2007) that coincide within $3''$ or less of X-ray sources found in chapter 2. Chapter 4 will discuss the results of chapters 2 and 3. Chapter 5 will conclude the dissertation and discuss possible future work.

Chapter 2

X-Ray Data Reduction and Analysis

2.1 Available X-ray Data

In accordance with available photometric data obtained by Harris (2007), three regions of the Magellanic Bridge were observed with the XMM-Newton (section 1.4), each for more than 30 ks. The three regions observed are located near the Small Magellanic Cloud, two follow the H_I ridgeline, while the other is offset North from the ridgeline.

The available data can be found on the XMM Science Archives (European Space Agency, g), with their observation IDs listed within Table 2.1, along with other details such as observation time and pointing location.

2.2 X-ray Reduction

2.2.1 Initialising Software

The software used for the reduction of XMM-Newton data are HEASoft (National Aeronautics and Space Administration, a, version 6.24) and System

Table 2.1: Observed regions with associated target names, pointing locations, photometric counterparts (Harris, 2007), observation time and observation IDs of XMM-Newton data. X-ray region ID assigned by XMM-Newton, with abbreviated ID in square brackets. Fields displayed in figure 2.1.

XMM-Obs. ID [Abbr. ID]	R.A. [J2000]	Dec. [J2000]	Harris ID	Obs. Time (s)
0674110101 [MB1]	01h 48m 00.00s	-74^o 30$'$ 00.0$''$	mb02	34919
0674110201 [MB2]	02h 00m 00.00s	-73^o 00$'$ 00.0$''$	mb03	36714
0674110401 [MB3]	02h 23m 59.99s	-73^o 54$'$ 02.0$''$	mb06	31915

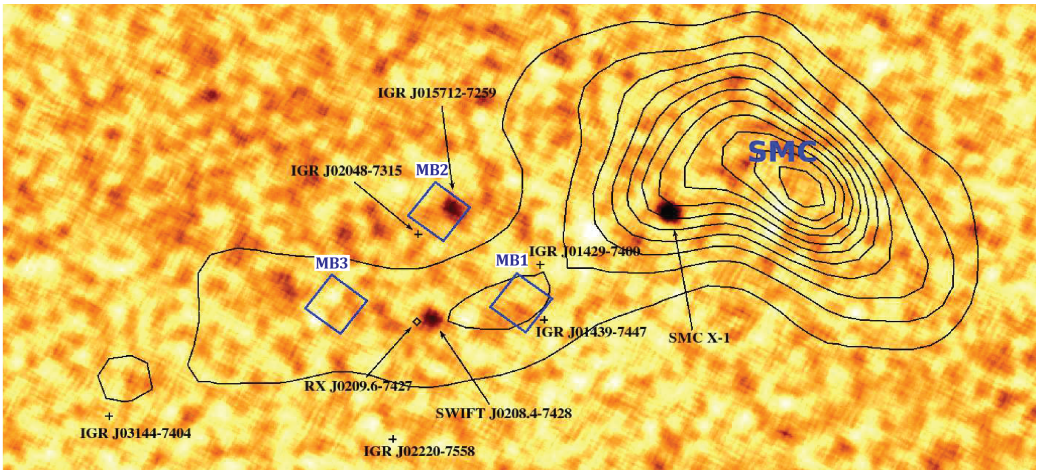

Figure 2.1: 15 - 35 keV *INTEGRAL* image of the SMC including the western region of the Magellanic Bridge, contours show the H I density map (Putman et al., 2003). The three fields observed with the XMM-Newton are shown using their abbreviated IDs, and can be found in Table 2.1. Known HMXBs in the Bridge include IGR J015712−7259, Swift J0208.4−7428 and RX J0209.6−7427. Candidate HMXBs are displayed with a cross. Figure has an approximate size of $5^o \times 10^o$.

Analysis Software (European Space Agency, b, SAS version 17.0.0), all performed on Ubuntu 16.04. XMM data are downloaded as original data files (ODFs), which are stored within a directory labelled `ODF`.

Before reduction of the ODFs can begin, HEASOFT and SAS must be initialized in a terminal. All reduction is then performed within said terminal. The relevant information required for this particular project are X-ray source locations, which can be followed up with optical observations, and hardness-ratios (more information in section 2.4), which allow for the initial classification of sources.

Since the procedure for reducing the ODFs requires multiple lines of commands, a more practical approach is to create a bash script that contains multiple commands and can be performed on any dataset. There are three separate datasets that must be reduced, these are shown in Table 2.1.

2.2.2 Reducing Data Using Script

This section will detail the steps required to reduce data obtained from XMM-Newton. The following steps are performed in a bash script and follow the SAS data analysis thread (European Space Agency, e).

To begin, HEASoft and SAS are both initialized via the script, which are detailed in the SAS start-up guide (European Space Agency, d). The location of the ODFs are then exported by using the following command:

```
export SAS_ODF = /path/to/ODF
```

This allows the software to locate the files to reduce. A work directory is then created, within the same parent directory to the ODF folder. This folder stores the output files created during the reduction process.

Calibration files are created according to the given dataset, and is covered in the SAS start-up guide. The calibration file (named ccf.cif) is created by using the command `cifbuild`, this cif file is then exported as:

```
SAS_CCF = /path/to/ccf.cif
```

This calibration file is unique for each dataset. Followed by this, a .SAS file is created (the filename can be any combination of letters or numbers, depending on the dataset) by using the command `odfingest`. Regardless of the filename, it is exported as:

```
SAS_ODF = /path/to/*.SAS
```

where * is the placeholder for the filename.

Once the calibration files have been created, event lists may be produced. These are used for creating images and extracting source information. For the production of event lists, a meta-task is run depending on the camera used. Event lists are created for all three EPIC cameras (MOS1, MOS2 and PN).

To create event lists for the MOS1 and MOS2 cameras, the command `emproc` is used, and for the PN camera, the command `epproc` is used. These commands are classified as meta-tasks, since they run several smaller tasks that are not explicitly stated within the SAS data analysis thread. Once the event lists have been created, they need to be cleaned of high energy background flaring that may have occurred during observation. The SAS filter guideline is followed (European Space Agency, c). A single event, high energy counts/second (rate) versus time graph is produced by using the `evselect` command. The energy parameter (named PI) for MOS is set to accept any counts that are greater than 10 keV, and the parameter for PN is in the range of 10-12 keV (this is to not confuse actual signal for a high energy background event). To make it a single event only, the parameter `PATTERN` is set to 0. An example of a high energy, single event light curve can be found in figure 2.2. Each light curve is examined by the user in order to determine the baseline count rate. According to the SAS filter guideline, it is recommended that the baseline for the MOS cameras is just below 0.35 counts/second, and the

baseline for the PN camera is just below 0.4 counts/second. This may vary for each data set.

Once a baseline count rate for each camera has been determined, the script then requires the value to be entered into the terminal. A new file, called `gtiset`, is created, followed by the command `tabgtigen` to clean the event lists of high energy flares. These are the event lists that are used to produce images.

2.3 Producing Images From Cleaned Event Lists

The five XMM-Newton standard energy bands are:

- 0.2 - 0.5 keV (band 1)
- 0.5 - 1.0 keV (band 2)
- 1.0 - 2.0 keV (band 3)
- 2.0 - 4.5 keV (band 4)
- 4.5 - 12 keV (band 5)

where the lower energy ranges are categorised as the softer bands, and the higher energy ranges are categorised as the harder bands. Images are created for each band (for each camera), as well as an image that contains all bands (all counts between 0.2 - 12 keV). For the PN camera, band 1 was set to 0.3 - 0.5 keV, since there appeared to be an issue with hot pixels when creating an image. The full range for the PN camera was then set to 0.3 - 12 keV.

Images are produced by using the `evselect` command, with the `PI` parameter (energy range) set to each band, as well as set to over all bands. For the MOS and PN cameras, the `PATTERN` parameter was set to accept only

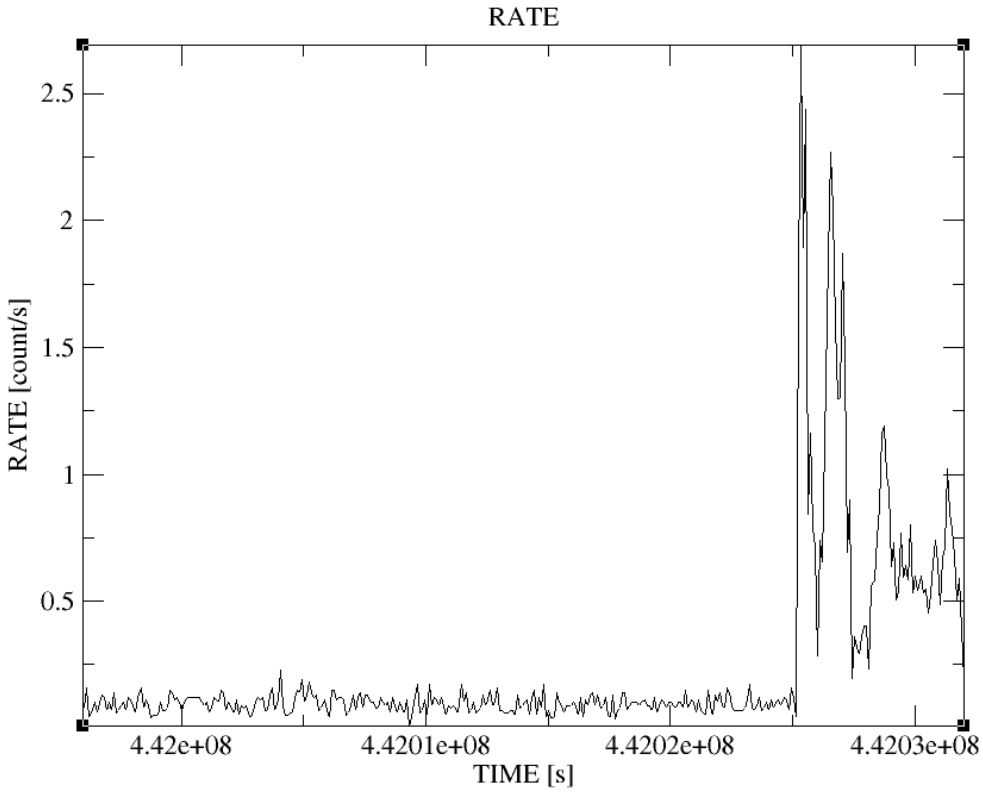

Figure 2.2: Light curve from single event only obtained from dataset MB2 in the MOS1 camera. The average count rate is below 0.25 counts per second. A high energy background event occurs around 4.42025×10^8 s, therefore the event list is cleaned by excluding any data obtained during this high energy flare.

single or double events. An example of an image produced from a cleaned event list can be found in figure 2.3.

2.4 Extracting Source Information

Once images have been created for all datasets and cameras, `edetect_chain` is then performed for each camera in each dataset. This command uses a source detection algorithm that stores the location of potential sources. Each image created for each band is accepted as an input, thus in total it requires five images for each camera. Another required input is the energy ranges (in eV), these are the bands defined at the start of section 2.3.

From this command, three files are created for each camera, the most important one contains the name `emllist`, since it contains each source's ID, R.A., Dec., counts/second, Hardness Ratios (HRs), associated errors, etc. This file may then be read into Python, where plots of source characteristics may be made.

HRs are a comparison of counts in each energy band. Following the same classification method as Sturm et al. (2013), the hardness-ratio of a source is calculated as follows:

$$\mathrm{HR}_i = \frac{\mathrm{R}_{i+1} - \mathrm{R}_i}{\mathrm{R}_{i+1} + \mathrm{R}_i} \tag{2.1}$$

where i ranges from 1 to 4, HR is the hardness-ratio, and R_i is the count rate in energy band i (defined in section 2.3). The HR value has a maximum value of 1 (corresponding to higher energy photons), and minimum value of -1 (corresponding to lower energy photons). Since the `emllist` contains the count rate for each energy band (and the associated error), it is automatically calculated and stored within the `emllist` (along with the propagated error).

The `emllist` may be read into ds9, and can be plotted over its associated image and producing a source list by using the command `srcdisplay`. The output file is named `regionfile`, which contains the location of each source in a text file. This file, however, does not contain the source numbers, and

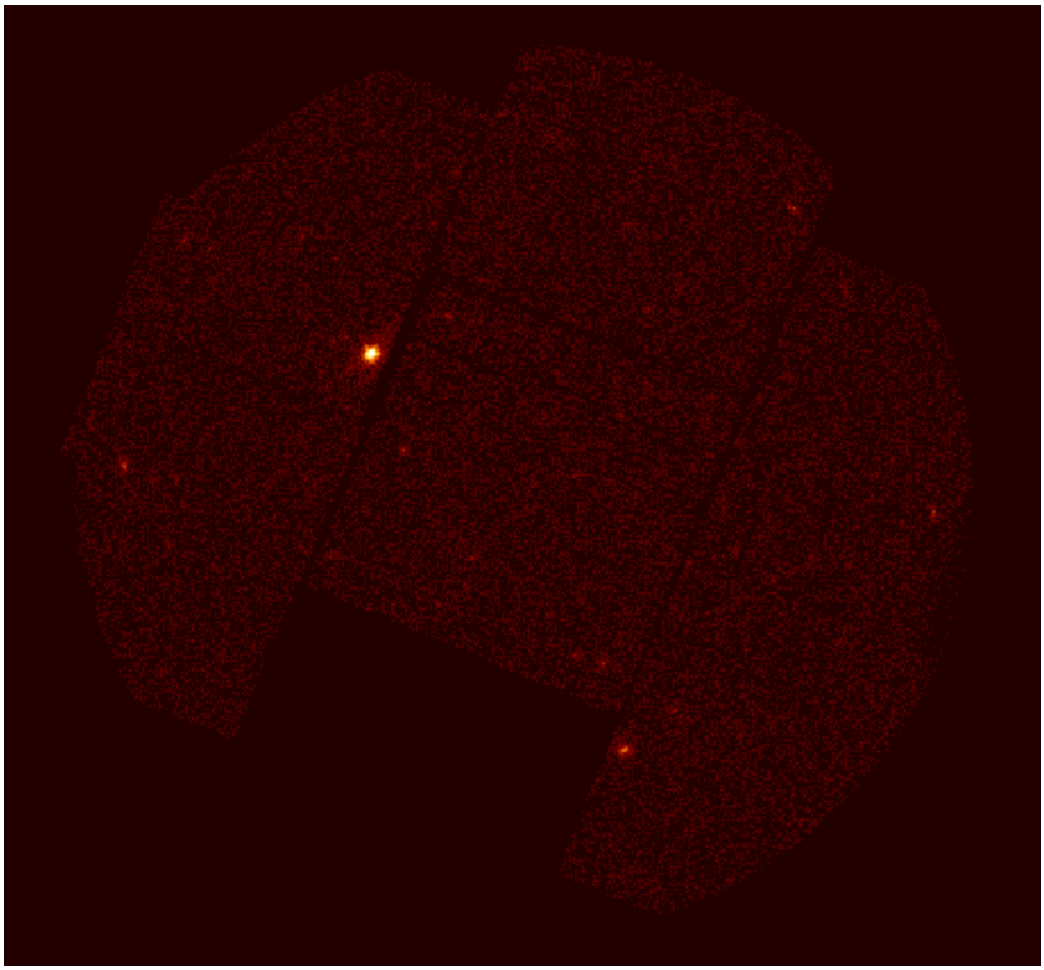

Figure 2.3: Image obtained from the cleaned event list of from the field MB2, obtained with the MOS1 camera.

an image similar to figure 2.4 is produced.

2.4.1 Information In `emllist`

The `emllist` contains seven rows of information for each source. The first and second row contain the total counts of the source (in all bands), with only the second row containing the four hardness-ratios (and associated errors, which have been propagated from the error in source counts). The following five rows contain the counts for each band, as well as the flux, but no information regarding the hardness-ratios. Since we are interested in the hardness-ratios, only the second row for each source (which is discussed in appendix A) will be extracted.

The extracted row also contains other important information, this includes its ID and source location (with error), which will be used for optical follow-up of interesting sources.

2.5 Hardness Ratios

As mentioned in section 2.4, HRs are a ratio of photon counts in two adjacent energy bands, and is calculated using equation 2.1. These ratios allow for a preliminary screening of interesting objects for possible follow-up.

A table of the four different types of HR classifications can be found in 2.2, which is a simplified version of the classification used in the XMM-Newton Survey of the SMC (Sturm et al., 2013). In this dissertation, objects are plotted in three different HR planes. Based on the results, figure 2.5 contains regions where different types of astronomical sources exist. For example, AGN and radio background sources (defined in Payne et al., 2004) are found to lie within the hard classification (HR_2 - HR_3), whereas non-active Galaxies lie within the soft classification.

Although useful, HRs do not determine the nature of a source, and there are cases where a HMXB may exist in the soft classification. Additional in-

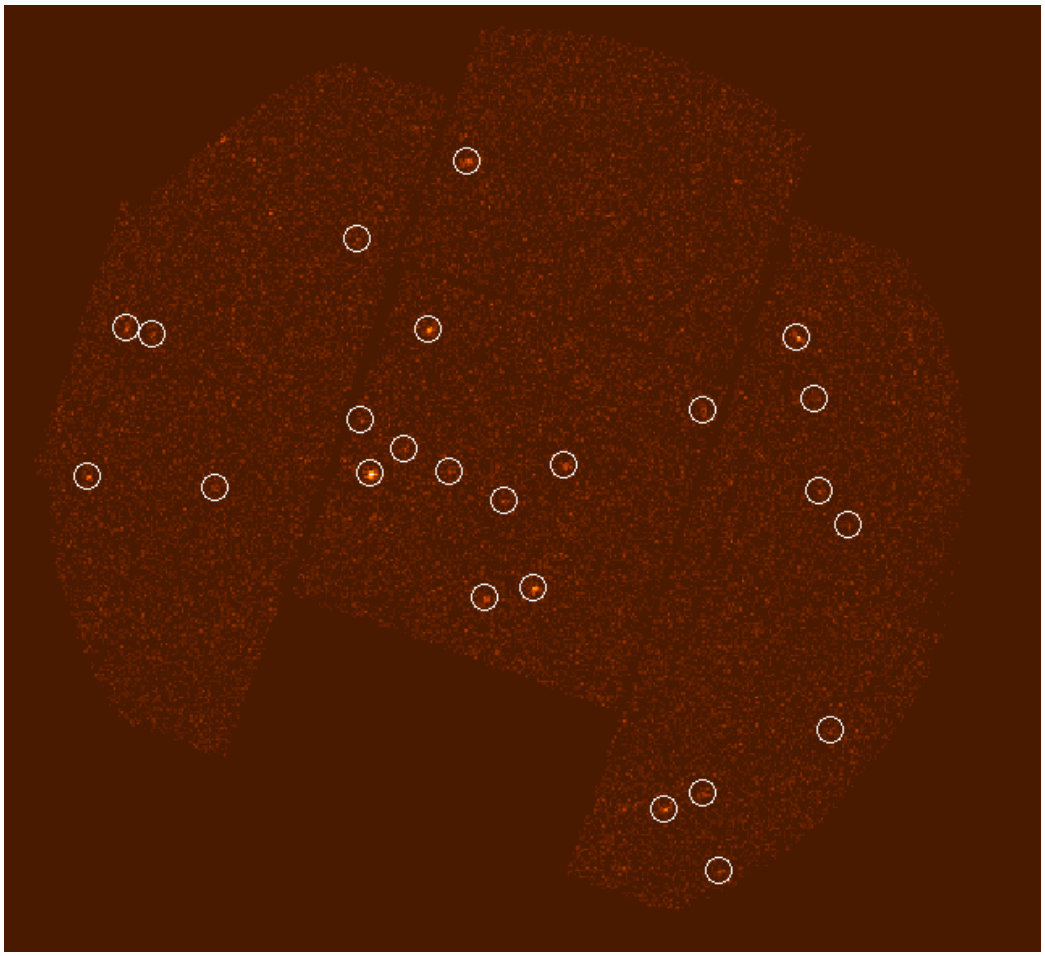

Figure 2.4: An image obtained from MOS1 in field MB1 which contains all detected source locations.

Table 2.2: Source classification based on the HR of various sources as defined in Sturm et al. (2013).

Spectrum	Selection criteria
Super Soft (ss)	$8HR_1 + 3HR_2 < -3$ or ($HR_1 < -0.75$ & HR_2 not def.)
Soft (s)	$8HR_2 + 3HR_3 < -3$ or ($HR_2 < -0.75$ & HR_3 not def.)
Hard (h)	($8HR_2 + 3HR_3 > -3$ or ($HR_2 > 0$ & HR_3 not def.)) & not ss
Ultra Hard (uh)	($8HR_3 + 3HR_4 > -1.4$ or ($HR_3 < 0.2$ & HR_2 not def.)) & not ss & not s
Unclassified	Not contained in any of the above expressions

formation, such as optical data, are required to classify these objects. As will be explained in section 3.4, there is a magnitude limit on the spectrograph which was used for optical follow-up. Thus HR selection of ultrahard sources (candidate HMXBs) was not feasible since many of the optical matches were below the magnitude limit. Regardless, those interested in analysing candidate systems may use HRs to select for interesting objects.

2.6 X-ray Data Analysis

The regions observed, along with exposure times, can be found in Table 2.1. Each dataset was observed with the MOS1, MOS2 and PN cameras. An `emllist` file was produced for each camera in each dataset, which amounts to a total of nine files, three for each region.

The following sections will investigate the amount of sources detected in each region. Images from each camera will also be displayed, along with the detected sources. The hardness-ratio plots will also be displayed for each camera. The plots will contain all sources that have an error below 0.7, this is to make the graph easily readable. All sources will still be categorised if an appropriate optical counterpart is observed.

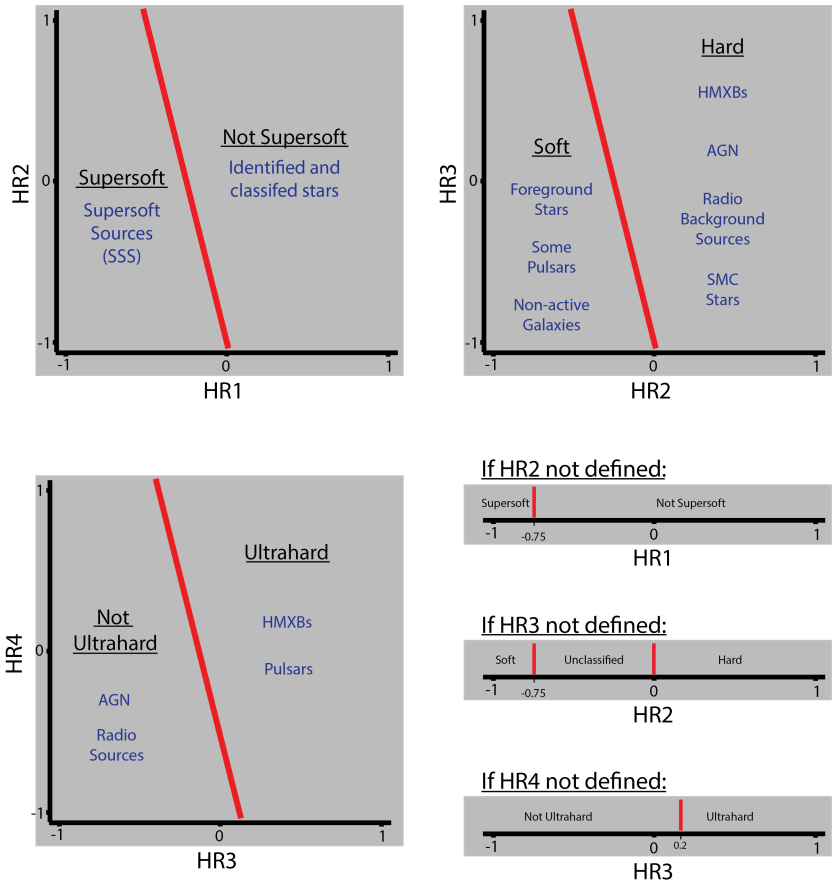

Figure 2.5: Hardness Ratio (HR) classifications based on Table 2.2, with objects found to cluster based on these hardness ratios (based on clusterings found in figure 8 of Sturm et al., 2013). The bottom right graphs show classifications if HR2, HR3 or HR4 are undefined.

2.6.1 Dataset MB1

The images produced from the MOS1, MOS2 and PN camera, along with the hardness-ratio plots of detected sources from field MB1 can be found in figures 2.6, 2.7, and 2.8, respectively. A table of categorised sources can be found in Table 2.3.

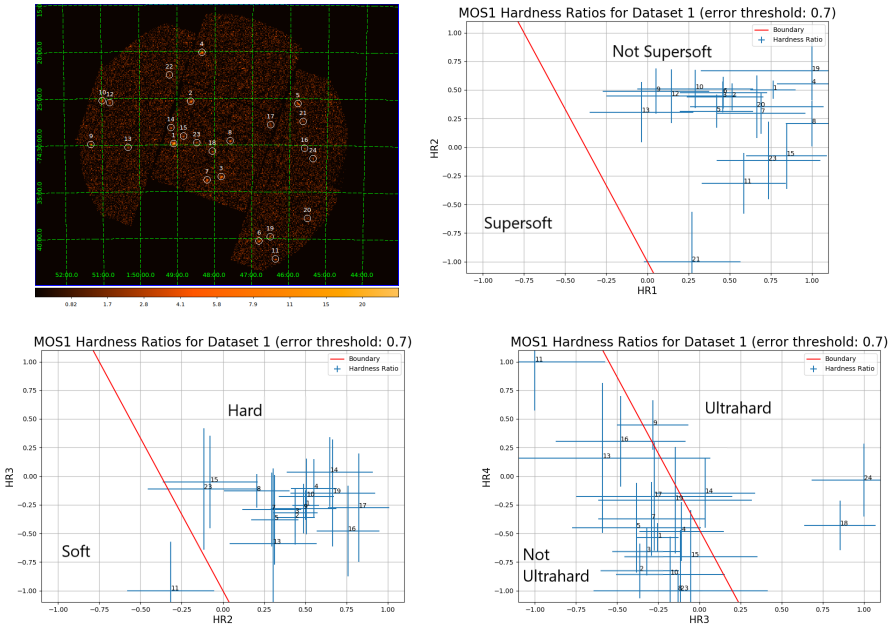

Figure 2.6: MOS1 sources in field MB1 with their hardness-ratios (HR). *Top left:* 24 sources detected. *Top right:* HR plot comparing HR_1 and HR_2; sources left of the boundary fall within the super soft category, sources right of the boundary are not super soft. *Bottom left:* HR plot comparing HR_2 and HR_3; sources left of the boundary fall within the soft category, sources right of the boundary are hard. *Bottom right:* HR plot comparing HR_3 and HR_4; sources left of the boundary are not ultra hard, and sources right of the boundary are ultra hard. All detected sources can be found in Table C.1.

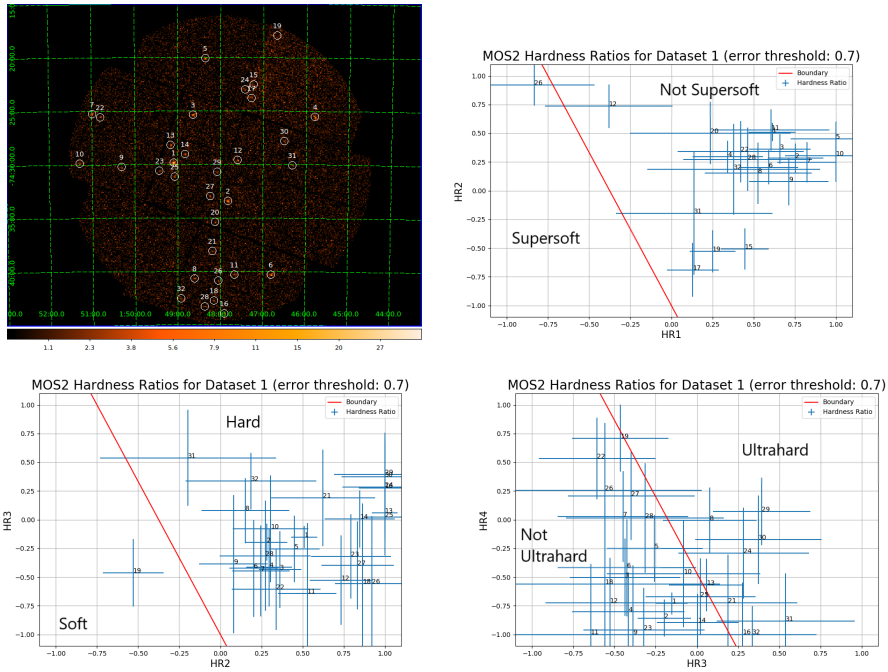

Figure 2.7: MOS2 sources in field MB1 with their hardness-ratios (HR), dataset contains 32 detected sources. Same as figure 2.6.

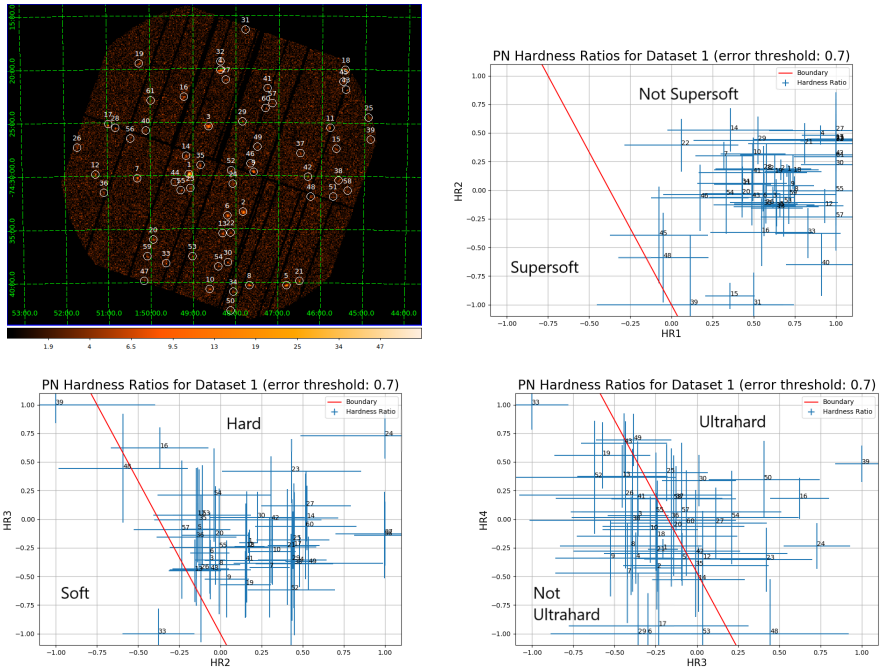

Figure 2.8: PN sources in field MB1 with their hardness-ratios (HR), dataset contains 60 detected sources. Same as figure 2.6.

Table 2.3: Detected sources in field MB1 categorised based on their hardness-ratios. Note that the same source may be contained within more than one category as well as detected by separate cameras due to the error in HR. Although not all sources are displayed in the HR diagrams in figs. 2.6 to 2.8 due to the error cut-off, or an HR value being undefined, the total amount of sources categorised are not affected by the error cut-off.

Dataset MB1					
Camera	Supersoft sources	Soft sources	Hard sources	Ultrahard sources	Total sources
MOS1	4	5	23	16	24
MOS2	3	2	18	10	32
PN	2	14	38	30	60

2.6.2 Dataset MB2

The images produced from the MOS1, MOS2 and PN camera, along with the hardness-ratio plots of detected sources from field MB2 can be found in figures 2.9, 2.10, and 2.11, respectively. A table of categorised sources can be found in Table 2.4.

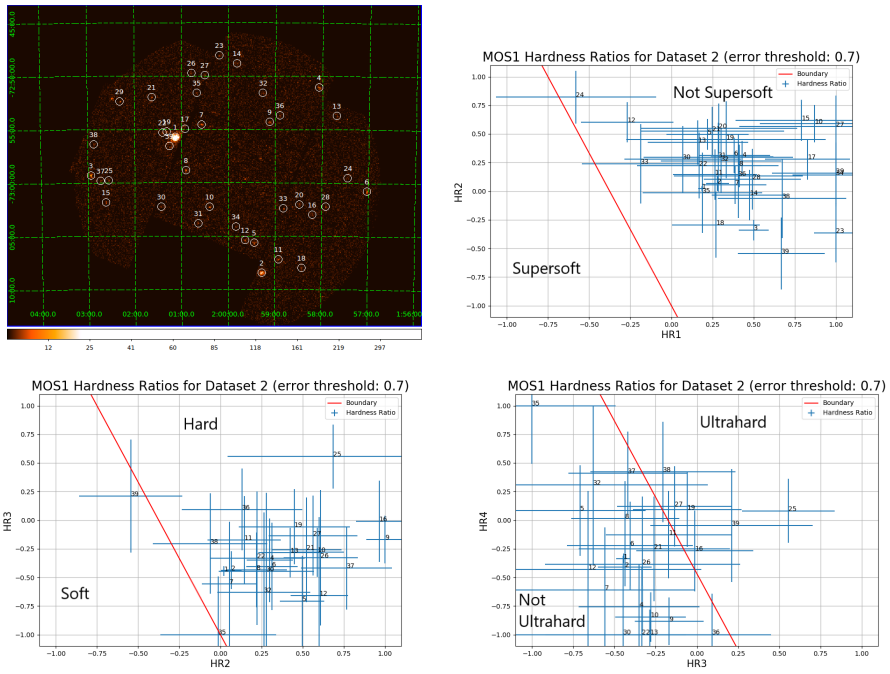

Figure 2.9: MOS1 sources in field MB2 with their hardness-ratios (HR). *Top left:* 39 sources detected. *Top right:* HR plot comparing HR_1 and HR_2; sources left of the boundary fall within the super soft category, sources right of the boundary are not super soft. *Bottom left:* HR plot comparing HR_2 and HR_3; sources left of the boundary fall within the soft category, sources right of the boundary are hard. *Bottom right:* HR plot comparing HR_3 and HR_4; sources left of the boundary are not ultra hard, and sources right of the boundary are ultra hard.

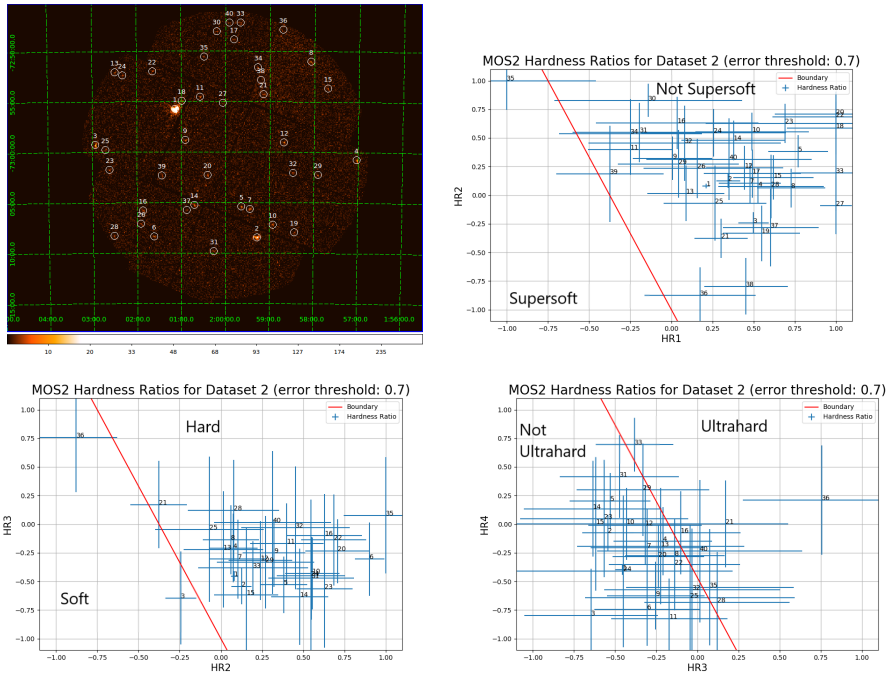

Figure 2.10: MOS2 sources in field MB2 with their hardness-ratios (HR), dataset contains 40 detected sources. Same as figure 2.9.

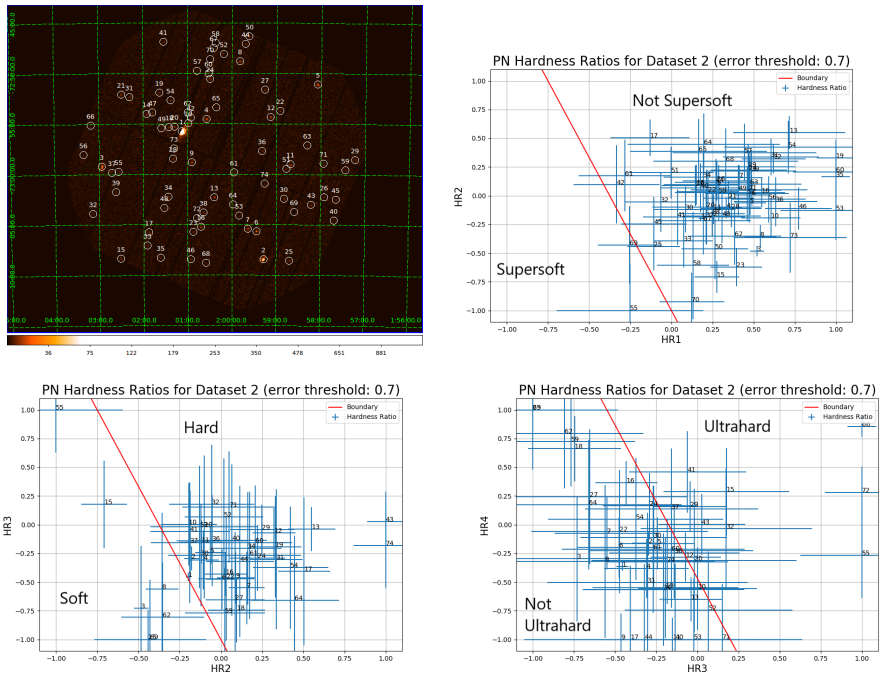

Figure 2.11: PN sources in field MB2 with their hardness-ratios (HR), dataset contains 73 detected sources. Same as figure 2.9.

Table 2.4: Detected sources in field MB2 categorised based on their hardness-ratios. Note that the same source may be contained within more than one category as well as detected by separate cameras due to the error in HR. Although not all sources are displayed in the HR diagrams in figs. 2.9 to 2.11 due to the error cut-off, or an HR value being undefined, the total amount of sources categorised are not affected by the error cut-off.

Dataset MB2					
Camera	Supersoft sources	Soft sources	Hard sources	Ultrahard sources	Total sources
MOS1	1	4	21	10	39
MOS2	5	6	29	22	40
PN	5	19	40	30	73

2.6.3 Dataset MB3

The images produced from the MOS1, MOS2 and PN camera, along with the hardness-ratio plots of detected sources from field MB3 can be found in figures 2.12, 2.13, and 2.14, respectively. A table of categorised sources can be found in Table 2.5.

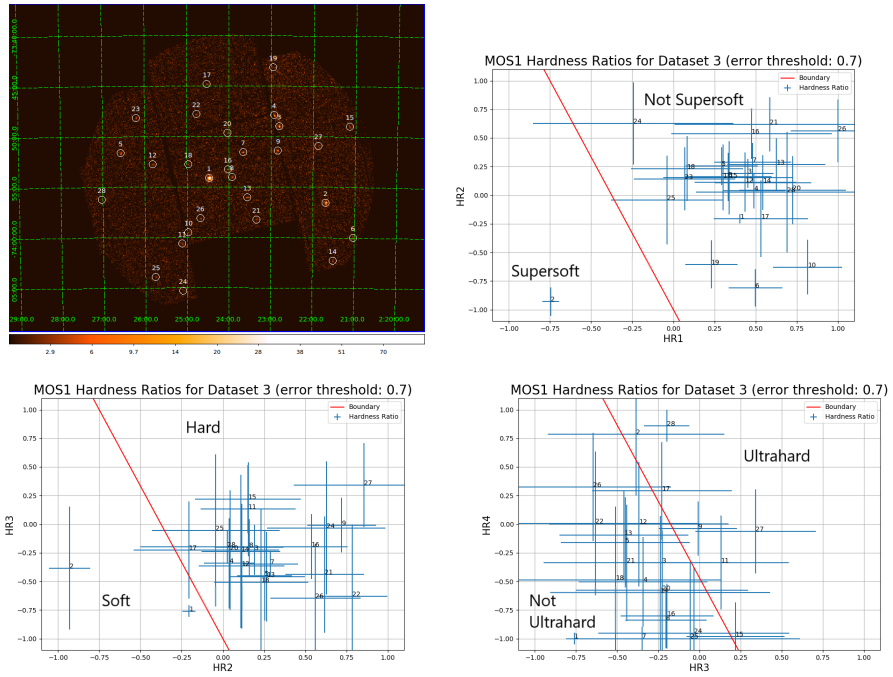

Figure 2.12: MOS1 sources in field MB3 with their hardness-ratios (HR). *Top left:* 28 sources detected. *Top right:* HR plot comparing HR_1 and HR_2; sources left of the boundary fall within the super soft category, sources right of the boundary are not super soft. *Bottom left:* HR plot comparing HR_2 and HR_3; sources left of the boundary fall within the soft category, sources right of the boundary are hard. *Bottom right:* HR plot comparing HR_3 and HR_4; sources left of the boundary are not ultra hard, and sources right of the boundary are ultra hard.

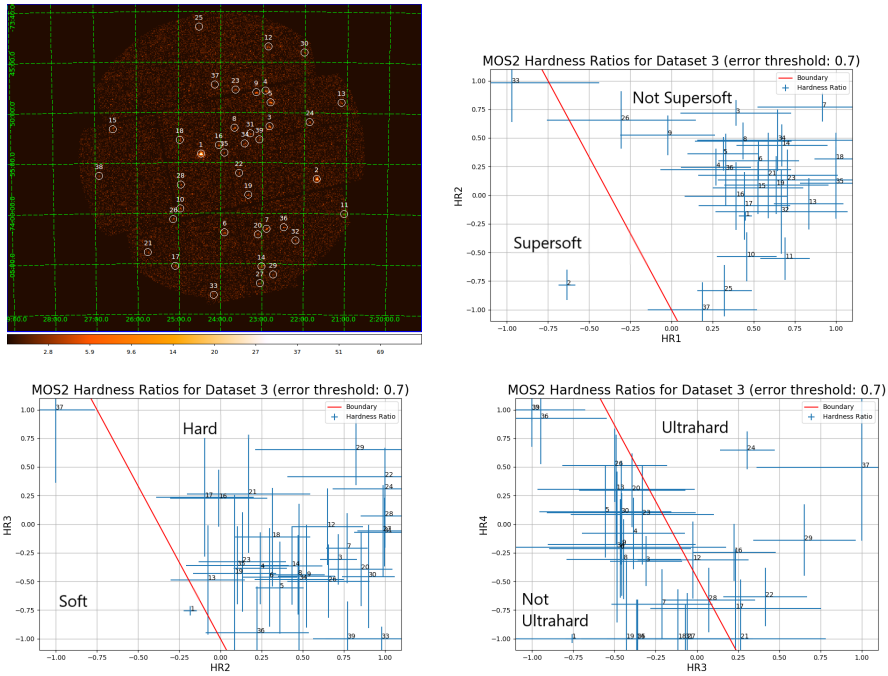

Figure 2.13: MOS2 sources in field MB3 with their hardness-ratios (HR), dataset contains 39 detected sources. Same as figure 2.12.

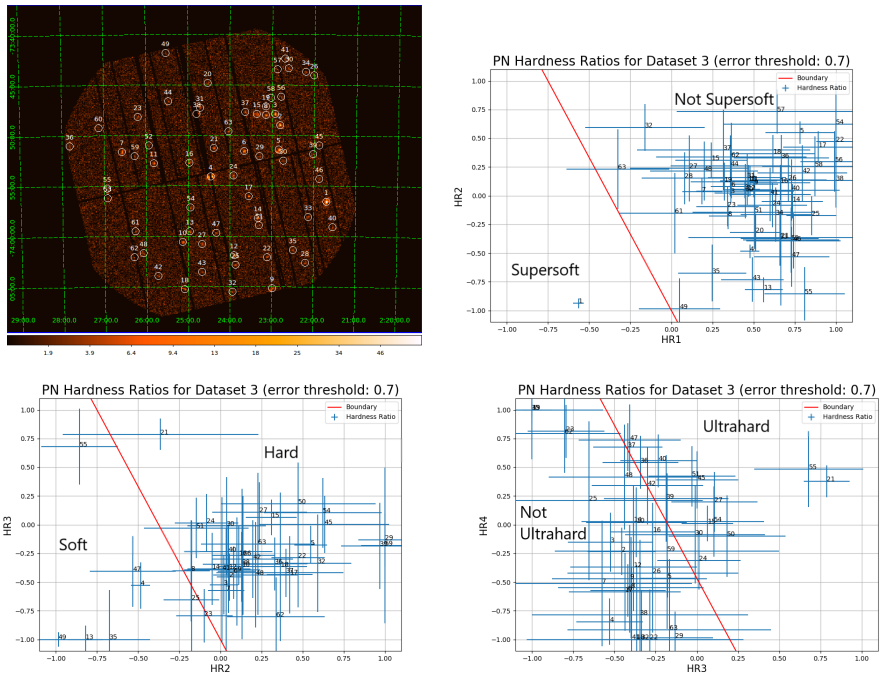

Figure 2.14: PN sources in field MB3 with their hardness-ratios (HR), dataset contains 39 detected sources. Same as figure 2.12.

Table 2.5: Detected sources in field MB3 categorised based on their hardness-ratios. Note that the same source may be contained within more than one category as well as detected by separate cameras due to the error in HR. Although not all sources are displayed in the HR diagrams in figs. 2.12 to 2.14 due to the error cut-off, or an HR value being undefined, the total amount of sources categorised are not affected by the error cut-off.

Dataset MB3					
Camera	Supersoft sources	Soft sources	Hard sources	Ultrahard sources	Total sources
MOS1	3	7	19	15	28
MOS2	3	7	21	13	39
PN	3	14	37	24	63

2.7 X-ray Point Source Catalogue of MB

The X-ray source lists comprises of detected sources in the three XMM EPIC cameras (in order of MOS1, MOS2 and pn) and in the three observed fields (in order of MB1, MB2 and MB3), resulting in nine tables. Due to the large amount of tables, only the sources from field MB1 detected by the MOS1 camera will be included in this section. All tables will be located in appendix C.

The source IDs are assigned according to the source finding algorithm used in XMM, and is not based on either flux or position in sky. Positional, flux and hardness ratios (HR) errors are according to a 1σ error.

The sources have not been boresight corrected (due to a combination of short time constraints and the low density of objects in the regions observed). Therefore, detections across all cameras are listed, instead of a single source list for each observed field. The only available catalogue is the 3XMM-DR6 Survey (Rosen et al., 2016), which coincides with field MB3. All X-ray sources are cross-matched in section 3.2 with photometric objects from Harris

(2007).

2.7.1 Example Table (Field MB1)

Table 2.6: X-ray point source list of all detections in the MOS1 camera in dataset MB1, corresponding image and HR plots are found in figure 2.6. All X-ray source list tables can be found in appendix C.

MOS1 Sources in Dataset MB1													
Source ID	R.A. [J2000]	Dec. [J2000]	σ(pos) [″]	Flux [erg cm^{-2} s^{-1}]	σ(Flux) [erg cm^{-2} s^{-1}]	HR_1	$\sigma(HR_1)$	HR_2	$\sigma(HR_2)$	HR_3	$\sigma(HR_3)$	HR_4	$\sigma(HR_4)$
1	01 49 05.3	-74 29 51	0.56	1.08×10^{-13}	1.67×10^{-14}	0.765	0.138	0.502	0.082	-0.253	0.127	-0.537	0.127
2	01 48 38.2	-74 25 22	0.95	3.70×10^{-14}	1.05×10^{-14}	0.515	0.192	0.439	0.12	-0.36	0.239	-0.828	0.239
3	01 47 49.2	-74 33 25	0.93	3.44×10^{-14}	8.46×10^{-15}	0.458	0.217	0.44	0.135	-0.32	0.209	-0.659	0.209
4	01 48 20.3	-74 20 07	1.2	9.23×10^{-14}	3.16×10^{-14}	1	0.211	0.553	0.14	-0.107	0.258	-0.483	0.258
5	01 45 47.1	-74 25 33	0.91	5.50×10^{-14}	2.29×10^{-14}	0.421	0.223	0.315	0.144	-0.382	0.393	-0.45	0.393
6	01 46 47.6	-74 40 17	1.28	3.48×10^{-14}	1.82×10^{-14}	0.463	0.266	0.476	0.139	-0.793	0.767	-0.222	0.767
7	01 48 12.0	-74 33 45	1.36	3.05×10^{-14}	1.10×10^{-14}	0.692	0.269	0.297	0.18	-0.29	0.323	-0.372	0.323
8	01 47 35.1	-74 29 36	1.26	1.33×10^{-14}	3.65×10^{-15}	1	0.158	0.206	0.199	-0.128	0.148	-1	0.148
9	01 51 17.6	-74 29 53	1.32	2.26×10^{-13}	7.20×10^{-14}	0.053	0.324	0.489	0.199	-0.283	0.217	0.447	0.217
10	01 50 58.7	-74 25 14	1.57	5.34×10^{-14}	2.47×10^{-14}	0.292	0.352	0.508	0.167	-0.176	0.331	-0.858	0.331
11	01 46 21.1	-74 42 12	1.82	6.04×10^{-14}	3.55×10^{-14}	0.586	0.256	-0.316	0.264	-1	0.428	1	0.428
12	01 50 46.8	-74 25 28	1.8	2.29×10^{-14}	2.01×10^{-14}	0.146	0.396	0.446	0.234	-0.328	0.755	-1	0.755
13	01 50 18.4	-74 30 15	2.4	3.30×10^{-14}	2.27×10^{-14}	-0.035	0.315	0.305	0.264	-0.589	0.656	0.16	0.656
14	01 49 09.7	-74 28 11	1.42	3.74×10^{-14}	1.44×10^{-14}	1	1.126	0.649	0.262	0.036	0.304	-0.148	0.304
15	01 48 49.8	-74 29 05	1.58	1.27×10^{-14}	6.47×10^{-15}	0.847	0.246	-0.077	0.288	-0.051	0.406	-0.702	0.406
16	01 45 35.9	-74 30 20	1.82	4.82×10^{-14}	2.50×10^{-14}	1	0.831	0.759	0.191	-0.478	0.395	0.305	0.395
17	01 46 30.4	-74 27 50	2.06	2.74×10^{-14}	1.66×10^{-14}	0.187	0.894	0.824	0.187	-0.274	0.474	-0.177	0.474
18	01 48 03.5	-74 30 42	1.66	2.64×10^{-14}	8.29×10^{-15}	1	3.952	0.106	0.986	0.855	0.217	-0.431	0.217
19	01 46 29.5	-74 39 48	2.11	4.81×10^{-14}	2.96×10^{-14}	1	0.675	0.667	0.257	-0.146	0.467	-0.21	0.467
20	01 45 29.7	-74 37 48	2.09	1.52×10^{-14}	1.40×10^{-14}	0.666	0.407	0.353	0.274	-0.415	0.867	-0.707	0.867
21	01 45 38.6	-74 27 28	2.43	1.78×10^{-14}	1.84×10^{-14}	0.273	0.295	-1	0.437	1	0.937	0.668	0.937
22	01 49 11.6	-74 22 32	1.94	1.63×10^{-14}	1.42×10^{-14}	1	2.511	0.892	0.251	-0.596	0.825	-0.446	0.825
23	01 48 28.7	-74 29 47	1.98	5.54×10^{-15}	3.84×10^{-15}	0.736	0.316	-0.116	0.339	-0.113	0.531	-1	0.531
24	01 45 22.2	-74 31 24	2.13	5.68×10^{-14}	2.55×10^{-14}	-	-	-	-	1	0.318	-0.033	0.318

Chapter 3

Optical Follow-up

3.1 Available Optical Data

The XMM-Newton fields were selected because of the optical coverage already available in those regions. The optical data comprises of a photometric survey of several fields along the H_I ridgeline that joins both Magellanic Clouds (hereinafter referred to as the Magellenic Bridge) as well as fields chosen outside of the H $_I$ ridgeline (Harris, 2007). The photometric data from Harris (2007) was obtained using the Washington C, Harris R and Cousins I bands (more information on these photometric systems can be found in Bessell, 2005).

There are various objects that emit X-rays that do not lie within the Bridge, these include background AGN and foreground stars. Objects of interest that lie within the Bridge are High Mass X-ray Binaries (HMXB), supernova remnants (SNRs) and soft X-ray transients. Three known HMXBs in the Bridge are RX J0209.6−7427 (Kahabka and Hilker, 2005), IGR J015712−7259 and Swift J0208.4−7428 (McBride et al., 2010).

3.2 Source Lists

The SAS software used to generate the source lists also produce a file known as the `emllist` contains the R.A. and Dec. of each detected source (additional information on this file is located in appendix A). These X-ray source locations (field names prefixed with 'MB') are then cross-matched with the photometric data (Harris, 2007, field names prefixed with 'mb') using Aladin Catalogue Software (University of Strasbourg) within a 3″ radius. Matched sources between the X-ray Magellanic Bridge fields and photometric Harris fields are shown in tables 3.1, 3.2, and 3.3.

The 3XMM-DR6 catalogue (Rosen et al., 2016) contains source detections from over 9000 fields, taken between the 3rd of February, 2000, to the 4th of June, 2015. All fields are publicly available on the XMM-Science Archives (European Space Agency, g), one of which uses the same original data files for field MB3. Therefore sources that match within a small radius are most likely the same object, which can be confirmed by comparing source hardness ratio and flux in all bands. In total, 52 3XMM-DR6 sources were cross-matched in field MB3.

When matching the X-ray sources with the optical sources, one X-ray source may be within 3″ of more than one optical source. An example of this can be found in Table 3.1, where the optical sources 24195 and 24225 both matched with MOS1 source 12 in field MB1. Although the separation distance for 24195 is smaller than 24225, no sources can be ruled out yet, further investigation must be performed to determine which optical source is the counterpart to the X-ray source. Since both optical sources are fainter than 20 magnitude, performing spectroscopy is difficult. The magnitude limit for follow-up observation is discussed further in section 3.4.

Due to weather and time constraints during the observation run, a magnitude cut of 18 was made to provide a sufficient signal-to-noise ratio for a 600 - 900 s exposure. A total of 7 sources from all 3 fields (table 2.1) were brighter than 18 magnitude (in any band). However, given the time constraint (only

2-3 hours per night in February) on the visibility of the Magellanic Bridge, only 6 sources were observed. Of the 6 sources observed using the low resolution grating, object 5437 was followed up using a higher resolution grating, grating 4. Note that the slit width for all observations was set to 2.24″. Sources with more than one exposure had their spectra combined.

3.3 Spectroscopic Calibrations

Spectroscopy of Harris (2007) objects that cross-matched with the X-ray point sources was performed using SpUpNIC (Spectrograph Upgrade - Newly Improved Cassegrain, South African Astronomical Observatory), which is mounted to the 1.9m telescope, located in Sutherland, South Africa. Before each observation run, a list of procedures must be completed in order to calibrate the spectrograph due to various environmental factors that affect the instrument.

At the start of calibration, multiple bias frames are taken. These are zero second exposures with no light on the charge-coupled device (CCD). This determines the readout noise and bias level, and is used to calibrate future images. These images are either called zero or bias images.

A Hartmann sequence is performed in order to focus the spectrograph. This is done by using two separate shutters that block a portion of the light after it has been passed through the collimator one at a time. An arc lamp is used to measure the change in focus, this is done by taking two separate exposures, then changing which shutter is used. A cross-correlation between the images is made, and the best focus is selected. This focus is dependent on various factors (such as temperature and instrument conditions) and should be performed before an observing run.

Dome flat images are then taken. This is performed by illuminating a blank white screen on the dome interior with a spectrum-featureless lamp, followed by exposing the spectrograph for several seconds in order to obtain sufficient counts (peak count of approximately 40 - 50 thousand). This procedure corrects for CCD response and accounts for sensitivity changes at all spatial scales, since the CCD is not 100% efficient in converting photons of various wavelengths to counts (efficiency varies with wavelength, and is important for obtaining spectra). Dome-flats are chosen over sky-flats since there are absorption features present in the solar spectrum.

After all calibration images are obtained, observations may begin. The

Table 3.1: X-ray sources from XMM-Newton dataset MB1 cross matched with available photometric dataset mb02 (Harris, 2007). The R.A. and Dec. locations are provided by the photometric data. The magnitude values are given in the *C, R* and *I* bands, with associated errors. Forty one optical sources have been matched in this field.

Harris ID	M1[a]	M1 dist[b]	M2[a]	M2 dist[b]	PN[a]	PN dist[b]	R.A. [J2000]	Dec. [J2000]	*C*	*R*	*I*
6891	24	0.8601	-	-	58	2.4354	01 45 22.0	-74 31 24	-	22.74±0.08	21.92±0.08
6900	24	0.2401	-	-	-	-	01 45 22.1	-74 31 25	-	21.72±0.08	20.83±0.07
7585	-	-	-	-	38	2.5347	01 45 34.6	-74 30 23	22.06±0.07	21.52±0.03	21.04±0.04
8242	5	1.0887	4	1.0257	-	-	01 45 47.1	-74 25 32	21.87±0.05	21.13±0.02	20.48±0.03
8277	-	-	-	-	11	0.9149	01 45 47.8	-74 25 29	22.96±0.11	22.30±0.04	22.10±0.09
9712	-	-	-	-	48	2.0843	01 46 13.6	-74 31 58	22.98±0.07	22.17±0.03	21.85±0.06
9719	-	-	-	-	48	2.2063	01 46 13.9	-74 31 56	22.82±0.08	22.43±0.05	22.29±0.11
9735	-	-	-	-	48	0.3166	01 46 14.2	-74 31 58	21.63±0.05	21.52±0.03	21.21±0.05
10107	11	1.0003	-	-	-	-	01 46 21.2	-74 42 12	19.19±0.05	16.57±0.03	15.85±0.03
10546	17	1.4322	30	1.7053	-	-	01 46 30.1	-74 27 50	22.89±0.11	22.17±0.04	21.90±0.08
11390	6	1.604	6	2.6571	5	2.0767	01 46 47.2	-74 40 16	20.50±0.03	20.05±0.02	19.88±0.03
12608	-	-	-	-	57	1.6165	01 47 09.2	-74 23 11	-	22.39±0.05	21.95±0.10
13970	8	1.2047	12	1.5672	9	2.074	01 47 34.8	-74 29 37	-	21.56±0.08	20.58±0.08
14220	-	-	11	2.425	8	2.8879	01 47 39.4	-74 40 17	20.75±0.03	20.21±0.03	19.90±0.03
14913	-	-	16	1.6909	-	-	01 47 53.9	-74 43 55	23.58±0.12	22.45±0.05	21.56±0.07
15572	-	-	20	2.1849	22	2.7823	01 48 06.4	-74 35 24	21.72±0.07	20.94±0.03	20.48±0.03
15775	-	-	21	1.2039	30	1.3941	01 48 10.3	-74 38 08	-	21.50±0.05	20.51±0.05
15795	-	-	-	-	6	1.7664	01 48 10.8	-74 33 44	-	22.44±0.06	22.08±0.09
15943	-	-	-	-	27	1.3583	01 48 13.3	-74 21 03	22.57±0.07	21.86±0.03	21.66±0.06
16274	4	2.2417	-	-	-	-	01 48 19.7	-74 20 07	-	21.84±0.03	21.02±0.04
16353	-	-	28	0.9644	-	-	01 48 21.6	-74 43 17	19.66±0.03	19.36±0.03	18.98±0.03
16369	-	-	-	-	32	2.4926	01 48 21.9	-74 19 17	21.75±0.06	21.17±0.03	20.85±0.04
17188	2	1.3188	3	0.1929	3	1.2605	01 48 37.8	-74 25 22	22.60±0.07	21.73±0.04	20.84±0.05
18332	-	-	-	-	53	2.9665	01 49 00.0	-74 37 32	22.64±0.08	22.05±0.04	21.83±0.07
18584	1	1.1687	1	1.6042	1	1.7966	01 49 05.0	-74 29 51	21.45±0.04	20.18±0.02	19.78±0.02
18986	-	-	-	-	16	1.4466	01 49 12.6	-74 22 40	23.11±0.11	22.36±0.05	21.98±0.08
19005	-	-	-	-	16	2.5702	01 49 13.0	-74 22 40	-	22.02±0.06	21.23±0.07
19188	-	-	-	-	55	1.4083	01 49 16.7	-74 31 25	-	22.77±0.06	-
19195	-	-	-	-	55	0.3701	01 49 16.8	-74 31 24	-	23.23±0.09	21.72±0.07
21825	-	-	-	-	59	1.7791	01 50 04.6	-74 37 36	21.39±0.05	20.22±0.02	19.79±0.02
21851	-	-	-	-	40	2.1783	01 50 05.3	-74 25 47	-	22.53±0.05	21.75±0.06
22411	-	-	-	-	19	2.451	01 50 14.8	-74 19 30	-	22.50±0.05	21.07±0.05
22570	-	-	-	-	7	2.9338	01 50 17.6	-74 30 13	22.22±0.05	21.68±0.03	21.06±0.04
24195	12	2.1165	-	-	-	-	01 50 46.8	-74 25 31	21.72±0.04	21.68±0.03	21.38±0.05
24225	12	2.6228	-	-	-	-	01 50 47.4	-74 25 28	-	23.39±0.09	22.89±0.18
24786	-	-	-	-	17	1.601	01 50 58.6	-74 25 09	21.70±0.04	20.50±0.02	20.07±0.02
25656	-	-	-	-	12	2.7446	01 51 16.6	-74 29 54	23.45±0.12	22.70±0.05	22.36±0.07
25668	-	-	10	2.4479	12	1.9958	01 51 16.7	-74 29 53	21.52±0.04	21.07±0.02	20.84±0.03
25734	9	1.5011	10	2.5895	-	-	01 51 17.9	-74 29 54	22.16±0.06	21.86±0.03	21.70±0.06
26969	-	-	-	-	26	2.7605	01 51 41.2	-74 27 17	21.76±0.04	21.52±0.03	20.87±0.03

Notes: [(a)] M1, M2 and PN are the source IDs of the XMM EPIC cameras, where M1 and M2 are MOS1 and MOS2, respectively. [(b)] The separation distance in arcseconds between the XMM source and the photometric source.

Table 3.2: X-ray sources from XMM-Newton dataset MB2 cross matched with available photometric dataset mb03 (Harris, 2007). Same as figure 3.1. Fifty one optical sources have been matched in this field.

Harris ID	M1[a]	M1 dist[b]	M2[a]	M2 dist[b]	PN[a]	PN dist[b]	R.A. [J2000]	Dec. [J2000]	C	R	I
2580	6	1.6319	4	1.9974	-	-	01 57 01.2	-73 00 46	-	20.00±0.02	19.45±0.02
3411	-	-	-	-	59	1.6139	01 57 25.6	-72 59 34	21.28±0.05	20.49±0.02	20.24±0.03
3839	-	-	-	-	45	2.9952	01 57 38.2	-73 02 30	20.91±0.04	20.40±0.02	19.93±0.03
3873	-	-	-	-	45	0.6672	01 57 39.0	-73 02 29	-	22.99±0.09	22.79±0.15
4386	-	-	29	1.7527	26	2.8926	01 57 54.1	-73 02 15	21.32±0.04	20.87±0.02	20.67±0.03
4414	28	1.2342	-	-	26	1.6108	01 57 55.1	-73 02 14	-	23.00±0.07	21.31±0.05
4720	4	2.16	-	-	5	2.0737	01 58 04.2	-72 51 06	20.76±0.04	20.44±0.03	19.95±0.02
4925	16	2.7069	-	-	-	-	01 58 11.2	-73 02 57	-	21.99±0.05	21.85±0.08
5355	18	1.6566	-	-	-	-	01 58 24.9	-73 07 59	20.16±0.08	16.47±0.03	14.88±0.03
5460	-	-	32	1.399	-	-	01 58 28.0	-73 02 06	-	22.78±0.06	22.18±0.07
5701	-	-	-	-	69	2.8358	01 58 35.3	-73 03 42	-	22.74±0.10	22.56±0.15
5851	-	-	12	1.6418	11	2.9759	01 58 39.9	-72 59 02	-	22.55±0.06	21.98±0.08
6072	-	-	-	-	51	0.561	01 58 46.3	-72 59 28	-	22.06±0.08	21.68±0.07
6151	33	1.3296	-	-	30	2.2092	01 58 48.6	-73 02 26	-	21.97±0.04	21.43±0.05
6306	36	2.2119	-	-	-	-	01 58 54.1	-72 53 44	-	22.67±0.07	21.00±0.04
6312	-	-	-	-	22	2.6212	01 58 54.4	-72 53 45	-	22.24±0.07	21.57±0.06
6326	11	1.6281	10	2.6626	-	-	01 58 54.8	-73 07 12	22.58±0.12	21.16±0.03	20.34±0.03
6333	-	-	-	-	22	1.8809	01 58 55.1	-72 53 46	-	20.19±0.03	19.24±0.02
6925	32	0.8617	34	1.5404	27	0.6862	01 59 15.5	-72 51 38	-	22.82±0.09	21.91±0.09
6947	2	1.3316	2	2.2175	2	1.9871	01 59 16.3	-73 08 27	20.01±0.03	19.50±0.03	19.01±0.04
7571	12	2.4013	5	0.6417	7	1.1572	01 59 37.7	-73 05 25	20.14±0.03	19.77±0.02	19.41±0.02
7623	-	-	33	1.9396	-	-	01 59 39.3	-72 47 13	-	22.44±0.07	21.85±0.09
7677	-	-	-	-	44	1.5519	01 59 41.1	-72 47 09	22.46±0.09	21.89±0.04	21.63±0.06
8431	23	1.3167	-	-	52	2.0355	02 00 11.0	-72 48 07	22.53±0.12	21.93±0.04	21.07±0.05
8552	-	-	31	1.9322	-	-	02 00 15.3	-73 09 49	20.42±0.03	20.15±0.02	19.88±0.02
8718	-	-	-	-	58	2.8165	02 00 21.2	-72 47 03	-	23.23±0.10	22.77±0.15
8772	10	2.6899	20	2.0203	13	2.7121	02 00 23.2	-73 02 18	-	22.66±0.06	21.71±0.06
8927	-	-	35	2.4784	-	-	02 00 28.3	-72 50 35	-	22.59±0.06	21.80±0.07
8966	27	2.5246	-	-	-	-	02 00 29.5	-72 49 58	20.51±0.04	20.21±0.02	20.00±0.02
9182	-	-	-	-	38	2.9272	02 00 37.7	-73 03 50	22.12±0.10	21.74±0.04	21.10±0.03
9285	-	-	14	2.227	16	1.9969	02 00 41.6	-73 05 14	21.43±0.04	20.76±0.02	20.53±0.03
9549	-	-	37	2.7182	-	-	02 00 51.4	-73 05 45	-	21.99±0.06	-
9606	8	1.2151	9	1.333	9	2.2277	02 00 53.7	-72 58 51	21.97±0.07	21.33±0.03	21.02±0.04
9650	-	-	-	-	46	2.6951	02 00 55.2	-73 08 27	-	21.69±0.05	-
9654	-	-	-	-	42	1.3979	02 00 55.2	-72 54 24	20.92±0.04	21.08±0.03	20.95±0.03
9967	1	1.8839	-	-	1	2.5708	02 01 07.3	-72 55 46	17.66±0.02	17.36±0.02	16.69±0.03
10238	-	-	-	-	20	1.4985	02 01 17.9	-72 55 18	-	21.63±0.03	21.11±0.03
10264	-	-	-	-	28	1.7496	02 01 18.9	-72 58 29	-	22.61±0.08	21.78±0.05
10407	22	0.8615	-	-	18	1.9676	02 01 24.1	-72 55 21	-	22.09±0.07	21.46±0.04
10426	30	2.9592	-	-	-	-	02 01 25.2	-73 02 15	22.07±0.08	21.95±0.06	21.45±0.06
10589	-	-	-	-	41	2.6238	02 01 31.2	-72 46 56	21.19±0.05	20.33±0.03	19.62±0.04
10707	-	-	6	2.2915	-	-	02 01 36.1	-73 08 21	19.31±0.03	18.76±0.02	18.50±0.02
10744	21	1.8976	-	-	-	-	02 01 37.2	-72 51 58	19.75±0.03	19.55±0.02	19.38±0.02
11143	-	-	16	1.8688	-	-	02 01 51.6	-73 05 45	-	22.72±0.08	21.99±0.08
11758	-	-	-	-	31	2.9946	02 02 17.4	-72 52 23	22.43±0.08	21.34±0.03	20.56±0.03
12060	-	-	13	2.5341	21	2.6542	02 02 28.4	-72 52 07	21.48±0.05	20.84±0.02	20.58±0.03
12101	-	-	-	-	15	2.9099	02 02 30.3	-73 08 22	22.04±0.09	21.46±0.04	21.05±0.04
12171	25	2.0338	-	-	-	-	02 02 32.5	-72 59 45	21.93±0.07	20.96±0.03	20.34±0.04
12271	15	2.5422	-	-	-	-	02 02 36.6	-73 01 48	20.15±0.03	19.70±0.02	19.34±0.02
12412	-	-	25	0.5139	-	-	02 02 42.5	-72 59 47	-	21.64±0.03	21.33±0.04

Notes: [a] M1, M2 and PN are the source IDs of the XMM EPIC cameras, where M1 and M2 are MOS1 and MOS2, respectively. [b] The separation distance in arcseconds between the XMM source and the photometric source.

Table 3.3: X-ray sources from XMM-Newton dataset MB3 cross matched with available photometric dataset mb06 (Harris, 2007). Same as figure 3.1. Forty optical sources have been matched in this field.

Harris ID	M1[a]	M1 dist[b]	M2[a]	M2 dist[b]	PN[a]	PN dist[b]	R.A. [J2000]	Dec. [J2000]	C	R	I
1750	15	0.9804	13	1.7561	-	-	02 21 07.6	-73 48 59	21.44±0.04	21.36±0.03	20.75±0.05
2181	14	2.8244	-	-	-	-	02 21 30.8	-74 02 19	22.33±0.05	21.68±0.03	20.98±0.04
2225	-	-	-	-	40	2.3097	02 21 32.7	-73 59 08	-	23.06±0.07	-
2583	-	-	-	-	46	2.3866	02 21 51.8	-73 54 20	-	20.72±0.02	19.25±0.03
2596	27	2.6119	24	1.3661	45	2.6373	02 21 52.4	-73 50 57	23.50±0.10	20.99±0.04	20.20±0.05
2967	-	-	32	1.8002	28	0.3941	02 22 11.5	-74 02 39	21.78±0.04	21.21±0.04	20.61±0.04
3296	-	-	36	2.4413	35	0.6905	02 22 29.3	-74 01 22	19.61±0.05	16.67±0.02	15.73±0.02
3656	-	-	-	-	56	2.7978	02 22 47.2	-73 46 15	23.51±0.13	21.67±0.08	20.97±0.07
3678	3	2.358	-	-	2	2.8008	02 22 48.1	-73 48 57	22.21±0.06	19.31±0.02	18.48±0.02
3679	3	1.6858	5	1.3627	2	2.3359	02 22 48.1	-73 49 00	-	20.70±0.05	19.89±0.05
3689	3	1.1893	5	1.3884	2	0.4612	02 22 48.7	-73 48 59	21.93±0.06	20.11±0.05	19.39±0.05
3753	-	-	-	-	57	1.0099	02 22 52.4	-73 43 28	21.92±0.06	19.55±0.04	18.84±0.04
3815	4	1.0235	4	2.2701	3	0.2949	02 22 55.6	-73 47 54	20.80±0.04	20.27±0.02	20.14±0.03
4133	-	-	9	1.5109	8	0.4605	02 23 08.6	-73 48 01	21.87±0.05	21.21±0.03	20.95±0.04
4343	21	2.8369	19	0.9846	14	2.4242	02 23 19.9	-73 58 12	22.00±0.05	21.70±0.02	21.13±0.04
4382	-	-	-	-	15	1.9983	02 23 21.8	-73 47 57	23.41±0.11	22.08±0.08	21.03±0.09
4432	-	-	34	2.0228	-	-	02 23 24.9	-73 53 03	-	22.22±0.07	21.01±0.08
4584	13	0.9814	22	1.5328	17	1.1868	02 23 33.1	-73 56 03	22.98±0.07	22.39±0.04	21.72±0.08
4703	7	1.3981	8	0.2584	6	1.3298	02 23 39.8	-73 51 33	23.50±0.11	20.95±0.04	20.25±0.05
4888	-	-	-	-	25	0.7515	02 23 52.1	-74 02 53	23.55±0.12	22.15±0.05	21.41±0.06
4915	-	-	6	1.5667	12	0.4545	02 23 53.7	-74 01 55	23.37±0.09	22.15±0.05	21.42±0.06
5057	16	1.3862	16	2.3458	-	-	02 24 01.7	-73 53 17	23.74±0.10	22.27±0.05	21.84±0.08
5075	-	-	-	-	63	1.3354	02 24 02.5	-73 49 37	22.41±0.06	21.88±0.03	21.62±0.06
5174	-	-	37	2.8491	-	-	02 24 07.0	-73 47 17	-	22.01±0.05	20.27±0.03
5437	-	-	-	-	21	2.6384	02 24 22.9	-73 51 15	14.69±0.03	15.07±0.02	15.02±0.02
5547	1	0.8949	1	1.0014	4	0.3105	02 24 27.6	-73 54 08	-	14.46±0.03	-
5638	-	-	-	-	20	1.1766	02 24 31.5	-73 44 53	23.33±0.08	22.19±0.04	21.47±0.05
5780	-	-	-	-	27	0.9173	02 24 39.8	-74 00 48	22.17±0.06	20.89±0.04	20.88±0.04
5794	-	-	-	-	43	2.0182	02 24 40.6	-74 03 34	20.37±0.08	16.87±0.02	15.48±0.02
5798	26	1.8501	-	-	-	-	02 24 40.8	-73 58 05	22.03±0.04	21.39±0.03	21.13±0.04
5832	-	-	-	-	31	1.1905	02 24 42.6	-73 47 18	21.86±0.04	21.61±0.03	21.18±0.04
6259	24	2.686	17	0.9541	18	1.0262	02 25 05.1	-74 05 15	22.02±0.04	21.21±0.05	20.39±0.07
6311	-	-	-	-	10	2.7108	02 25 07.8	-74 00 33	22.15±0.05	21.03±0.04	20.31±0.04
7057	-	-	-	-	42	2.8528	02 25 43.8	-74 03 55	-	21.22±0.06	20.25±0.06
7151	12	1.4874	-	-	11	0.7664	02 25 48.6	-73 52 46	20.43±0.03	19.82±0.02	19.33±0.02
7283	-	-	-	-	52	2.7695	02 25 55.8	-73 50 58	21.05±0.03	20.39±0.02	20.10±0.03
7586	23	1.6595	-	-	23	0.876	02 26 11.3	-73 48 10	21.88±0.04	21.12±0.03	20.79±0.04
7984	5	1.8882	15	2.051	7	0.9141	02 26 33.7	-73 51 37	19.22±0.03	18.92±0.02	18.55±0.02
8663	-	-	-	-	60	2.9697	02 27 06.4	-73 49 14	-	22.11±0.06	21.13±0.05

Notes: [(a)] M1, M2 and PN are the source IDs of the XMM EPIC cameras, where M1 and M2 are MOS1 and MOS2, respectively. [(b)] The separation distance in arcseconds between the XMM source and the photometric source.

final step before reduction may be performed is to clean the spectra of cosmic rays. This is done using a robust cosmic ray cleaning algorithm, created by van Dokkum (2001). Once all spectra are cleaned of cosmic rays, reduction in IRAF (Image Reduction and Analysis Facility) using the calibration images may be performed.

3.3.1 Reduction Using IRAF

An IRAF reduction script designed for the South African Astronomical Observatory (SAAO) 1.9 m Telescope by Macri (2016) was used for image correction. The images are initially trimmed in order to remove the readout pixels. Due to the inherent noise within the CCD, certain pixels and columns will have charge which is added to the spectra images. To remove this effect, an averaged bias image is created using the `ccproc` command within IRAF. This average bias frame is created from all bias images taken before the observation run. The average bias frame is then subtracted from all the spectra images.

To correct for pixel-to-pixel variations in sensitivity, the spectral images are divided by the flat-fields. Before an averaged flat-field is created, it is first bias subtracted. Similarly to the averaged bias frame, an averaged flat-field is created from all flat-field images taken before the observations. After the flat-field corrections have been applied, wavelength calibration may then proceed.

The atmosphere contributes in absorption to the spectra obtained. Since the spectrum of an observed object will only occupy several pixel rows across the CCD, the rest of the CCD will contain the background spectrum only. The background spectrum above and below the object spectrum is extracted, then subtracted from the object spectrum. This process converts a two dimensional image into a one dimensional spectrum that is corrected for background absorption. The `apall` package within IRAF performs background subtraction and spectrum extraction.

Before and after each exposure of an object, an arc calibration image is taken. This was done by exposing the spectrometer to a copper argon lamp. The emission lines of the lamp are well known, thus IRAF is able to create a pixel-to-wavelength fit so that the background corrected spectra obtained may be converted from pixel number to wavelength. Both `apall` and `dispcor` packages are used for the conversions.

The signal-to-noise ratios (SNR) are dependent on several factors, including the magnitude of the object observed, length of exposure, weather conditions, etc. The SNR of each spectra (figure 3.1) can be found in Table 3.4.

3.4 Spectroscopic Observations

Grating 7 is a low resolution, wide wavelength coverage grating. The lines are ruled at 300 lines/mm, with a resolution of 19.1Å. It gives a wavelength range of 5000 Å. A grating angle of 16.10 units allows for a spectrum to be taken between 3400-9050 Å. The low resolution allows for shorter exposures to be taken, and simplifies the initial classification (since stellar and galactic spectra are easily discernible over this wavelength range).

Interesting sources are then followed up with a higher resolution grating (grating 4). This grating has a wavelength range of 1250 Å and has lines ruled at 1200 lines/mm, with a resolution of 3.1 Å. A grating angle of 5 units was chosen, which allows for a spectrum to be taken between 3880-5050 Å. This covers the region typically used for spectral classification.

A list of all objects that were followed up with optical spectroscopy can be found in Table 3.4. The object names are the same used in Harris (2007). The table contains the exposure times for each spectra, the number of exposures for each object and the grating chosen. The grating name is unique to this spectrograph, and simply determines the wavelength range and resolution of spectra.

Table 3.4: Spectroscopic observations taken using SpUpNIC taken in February, 2019. Object names are the same used in Harris (2007). The R magnitude (R Mag.) is obtained from Harris, and is rounded to one decimal place. The exposure times (Exp.) and number of exposures (No. Exp.) for each source is given, along with the grating used. The range of signal-to-noise (SNR) values is also shown. Slit width for all observations was set to 2.10″. Grating 7 has a resolution of 19.1 Å and grating 4 has a resolution of 3.1 Å. Observing conditions for each object is shown in Table 3.4. Spectra can be found in figure 3.1. Spectra of sources observed on 10 February were reduced by Trystan Lambert.

Date	Object	R Mag.	Exp. [s]	No. Exp.	SNR	Grating	λ Range [Å]
7	5355	16.5	600	2	8.7 ± 4.1	7	4000 - 7000
	9967	17.4	900	1	18.1 ± 2.1		
	3296	16.7	900	1	12.9 ± 4.7		
10	5437	15.1	600	2	41.2 ± 5.7		
	5547	14.5	600	1	28.2 ± 12.0		
	5794	16.9	900	1	8.0 ± 4.1		
11	5437	15.1	900	2	43.5 ± 1.1	4	3900 - 5000
12							

Table 3.5: Observation conditions for each object presented in Table 3.4. Airmass is calculated as sec(z) where z is the azimuthal angle. RST is the relative sky temperature, lower values indicates higher cloud coverage. Seeing is in arcseconds. Seeing on the 11th of February was unavailable.

Date	Object	Airmass [sec(z)]	RST [K]	Seeing [″]
7	5355	1.5821	40.46	1.32
	9967	1.6501	37.85	1.18
	3296	1.7396	39.15	1.44
10	5437	1.5785	32.04	2.01
	5547	1.6415	31.61	1.72
	5794	1.6819	32.62	1.46
11	5437	1.6634	34.22	N/A
12		1.4789	39.73	1.7

3.5 Spectroscopic Results

For this section, the package `rvsao` (Mink and Kurtz, 1998) for `IRAF` is used to determine the absorption and emission lines from spectra; figures from Townsend et al. (2011) are used to determine absorption lines in shorter wavelength spectra. The spectral features are used to determine the redshift of each object. Due to atmospheric absorption lines, wavelengths greater than 7000 Å are ignored. As shown in Table 3.4, a higher resolution grating was used to follow up source 5437.

All observed spectra are shown in figure 3.1, with additional information (such as exposure times, magnitudes, etc.) presented in Table 3.4. A higher resolution spectrum of object 5437 is also found at the bottom in figure 3.1, which is a combination of two spectra obtained on consecutive nights.

The associated X-ray source that matched with object 5437, is source PN 21 from dataset MB3. The separation distance between these objects is 2.6″. However, this same X-ray source was also found to match 3XMM-DR6 J022422.8−735116 (an AGN in the 3XMM-DR6 catalogue Rosen et al., 2016), with a separation distance of 1.4″. The X-ray spectra of this source will be discussed in the following section in order to determine if the source is a neutron star or an AGN.

All spectra have been normalised, except for objects 5355, 5547 and 5794, the broad emission and absorption made it particularly difficult to do so.

The classification of the spectra contained within this chapter will be discussed in the following chapter 4.1, comparing them to spectral standards found in the SDSS cross-correlation templates (Sloan Digital Sky Survey).

The SNR for each spectrum will be quoted within each caption, along with the 1σ standard deviation of the SNR across all wavelengths. Refer to appendix D for a detailed breakdown of the SNR calculations.

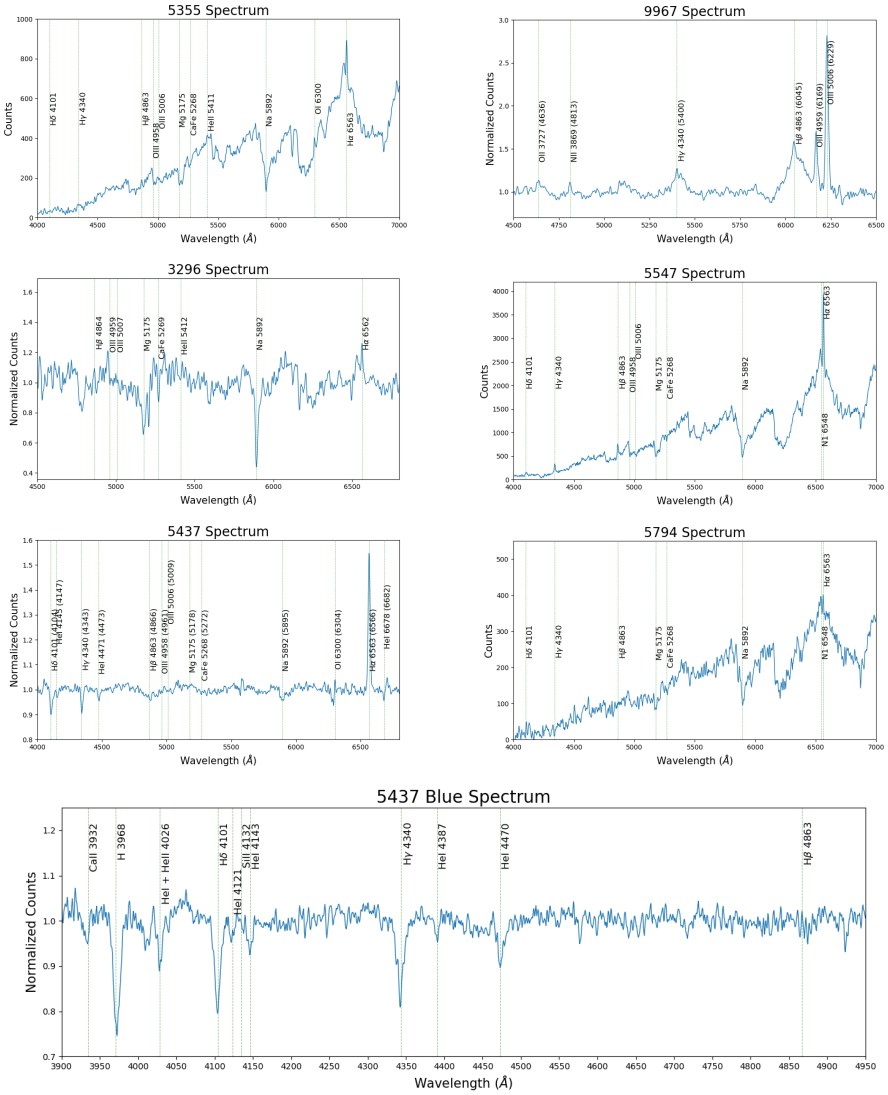

Figure 3.1: Broad spectra of all six observed sources, including a narrow spectrum of object 5437. The SNR ranged from 4 to 45, depending on exposure time. Additional information on each object can be found in Table 3.4, detailed discussion on each object can be found in chapter 4. Certain objects are redshifted, with observed absorption/emission lines shown in brackets.

Chapter 4

Interpretation Of Results

4.1 Spectral Analysis

The following section will be a discussion on the results of each spectrum. Broadband spectra listed previously in section 3.5 (around 4000 Å to 7000 Å) will be compared using the absorption and emission features to the SDSS cross-correlation templates (Sloan Digital Sky Survey) and the Stellar Spectral Flux Library (Pickles, 1998). The narrow blue spectrum of object 5437 (bottom of figure 3.1) will be compared to an alternative classification system designed for the lower metallicity environment found in the Magellanic Bridge (Evans et al., 2004). Due to time constraints, the spectra have not been flux calibrated. For general classifications, this is not required.

4.1.1 Object 5355

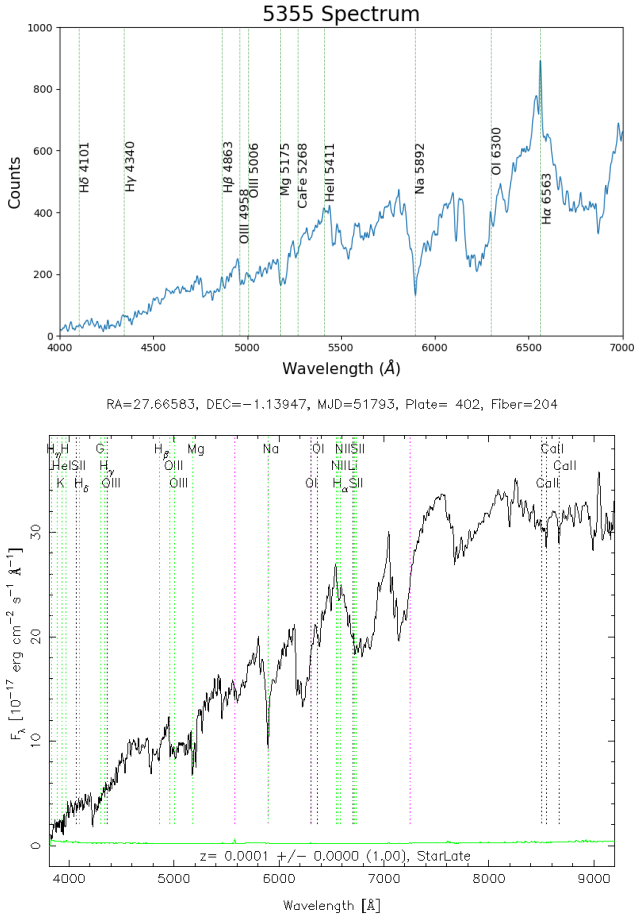

Figure 4.1: *Top*: Spectrum of object 5355 in field MB2, which is the optical counterpart to X-ray source MOS1 18. *Bottom*: SDSS spectrum of an M1 dwarf.

The presence of a strong Na absorption line in object 5355 (figure 4.1), along with titanium monoxide (TiO, responsible for many of the absorption features, lines not shown since it will clutter the graph) indicates it is an early M1-M3 dwarf. The Hα emission gives a redshift velocity of -4.35 ± 0.01 km/s. In addition, when comparing magnitudes to known M dwarfs Lépine and Gai-

dos (2011), using the spectral classification of M1-M3, the distance obtained is 13.6 - 51.1 pc. The radial velocity and magnitude are consistent with an M dwarf located in the Milky way.

Featuring emission lines Hα, and small Hβ, the rest of the spectrum is dominated with metal absorption. The X-ray counterpart of object 5355 is MB2 MOS1 18, and according to Table 2.2, the source is categorised as soft, hard and ultrahard categories within 1σ error.

4.1.2 Object 9967

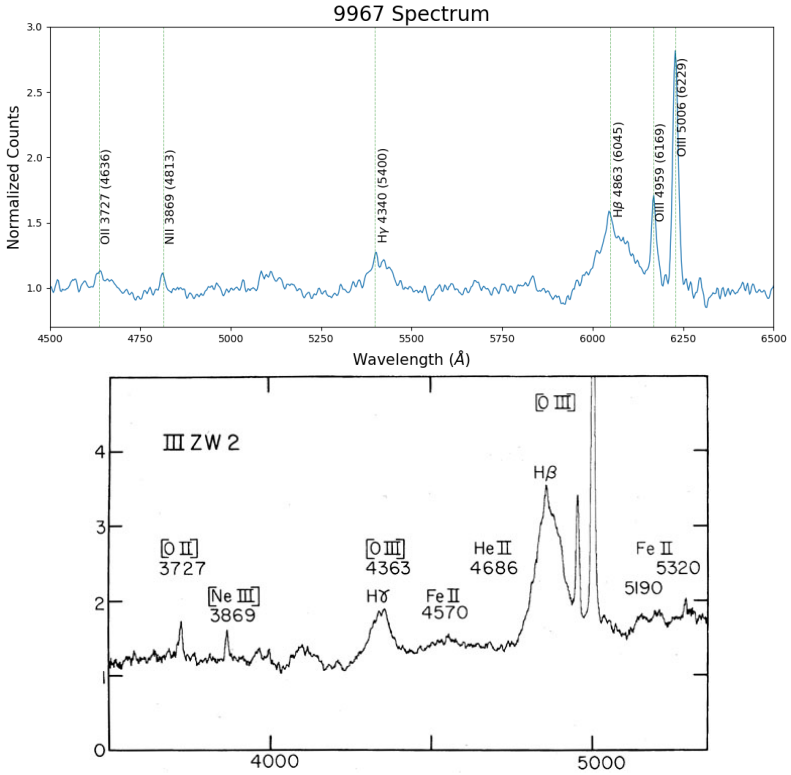

Figure 4.2: *Top*: Spectrum of object 9967 in field MB2, which is the optical counterpart to X-ray sources MOS1 1 and PN 1. *Bottom*: Spectrum of III Zw 002 (NASA/IPAC Extragalactic Database), a Seyfert 1 galaxy (Neugebauer et al., 1979).

Broad Hγ and Hδ emission lines in object 9967 (figure 4.2) are observed, along with narrower OIII emission lines. The Fe lines are difficult to find due to the noisy spectrum.

Redshift is calculated by taking the observed emission/absorption lines and comparing to rest wavelengths of known elements by using the following equation:

$$z = \frac{\lambda - \lambda_0}{\lambda_0} \tag{4.1}$$

where λ is the observed wavelength of an emission/absorption feature, and λ_0 is the rest wavelength of the emission/absorption feature. The redshift of object 9967 may then be calculated by comparing the spectra (top of figure 4.2) to a known Seyfert 1 galaxy, III Zw 002 (NASA/IPAC Extragalactic Database, bottom of of figure 4.2). A redshift value of $z = 0.244 \pm 0.002$ is obtained.

Using a redshift of $z = 0.244 \pm 0.002$ returns a distance modulus of 40.51 ± 0.02 and a luminosity distance of $D_L = 1.263 \pm 0.014$ Gpc (assuming a flat universe, and ignoring reddening from dust). From Table 3.2, the CRI magnitudes are 17.66, 17.36 and 16.69, respectively. Using the aforementioned distance modulus, the absolute CRI values are -22.85, -23.15 and -23.82, respectively. From the USNO-A2.0 catalogue on Vizier (Monet, 1998), the B and R magnitudes are 17,4 and 17.1, respectively. This results in an absolute B and R magnitude of -23.1 and -23.4, respectively. These values are consistent with the luminosity function of Seyfert 1 galaxies (Osterbrock, 1984).

The combined X-ray flux of this source (in the 0.2-12 keV range) in the MOS1 (source 1 in Table C.5) and PN cameras (source 1 in Table C.7) is:

$$F_{9967} = (2.2 \pm 0.1) \times 10^{-12} \text{ erg cm}^{-2} \text{ s}^{-1} \tag{4.2}$$

Using the luminosity distance obtained from the redshift, D_L (in cm), the

X-ray luminosity may be obtained as follows:

$$L_{M19967} = F_{9967} \times 4\pi D_L^2 \tag{4.3}$$

$$L_{M1\ 9967} = (4.2 \pm 0.2) \times 10^{44}\ \text{erg s}^{-1} \tag{4.4}$$

$$\log(L_{M1\ 9967}) \sim 44.6\ \text{erg s}^{-1} \tag{4.5}$$

These values are consistent with the X-ray luminosity function of AGN (Georgakakis et al., 2014, figure 6, given in the 2-10 keV range).

According to the hardness ratio obtained from the MOS1 camera, the source is classified as hard within the 1σ error (Table 2.2), but according to the HR values obtained from the PN camera, it falls within both the soft and hard categories.

4.1.3 Object 3296

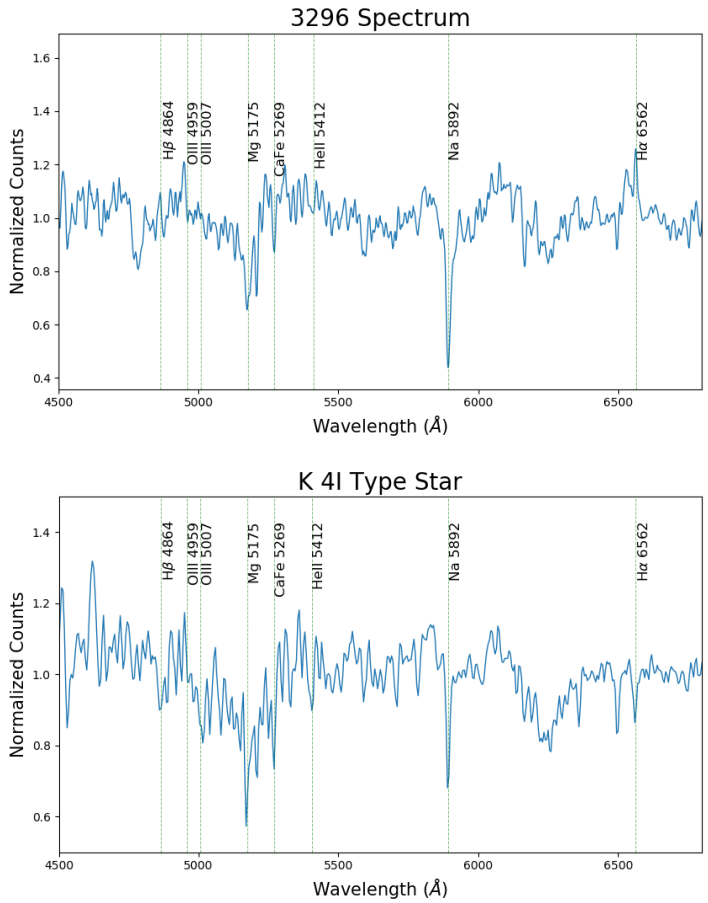

Figure 4.3: *Top*: Spectrum of object 3296 in field MB3, which is the optical counterpart to source 36 in the MOS2 camera and source 35 in the PN camera. *Bottom*: Spectrum of a K4 type star obtained from the Stellar Spectral Flux Library (Pickles, 1998).

The spectrum of object 3296 (figure 4.3) features a strong Na absorption line, along with a weaker Mg line. Hα is in emission, it is difficult to determine if Hβ is in emission. Comparing to the HR category Table 2.2 within 1σ error, the MOS2 source is categorised as soft, hard and ultrahard, while the

PN hardness ratios are only categorised as soft. The Hα line gives a redshift velocity of 5.48 ± 0.1 km/s. An estimated distance of 36 - 136 pc is calculated by comparing the magnitude to other known K stars (Lépine and Gaidos, 2011). Both the radial velocity and magnitude indicate the star resides in the Milky Way.

The K-type star has all the same features, except that the Na absorption is not as strong, and the Balmer lines are in absorption. The Hα emission makes it difficult to classify the object accurately.

4.1.4 Object 5547

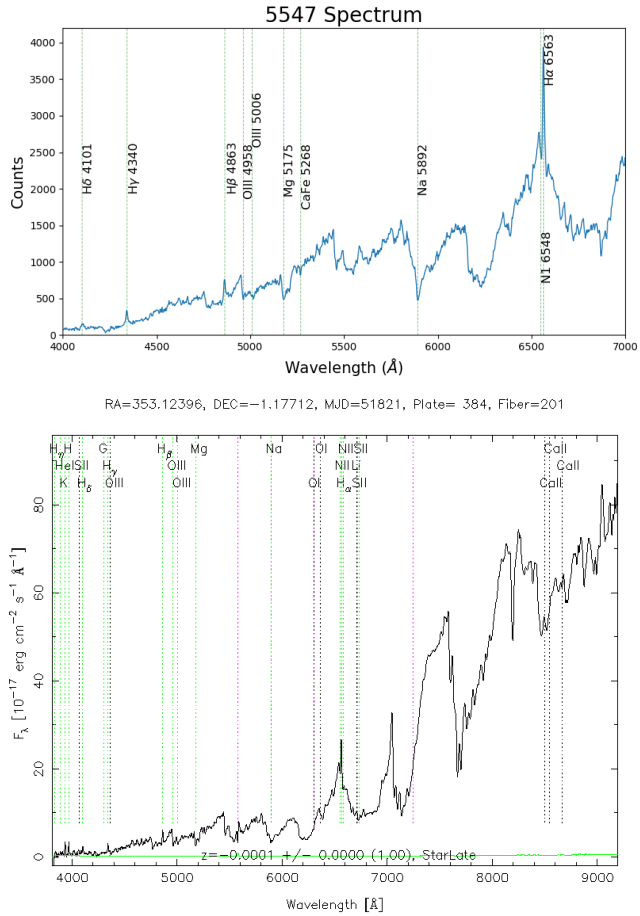

Figure 4.4: *Top*: Spectrum of object 5547 in field MB3, and is the optical counterpart to source 1 in the MOS1 and MOS2 cameras, and source 4 in the PN camera. *Bottom*: SDSS spectrum of an M5 dwarf.

The spectrum of object 5547 (figure 4.4) is similar to that of object 5794 (figure 4.5) and object 5355 (figure 4.1). The spectrum contains a broad Na absorption line, along with Balmer emission, of which Hα is the strongest. Most of the other absorption features are believed to be caused by TiO. This object is later than an M1 dwarf, but is earlier than an M5 dwarf, therefore

it is constrained as an M2-M4 dwarf. No significant redshift was observed. According to the HR category Table 2.2, the sources in all cameras fall within the soft category (1σ error, this is consistent with coronal X-ray emission from flare stars). The Hα emission gives a redshift velocity of 17.82 ± 0.01 km/s. A distance of 3 - 13 pc is calculated when comparing magnitudes to other M dwarfs (Lépine and Gaidos, 2011). These values are consistent with an M dwarf located in the Milky way.

4.1.5 Object 5794

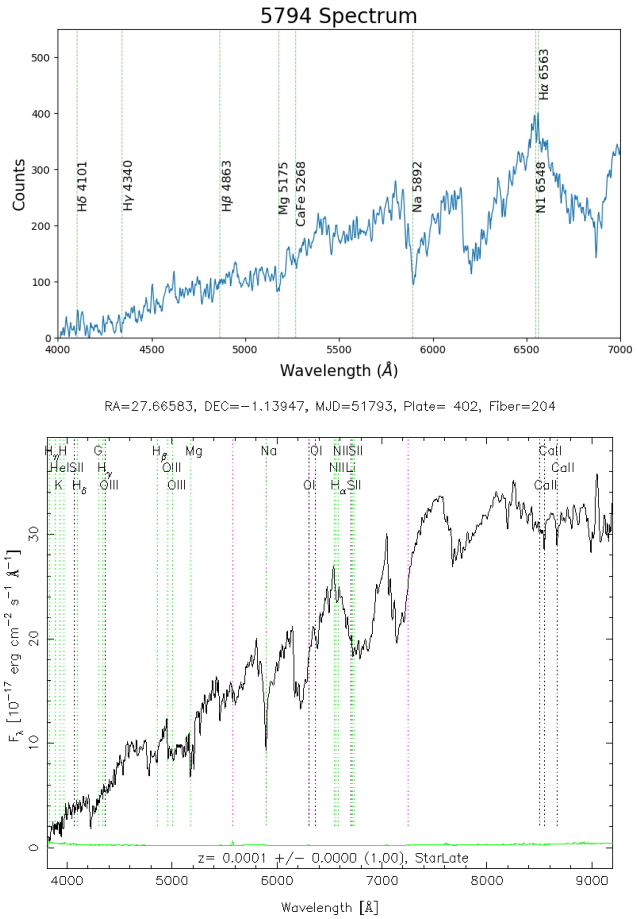

Figure 4.5: *Top*: Spectrum of object 5794 in field MB3, and is the optical counterpart to source 43 in the PN camera. *Bottom*: SDSS spectrum of an M1 dwarf.

The spectrum of object 5794 (figure 4.5) shows the typical M-type dwarf shape and features as seen in objects 5547 (figure 4.4) and 5355 (figure 4.1). The Na absorption is not as deep as the other observed M dwarfs. Balmer emission appears to be absent, Mg lines are observed, but are weak. Similarly to objects 5355 and 5547, many of the absorption features are believed to be

caused by TiO in the cooler atmosphere. This is most likely an early M dwarf, and is constrained to a spectral type of M1-M3. No significant redshift was observed. According to the HR category Table 2.2, the source falls within the soft category (1σ error, this is consistent with coronal X-ray emission from flare stars). The Hα line gives a redshift velocity of -74.82 ± 0.01 km/s. Comparing magnitudes to M stars from Lépine and Gaidos (2011), a distance of 16 - 61 pc is obtained. These values are consistent with an M-type star in the Milky Way.

4.2 Object 5437

Object 5437 matched within 2.6″ of X-ray source 21 in the PN camera in field MB3. The object was initially observed with a broad wavelength grating, a wavelength range from 4000 Å to 7000 Å (figure 4.6). A very strong Hα emission line with equivalent width (EW) of -10.3 ± 0.3 Å, where the error was calculated according to equation (6) in Cayrel (1988), where the signal-to-noise ratio is ~ 32, and the wavelength-to-pixel ratio is ~ 3.

The Hα emission line is redshifted to 6566.9 ± 0.1 Å, which prompted further investigation into obtaining a narrow spectrum from 3900 Å to 5100 Å(with a higher resolution of 3.1 Å). This will allow for a better classification of the object as well as constraining the redshift with a lower error.

By comparing several observed absorption lines (such as the Balmer series, He and Ca) to the rest wavelengths, an average redshift of $z = 6.2 \times 10^{-4}$ with a standard deviation of $\sigma_z = 2.0 \times 10^{-4}$ was found. Converting the redshift to velocity returns a value of $v = 186 \pm 60$ km/s. This velocity is within error of the recession velocity of the Small Magellanic Cloud (145.6 ± 0.6 km/s, and would be similar to the recession velocity of the Magellanic Bridge, McConnachie, 2012), however it is not definitive as to whether the observed object resides within the Magellanic Bridge.

Although source MB3 PN 21 is within the ultrahard category (as shown in

figure 2.14) in the HR_3 - HR_4 diagram, the large errors in the softer hardness ratios allow it to be categorised as soft and hard (for 1σ). A condition for a source to be labelled ultrahard (based on HR_3 and HR_4) is that it must not be categorised as soft (which is based on HR_2 and HR_3).

4.2.1 Spectral Analysis

The large Hα emission hints at the possibility of the star containing a circumstellar disk, which is commonly found in OB-type stars. The rapid spin of the OB-star allows material to reach high enough speeds that some of it can be put into a Keplerian orbit around the star. However, spectral classification will be done according to the bluer higher resolution spectrum, found in figure 4.7.

Comparing the broad spectrum to the Stellar Spectral library (Pickles, 1998), object 5437 has the same features found in other B-type stars. However, the absence of a strong sodium line suggests that the object may be in a lower metallicity environment. A stellar spectral survey of the SMC by Evans et al. (2004) is available, which contains an alternative spectral classification scheme better calibrated to a lower metallicity environment. Included is a redefinition of B-stellar spectra, which can be found in figure 4.8 (luminosity class Ib-II on the left, II-IV on the right).

As seen in the narrow blue spectrum (figure 4.7), hydrogen and helium are in absorption. Another possible line is 4132 Å (Si II), however it is difficult to confirm due to the noisy spectrum. This spectrum contains the same deep absorption H and He lines in figure 4.8, although determining the exact spectral type will be difficult due to measuring the differences in the shallower lines, which are heavily affected by the low signal-to-noise and low metallicity.

In figure 4.7, He I 4121 Å and 4143 Å are in absorption, this is present in spectral types B0-B5 II-Ib (left in figure 4.8, weakest at B0 and B5) and also present in spectral types B1-5 III (right in figure 4.8). In addition to this, there may be a possible Si II 4132 Å line between the previously mentioned

He I lines. This appears in spectral type B3, but is very weak, and is not present in luminosity class III.

The He line 4470 Å is approximately half the strength of Hγ 4340 Å, but is stronger than He I 4387 Å, this closely fits with spectral types B2.5Ib and B3Ib, as well as B1-5 III. In B2.5-B3 Ib and B3-B5 III spectral types, Mg II 4481 Å is present, however at the resolution of the spectrum the Mg line may have blended with the He I line.

According to luminosity class Ib-II (left in figure 4.8), these absorption lines constrain the spectral type to around B3Ib due to the presence of a Si II 4128 Å line. This classification also requires a Mg II 4481 Å line, which may be blended with He I 4470 Å, thus a higher resolution spectrum is required.

Comparing to luminosity class II-IV (right in figure 4.8), a He I line is absent in B0-5 II at 4470 Å, which is present in the spectrum of object 5437. The O II line (4650 Å) present in B1-3 III cannot be seen in the spectrum of the object, however this line is very weak, and difficult to distinguish from noise. Si II 4128 Å and 4132 Å absorption is present in B1-2 III, but similar to O II, is also weak. Taking all these possibilities into consideration, the object can be constrained to B1-5 III-IV according to these criteria. Taking the luminosity class Ib-II into consideration, this object may be constrained as a B0-5 II-IV star. Follow-up with a higher resolution spectrograph is required for a more accurate classification.

By comparing the observed emission lines in the higher resolution blue spectrum to the rest wavelengths (figure 4.7), the radial velocity is constrained to v = 186 $\pm$ 60 km/s. The redshift of the SMC is v = 145.6 $\pm$ 0.6 km/s, which falls within error, but is not a definitive test. However, the apparent magnitude and estimated distance may be used to calculate the absolute magnitude. The absolute magnitude may then be used to check if it is consistent with a B-type star of luminosity class III-IV (as classified above).

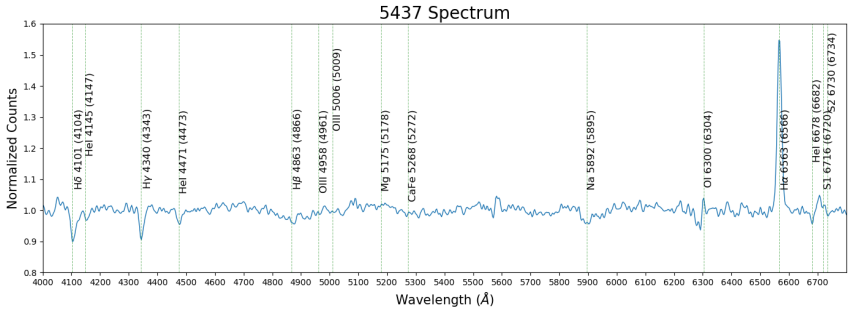

Figure 4.6: Broad spectrum of object 5437, as first presented in figure 3.1. The object has H and He in absorption (except for Hα), possibly with some metal absorption. An important feature is the very large Hα emission feature. Comparing to the SDSS database, this is a young star, and most likely a Be star, further analysis in the bluer spectrum must be conducted in order to determine its spectral type. In Be stars, the presence of an Hα emission line means that there is an active circumstellar disk, hence this is most possibly a Be star. The analysis of the blue spectrum can be found in figure 4.7.

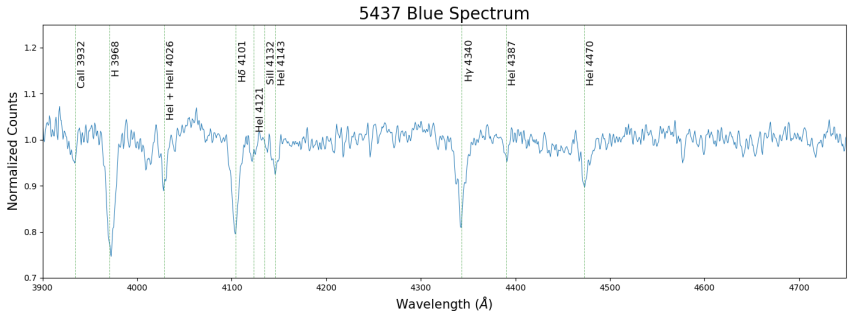

Figure 4.7: Combined narrow band spectrum of object 5437 taken between 3900 Å to 4750 Å, taken on two consecutive nights, as first presented in figure 3.1. Deep H absorption lines can be found at 3968 Å, 4101 Å and 4340 Å. Helium absorption lines can be found at 4026 Å, 4143 Å, 4387 Å and 4470 Å. There is a possible He 4121 Å absorption line. There also appear to be absorption lines located at 3932 Å (CaII), 4142 Å (HeI) and 4132 Å (SiIII), however the signal-to-noise is very low, and it is difficult to determine whether these features are real. The absence of He II means that the spectral classification is later than B0.

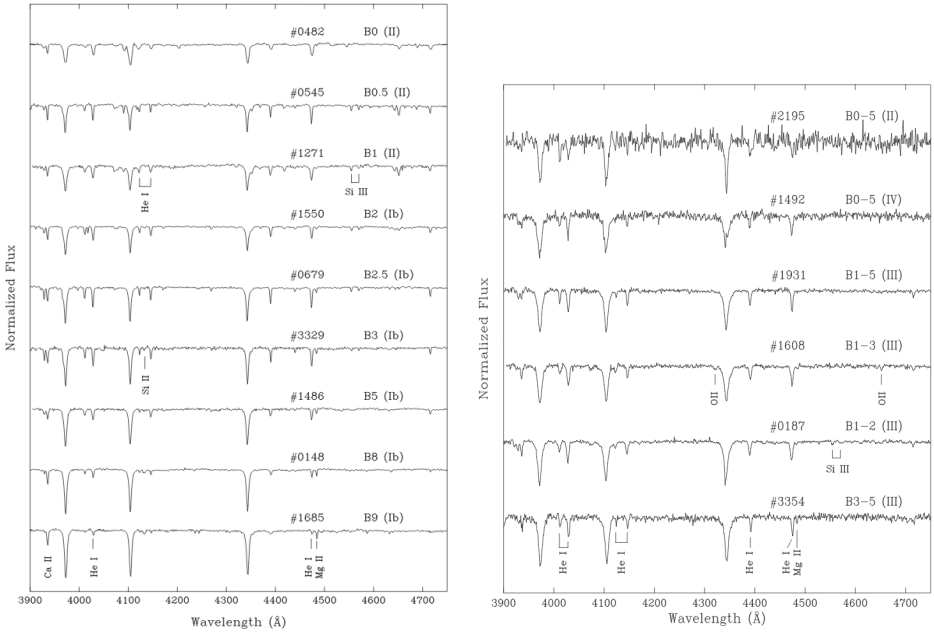

Figure 4.8: B-stellar spectral sequence of luminosity class Ib-II (*left*) and II-IV (*right*) in the 2dFS catalogue (Evans et al., 2004, figure 3).

4.2.2 Magnitude Comparisons

A Be star at the distance of the SMC should share similar apparent magnitudes with other Be stars within the Magellanic Bridge (within error due to spectral type and luminosity class). Since the object is located in the western region of the Bridge (closest to the SMC), the distance modulus to the SMC is used.

The first Be/X-ray Binary system discovered in the Magellanic Bridge was RX J0209.6−7427, with a V magnitude of 14.45 and a spectral classification constrained to B0-1.5 IV-Ve (Kahabka and Hilker, 2005). A few years later, the BeXRB system IGR J015712−7259 was found, with a magnitude of 15.4 in the R1 band (Coe et al., 2008), and magnitudes of 14.48, 14.66 and 14.7, in the I, J and B bands, respectively (DENIS Consortium, 2005). The third known BeXRB system in the Bridge is Swift J0208.4−7428 (McBride

et al., 2010), whose optical companion was initially observed by Irwin et al. (1985) with B and V magnitudes of 14.41 and 14.75, respectively. For object 5437, the available NOMAD Catalog (Zacharias et al., 2005) magnitudes in the B, V and R bands are 14.61, 15.06 and 15.97, respectively. Long term observations of this object have also been performed using OGLE in the I band, and can be found in figure 4.9.

Comparing the available magnitudes of object 5437 to the previously known Be star from Kahabka and Hilker (2005) that exists in the Bridge, the values are within 0.61 magnitude, with object 5437 being dimmer. The spectral type of a star, as well as its distance from Earth, affect the apparent magnitude. The disparity in V magnitudes may be a result of object 5437 being a later spectral type, or is located at a greater distance. It is expected that a Be star of luminosity class Ib-II located in the Bridge would either match or be brighter than a B0-1.5 IV-Ve star (due to error in distance).

The apparent V magnitude of object 5437 may be converted to an absolute V magnitude, M_V, by using the distance modulus of the SMC (Hilditch et al., 2005, $\mu_{SMC} = 18.95 \pm 0.07$). A value of $M_V = -3.89 \pm 0.07$ is obtained. Wegner (2006) provides an analysis of absolute V magnitudes of OBe stars with varying luminosity classes (from a sample of OBe stars in Milky Way). A list of possible spectral types and luminosity classes that object 5437 may be classified as, based on its absolute V magnitude, is shown in Table 4.1. The large variety of possible classifications is a result of the large variance of each spectral type found within Wegner (2006). Thus the magnitude of object 5437 is consistent with OBe magnitudes, assuming the object is located within the Magellanic Bridge.

The OGLE-IV light curve of object 5437 in the Cousins I band can be found in figure 4.9. The first observation shown was obtained in June 2010, with the object at an I magnitude of 15.085 ± 0.003. Approximately four years later, the magnitude of the object falls by a value of 0.25. Over the following four years, it raises in magnitude to a final observed value

Table 4.1: Range of luminosity classes and spectral types that object 5437 fall within error, based on its absolute V magnitude. M_V is calculated using the distance modulus of the SMC (Hilditch et al., 2005, $\mu_{SMC} = 18.95 \pm 0.07$). Magnitudes of OBe stars within the Milky Way obtained from tables 1-6 in Wegner (2006).

Luminosity Class	Spectral Type	Magnitude Range
V	O5 - B2.5	$-7.6 \rightarrow -1.2$
IV	O9 - B2.5	$-5.8 \rightarrow -0.7$
III	O7 - B3	$-9.9 \rightarrow -0.8$
II	O7 - B3	$-7.5 \rightarrow -2.4$
Ib	B0 - B9.5	$-7.4 \rightarrow -2.5$
Iab	O5 - B9.5	$-7.0 \rightarrow -3.2$

of 15.092 ± 0.003 in February 2019. These variations in magnitude are also observed in other BeXRBs that vary within ~ 0.5 magnitude. One example is Swift J053041.9−665426, which varies between 15.0 - 15.3 magnitude (Vasilopoulos et al., 2013). The variation in magnitude is attributed to the changing size of the circumstellar disk due to the gravitational interaction between the Be star and neutron star. After analysing the lightcurve using the Lomb-Scargle method, no significant period less than 300 days was found, which is not consistent with a BeXRB interpretation. Any variability longer than 300 days may be due to the super-orbital period variability.

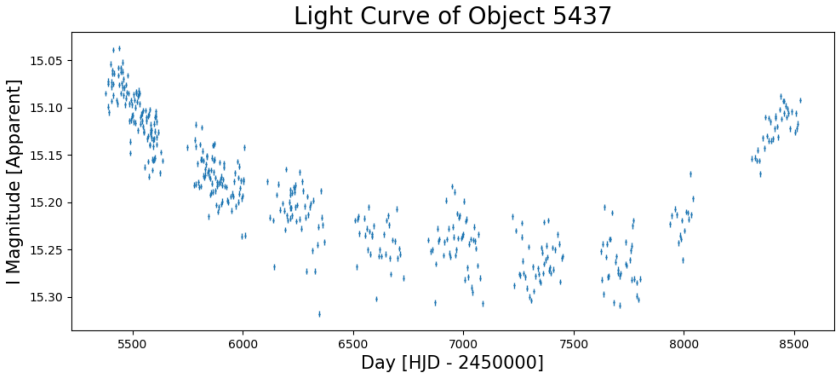

Figure 4.9: *Top*: Light curve obtained from OGLE-IV for object 5437 in the standard Cousins I band.

4.2.3 X-ray Counterpart

If this star is in a BeXRB system, the X-ray counterpart is most likely a neutron star. An X-ray spectrum of the detected source (MB3 PN 21) can be found in figure 4.10. The spectrum has a very low signal-to-noise, thus making it difficult to fit a model. Using an X-ray spectral fitting package, xspec (National Aeronautics and Space Administration, b), a power law model was fit to the spectrum, which returned a photon index of 0.64 ± 0.48. The large error makes it difficult to determine whether this is consistent with a quiescent BeXRB, however it does fall within error. X-ray emission from OB stars is thermal (Zhekov and Palla, 2007), which is not what is observed in this spectrum, further suggesting the X-ray emission is not from the optical object 5437.

An X-ray light curve of source MB3 PN 21 was extracted and is shown in figure 4.11. The sampling period of the dataset is 100 s, thus any periods shorter than 200 s will not be detectable according to the Nyquist theorem. The light curve was analysed for any periods larger than 200 s using a Lomb-Scargle method, however no significant periods were detected, which is not surprising given the low counts.

As mentioned in section 3.2, the same data files for field MB3 were used for the 3XMM-DR6 catalogue (Rosen et al., 2016). The X-ray source MB3 PN 21, which is associated with object 5437 (distance separation of $\sim 2.60''$), is found to match with 3XMM-DR6 J022422.8−735116, a source in the Rosen et al. catalogue (distance separation of $\sim 1.44''$).

A comparison of hardness ratios and fluxes between X-ray source MB3 PN 21 and 3XMM-DR6 J022422.8−735116 was performed, and is confirmed that both sources match according to their hardness ratio and fluxes (within error), and can therefore conclude that both sources are the same. For example, The total flux of MB3 PN 21 is $\log(L_X) \sim -13.24$ erg cm^{-1} s^{-1}, and the total flux of J022422.8−735116 is $\log(L_X) \sim -13.23$ erg cm^{-1} s^{-1}. Both sources have an X-ray luminosity of $\log(L_X) \sim -16$ erg cm^{-1} s^{-1} in the 0.2 - 2.0 keV band, increasing to $\log(L_X) \sim -14.15$ erg cm^{-1} s^{-1} in the 2.0 - 4.5 keV band, with even stronger emission in 4.5 - 12 keV at $\log(L_X) \sim -13.3$ erg cm^{-1} s^{-1}. There is a small disparity in values, however this is most likely the result of differing parameters when reducing the data.

The distance separation between X-ray source 3XMM-DR6 J022422.8−735116 and optical object 5437 is $\sim 1.30''$, a smaller separation than that between X-ray source MB3 PN 21 and object 5437 ($\sim 2.60''$). The sources in the 3XMM-DR6 catalogue have been boresight corrected, thus the smaller separation distance between 3XMM-DR6 J022422.8−735116 and optical object 5437 is further evidence that both objects are the same. The Rosen et al. (2016) catalogue states that 3XMM-DR6 J022422.8−735116 is an AGN, however, the only optical counterpart is a Be star. This is a common misclassification with neutron stars due to their hardness ratios (Natalie Webb, personal communication, September 10, 2019).

Since the X-ray luminosity is consistent with a quiescent BeXRB at the distance of the Magellanic Bridge (quiescent BeXRBs have an energy output of $\log(L_X) = 33.3 \pm 1.2$, Lewin et al., 1997), with a recession velocity that falls within error to that of the SMC, and the star has a magnitude similar

to that of a B III-IV star located at the distance of the Magellanic Bridge, it is proposed that this system is a Be/X-ray binary (BeXRB). If this is the case, it would be the fourth known BeXRB to be found within the Magellanic Bridge region.

The observed flux (in erg cm^{-2} s^{-1} in 0.2-12 keV) may be converted to luminosity (erg s^{-1}) using a given distance, similar to equation (4.3). Assuming that the X-ray source is associated with object 5437 in the Magellanic Bridge, the distance to the SMC is used, which is 60.1 ± 3.8 kpc (Hilditch et al., 2005). The X-ray luminosity in the 0.2-12 keV band may then be calculated (with observed flux $F_{PN\ 21} = (5.81 \pm 0.96) \times 10^{-14}$ erg cm^{-2} s^{-1}):

$$L_{PN\ 21} = F_{PN\ 21} \times 4\pi D^2 \tag{4.6}$$

$$L_{PN\ 21} = (2.51 \pm 0.47) \times 10^{34} \text{ erg s}^{-1} \tag{4.7}$$

$$\log(L_{PN\ 21}) \sim 34.4 \text{ erg s}^{-1} \tag{4.8}$$

This value may then be compared to the X-ray luminosities of OB stars and quiescent BeXRBs. A study of the X-ray luminosity of OB stars was performed by Nazé et al. (2011), which compared the bolometric luminosity (L_{bol}) to the X-ray luminosity (L_X) in the 0.5-10 keV band. It was found that there was a positive correlation between $\log(L_X)$ and $\log(L_{bol})$ for O stars in all bands. However, for B stars, $\log(L_X)$ stays constant for all $\log(L_{bol})$.

There are three X-ray bands defined in Nazé et al. (2011), these are $0.5 - 1.0$ keV, $1.0 - 2.5$ keV and $2.5 - 10$ keV, which are described as soft, medium and hard, respectively. For a given bolometric luminosity of O stars, it was found that the X-ray luminosity decreases from the soft to hard band, usually by an order of magnitude. In the soft band, $\log(L_X)$ varies from 30.5 to 33. In the medium band, $\log(L_X)$ varies from $30 - 33$. In the hard band, $\log(L_X)$ varies from $26 - 33$.

However, for B stars it remains relatively constant across all three bands,

Table 4.2: Flux and luminosities of X-ray source MB3 PN 21, assuming object lies within Magellanic Bridge (at a distance of the SMC, 60.1 ± 3.8 kpc). Conversion from flux to luminosity performed using equation (4.6).

X-ray Band [keV]	Flux [erg cm^{-2} s^{-1}]	Luminosity [erg s^{-1}]
0.2 - 0.5	$(0.71 \pm 1.36) \times 10^{-16}$	$(3.1 \pm 6.0) \times 10^{31}$
0.5 - 1.0	$(4.15 \pm 2.69) \times 10^{-16}$	$(1.8 \pm 1.2) \times 10^{32}$
1.0 - 2.0	$(2.68 \pm 3.24) \times 10^{-16}$	$(1.2 \pm 1.4) \times 10^{32}$
2.0 - 4.5	$(6.78 \pm 1.77) \times 10^{-15}$	$(2.9 \pm 0.8) \times 10^{33}$
4.5 - 12.0	$(5.07 \pm 0.95) \times 10^{-14}$	$(2.2 \pm 0.5) \times 10^{34}$
0.2 - 12.0	$(5.81 \pm 0.96) \times 10^{-14}$	$(2.5 \pm 0.5) \times 10^{34}$

$\log(L_X)$ can vary from 28 to 31.5 for a given L_{bol}. If the X-ray emission of source MB3 PN 21 is from object 5437, it is expected that it share the X-ray luminosity properties of B stars in Nazé et al. (2011). Although the X-ray luminosity is similar to that of the observed O stars ($\log(L_X) \sim 30 - 33$ as seen in equation (4.7), the luminosity in each band increases, found in Table 4.2. Although the X-ray bands are slightly different than those defined in Nazé et al. (2011), a general trend of increasing luminosity is observed, by three orders of magnitude from $0.5 - 1.0$ keV to $4.5 - 12$ keV, suggesting the X-ray luminosity is emitted by another object.

Regardless of whether the distance of the object is correctly assumed, if the flux is solely due to the emission of the optical object 5437, the flux should either be constant (within an order of magnitude) across all bands (which is observed in B stars) or decrease in the higher energy bands (observed in O stars).

Since the system shares similar properties to other Be/X-ray binaries, the X-ray companion will be compared to quiescent neutron stars (where low level accretion may occur, causing the energy output to be higher than isolated neutron stars where no accretion occurs). Quiescent neutron stars

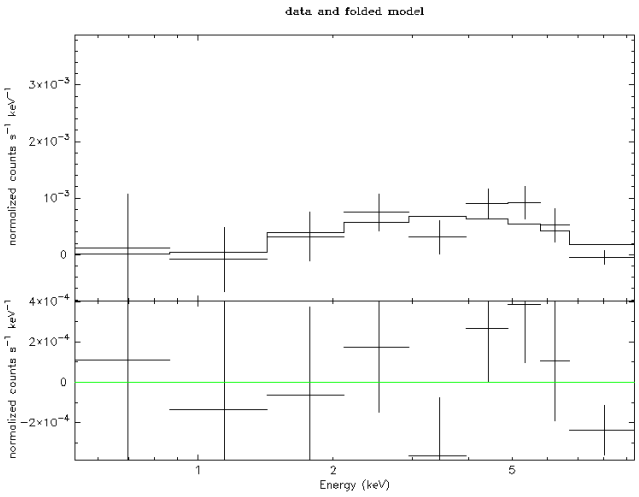

Figure 4.10: X-ray spectrum of source PN 21 in field MB3 between 0.2 and 10 keV. The solid line is a fitted power law with a photon index of 0.64 ± 0.48 and a reduced χ^2 value of 0.14 with 3 degrees of freedom. The residuals are found in the lower panel.

in BeXRBs have X-ray luminosities of $\log(L_X) \sim 33.3 \pm 1.2$ (Lewin et al., 1997, Table 2.1). In addition, according to Table 3 of Sturm et al. (2013), the X-ray source falls within the classification of a HMXB (falls within the category of ultrahard).

4.3 Final Remarks

All objects observed along with their respective classifications are shown in Table 4.3. The following subsections discuss the nature of the observed objects in relation to the introductory section 1.6.

4.3.1 K Stars and M Dwarfs

Of all objects observed, a majority contain absorption dominant spectra, these are objects 5547, 5794 and 5355. In late spectral-type stars (M dwarfs),

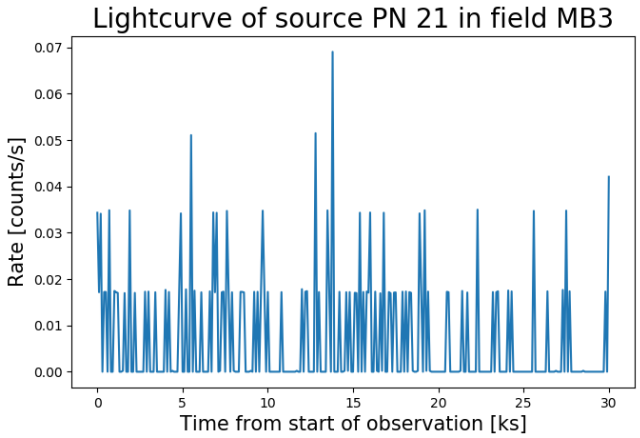

Figure 4.11: X-ray light curve of source PN 21 in field MB3 between 0.2 and 12 keV. The sampling period of the dataset is 100 s, due to the low signal of the source.

Table 4.3: List of all followed up objects with their spectral classification. †The classification of object 3296 was difficult to discern, with K4e being the closest match in the Pickles (1998) database.

Object	Classification
5547	dM2-4 Ve
5794	dM1-3 V
5355	dM1-3 Ve
3296	K4e†
9967	Seyfert 1
5437	B0-5 II-IVe

the spectrum is dominated by molecular absorption bands, primarily from titanium monoxide (TiO, Morgan et al., 1943). The lower surface temperature allows the TiO molecule to form. In addition, there exist discrete ionized Ca II lines (Walker, 2018), known as the Fraunhofer H and K lines. In earlier spectral types, a Ca I absorption line can be found.

As for object 3296, the presence of the Hα emission makes it difficult to classify, and may be another type of object. K stars are known to exist in cataclysmic variables, however almost all lines are seen in emission, and are much stronger than the Hα emission observed in object 3296 (Thorstensen et al., 2004). Thus, although the spectrum of object 3296 closely fits that of a K4 star, the Hα emission makes it difficult to determine the accuracy of the classification.

All objects that have been classified as M dwarfs in Table 4.3 are classified as soft sources according to their X-ray hardness ratios (objects 5355, 5547 and 5794) within 1σ error. For the K-type star (object 3296), the error on the HR values is larger, and can be potentially classified as soft, hard or ultrahard.

4.3.2 Seyfert Galaxies

Seyfert 1 galaxies are a class of active galactic nuclei (AGN, as discussed in section 1.6.2). The differentiation between Seyfert 1 and Seyfert 2 galaxies is dependent on the presence or absence of broad emission lines in the optical spectrum (Singh et al., 2011), due to the viewing angles of these AGN cause the distinction between the two classes. In the case of Seyfert 1, the central supermassive black hole is directly observed; whereas, for Seyfert 2 the super massive black hole is obstructed by a thick, dusty torus. In the spectra, broad lines are observed in Seyfert 1 galaxies, whereas narrow lines are observed in Seyfert 2 galaxies.

Object 9967 exhibits properties of a Seyfert 1 galaxy, with a broad Hβ emission line. The spectrum is also redshifted by $z = 0.244 \pm 0.002$, which

gives a luminosity distance of $D_L = 1.263 \pm 0.014\,\mathrm{Gpc}$. The observed flux in the MOS1 and PN cameras was converted to luminosities using the distance D_L, and returned values of $(2.8 \pm 0.1) \times 10^{42}$ erg s^{-1} and $(2.5 \pm 0.1) \times 10^{42}$ erg s^{-1}, respectively.

The hardness ratios of AGNs are typically categorised as hard. The X-ray source of object 9967 in the MOS1 is categorised as hard, where as can be categorised as either soft or hard in the PN camera (within 1σ error).

4.3.3 BeXRBs in the Magellanic Bridge

Three fields were observed, which covers an area of approximately 0.6 square degrees (given that the radius is $15'$). Only one BeXRB system was observed in this area, which equates to approximately 1.66 BeXRB systems per square degree.

This is a higher density than estimated by Kahabka and Hilker (2005, 0.68 - 0.98 BeXRBs per square degree), however, due to the small area observed, the single system statistically skews the density to much higher than what may possibly exist. Further surveys if the Bridge should be performed in order to obtain a more accurate BeXRB density of the region.

Chapter 5

Conclusion

Three fields were imaged using the XMM-Newton for 30 ks each, using the same fields as Harris (2007). X-ray point sources were matched within a 3″ radius with optical sources in Harris (2007, photometric catalgue) and Rosen et al. (2016).

Matched optical sources with magnitudes brighter than $\sim$ 18 were followed up using the 1.9 m telescope located in Sutherland, South Africa, using the SpUpNIC instrument.

Six objects matched the above criteria, and were observed in a broad filter (4000 Å to 7000 Å). One object of interest (named object 5437) was then observed using a higher resolution grating in a smaller wavelength range (3900 Å to 4750 Å).

Three objects appear to be M dwarfs that are located in the Milky Way (objects 5355, 5547 and 5794). Object 3296 is most likely a K4 star, when compared to the Pickles (1998) spectra. Object 9967 is a highly redshifted Seyfert 1 galaxy.

5.1 Object 5437

Object 5437 is a Be star located in a lower metallicity environment. A higher resolution spectrum was obtained and compared to lower metallicity OB stars found within the SMC (Evans et al., 2004). The object was constrained to B0-5 II-IVe.

A radial velocity of 186 ± 60 km s^{-1} was obtained from the spectrum, which falls within the radial velocity of the SMC (145.6 ± 0.6 km s^{-1}). The B, V and R magnitudes obtained from the NOMAD catalogue are consistent with OB stars located within the SMC (Wegner, 2006).

The X-ray source MB3 PN 21 is the X-ray counterpart to optical object 5437. An X-ray spectrum was extracted, a power law model was used to fit the data with a photon index of 0.64 ± 0.48. However, X-ray emission from OB stars is thermal (Zhekov and Palla, 2007) and does not increase in energy in the harder bands (Nazé et al., 2011). Thus another source in the region of object 5437 that has little to no optical emission is responsible for the X-ray emission. Additionally, an X-ray lightcurve was extracted from source MB3 PN 21, however the count rate was too low to extract any periodicity.

A suitable model for this is a Be/X-ray binary (BeXRB) system, with a neutron star companion. There has been no X-ray outburst, thus the BeXRB is in quiescence. The X-ray flux of source MB3 PN 21 was converted to X-ray luminosity (using the distance of the SMC, a value of $\log(L_X) \sim 34.4$ erg s^{-1} was obtained), and is consistent with quiescent BeXRBs, which typically have emissions of $\log(L_X) = 33.3 \pm 1.2$ erg s^{-1} (Lewin et al., 1997).

The B and B - V colours, along with the X-ray source classified as ultra-hard, satisfy the conditions for a BeXRB found within Table 3 of Sturm et al. (2013). Source MB3 PN 21 also matches with X-ray source J022422.8−735116 from the 3XMM-DR6 catalogue (Rosen et al., 2016). Both sources were obtained from the same unprocessed data set (slight difference in fluxes due to differing reduction parameters). Rosen et al. (2016) classifies the source as an AGN, this is purely based on X-ray emission alone. The evidence in this

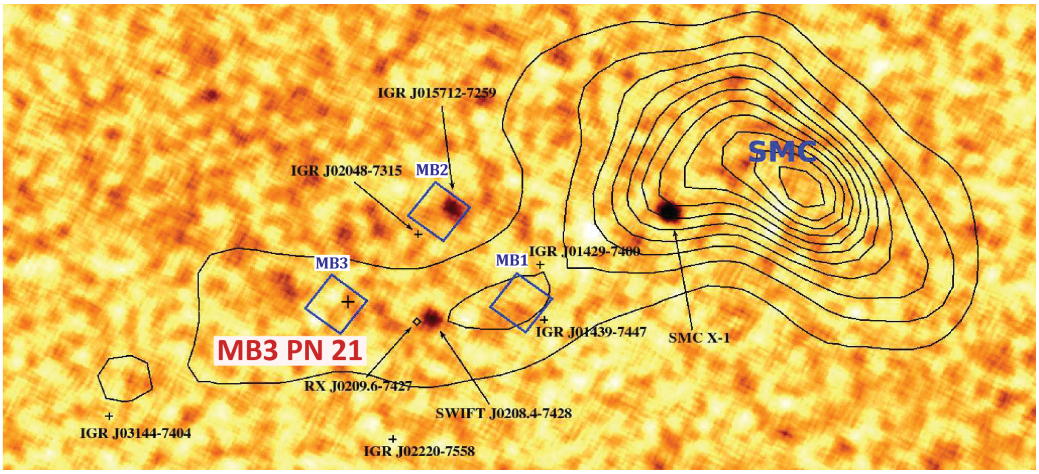

Figure 5.1: Same as figure 2.1, with the addition of Be/X-ray candidate source MB3 PN 21.

dissertation suggests that this is a misclassification of a neutron star (Natalie Webb, personal communication, September 10, 2019), and that this system is a BeXRB located in the Magellanic Bridge.

Further Investigation

Due to the interesting nature of object 5437, a higher resolution spectrum should be obtained in order to better constrain the spectral class of the object. In addition, the system should be placed on a Be/X-ray monitoring program to observe if there is either an evolution in the Hα line, or possibly an outburst due to accretion.

If the system is a BeXRB, it will be the fourth known BeXRB within the Magellanic Bridge, and will be the furthest BeXRB from the SMC. It would also increase the BeXRB density of the Bridge. This is further evidence of a rich star forming region located between two interacting galaxies. The close proximity allows for an in-depth study of how the region between interacting galaxies behaves due to the resolvability of sources.

Appendices

Appendix A

Data Manipulation In Python

Python is able to read in FITS files into arrays. From here, various data can be plotted against one another. As mentioned in the previous section 2.4, the region file created from the `srcdisplay` which is then read into ds9[1] (which contains the source locations) does not contain the source ID. The `regionfile` also obtains seven rows of R.A. and Dec. for each source (a consequence of the emllist containing seven rows of information for each source, as discussed in section 2.4.1). The goal is to then create a region file that can be read into ds9, and contains the source ID.

To remedy the various issues with the `regionfile` produced by the `srcdisplay` command, this file may be read into Python and edited in order to obtain a `regionfile` that contains source IDs and no duplicate coordinates. This is done by reading each line of the file into an array entry as a string. A new empty array is created which will store only one of each coordinate. If an array entry is the same as the following entry (which would be the exact same location), it is not written to the new array. This allows for an array to be created that does not contain any duplicates.

As for the source ID, this is simply appended to each entry of the array. The order in which the coordinates are written are also the order of the

[1] `https://sites.google.com/cfa.harvard.edu/saoimageds9`

source IDs, and ranges from 1 to n (the total amount of sources). Once the new array is created (which contains the correct coordinates, and is correctly labelled with source IDs), it can then be written to a new text file. This text file can then be read into ds9, overlaying an X-ray image with the correct source locations and labels. A corrected version of the `regionfile` in use can be seen in figure 2.6.

Another useful function implemented in Python is to categorise sources based on their hardness-ratios. This can be done by creating a user defined class. The class allows an object to be created that contains multiple attributes. This object may then be created for each `emllist`, which will contain information such as the camera that was used and the R.A., Dec., ID, HR, etc, of each source in said file. Section B will cover how the hardness-ratios can be used in order to pre-emptively categorise sources.

Once the data has been read into Python (using the `astropy` extension to read in FITS files), specific columns can be read into arrays. The simplest way to do this is by creating an object for each emllist. This object will contain various properties, such as source IDs, their location, hardness-ratios, etc. This is a better alternative to creating new arrays for each property, and rather append these properties to a single object. Doing this allows for creating function with a single input being that of the object, rather than several inputs for each array one is interested in. Properties may also be appended to the object later.

When reading the emllist into Python, the issue of each source containing seven rows of data still persists. The solution is to simply remove any repeating rows such that each source only has one row of data associated with it. However, for the hardness-ratios, they are located in the second row for each source (section 2.4.1), thus all other rows are discarded. Once each array has been corrected for (due to duplication), a new region file may be created. In addition to this, each source may then be labelled according to the source ID. The corrected region file overlaid with an image may be found

in figure 2.6.

Appendix B

Categorising Sources Based On Hardness Ratios

For this section, Python was implemented in extracting source information from FITS files, as well as categorising sources and plotting the values. For a more in-depth explanation, refer to appendix A. Hardness ratio classification follows the groupings observed in astronomical objects as seen in Sturm et al. (2013).

Sources are not easily classified just by looking at the X-ray flux, here the hardness-ratios become important in distinguishing between different source types (e.g. galaxies or compact objects). The criteria laid out by Sturm et al. (2013) can be found in Table B.1; in addition, figure B.1 shows where different objects appear to cluster. There were additional requirements for super soft sources, which involve comparing the flux of an object in different bands. These requirements were omitted in order to simplify classification.

These requirements may be graphed. This allows for a quick glance at where sources lie in the HR parameter space. Sources found in figure 2.6 are plotted in HR parameter space (HR_1 - HR_2 plane) in figure B.2. This parameter space categorises sources into either super soft (left of red line) or not super soft (right of red line).

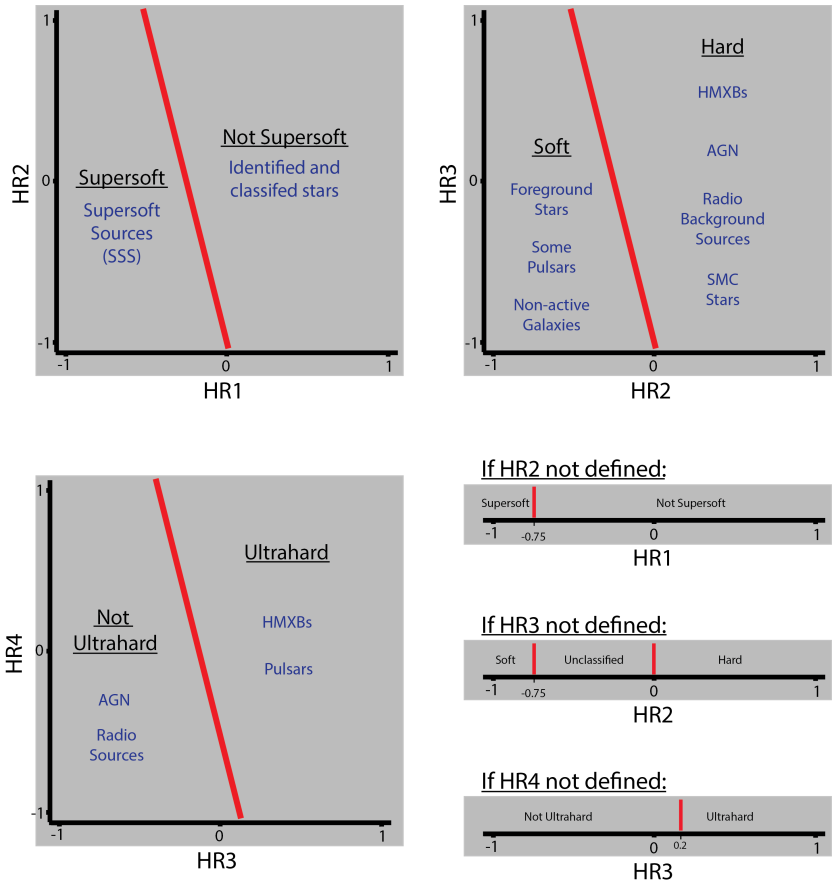

Figure B.1: Hardness Ratio (HR) classifications based on Table 2.2, with objects found to cluster based on these hardness ratios (based on clusterings found in figure 8 of Sturm et al., 2013). The bottom right graphs show classifications if HR2, HR3 or HR4 are undefined.

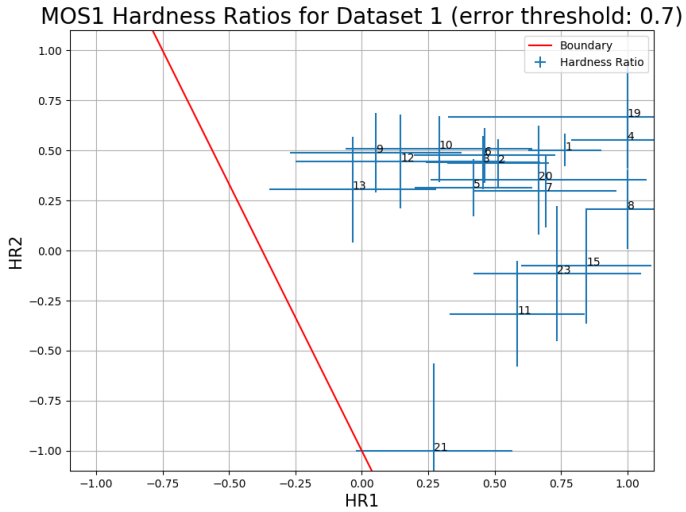

Figure B.2: Hardness-ratios (HR_1 - HR_2 plane) of sources found in the MOS1 camera in field MB1. These sources correspond to sources found in figure 2.6. This plot categorises sources into either super soft (left of red line) or not super soft (right of red line).

When categorising multiple sources, a function within Python may be used to read in the HR values of a source and determine where in the HR plane the source lies. This is important for sources that cannot be graphed (sources where the HR value in a given band is not defined, and thus cannot be plotted on a 2D plane). The function within Python may label a source using the 1D planes shown in figure B.1. The 1σ error value adds complexity, since a source may be defined as soft or hard within its error value.

When categorising a source according to its 1σ error, the best approach to sorting is to treat the lower bound ($HR_n - \sigma(HR_n)$) and upper bound ($HR_n + \sigma(HR_n)$) of the HR as a single point, and sort these according to Table B.1 independently, resulting in a list of sources that may exist in more than one category (such as super soft, soft, etc.). In a two dimensional plot, the lower and upper bounds would be as follows:

- Lower Bound:

$(\mathrm{HR_n} - \sigma(\mathrm{HR_n}), \mathrm{HR_{n+1}} - \sigma(\mathrm{HR_{n+1}}))$

- Upper Bound:
  $(\mathrm{HR_n} + \sigma(\mathrm{HR_n}), \mathrm{HR_{n+1}} + \sigma(\mathrm{HR_{n+1}}))$

An example of this is by looking at source MB3 PN 21 in figure B.2, the lower bound (bottom left) exists within the super soft region, where as the upper bound (top right) does not. Since it is quicker to numerically classify sources, a sorting algorithm must be created in Python. The method is to treat the lower and upper bounds as independent points (across all HRs), then create new arrays for each category which contain the source IDs. Since there are four categories of X-ray hardness (supersoft, soft, hard and ultrahard), and the possibility of not being classified (not meeting the requirements in figure B.1), five arrays are then created for each camera and each dataset. Since the sorting algorithm depends on the hardness-ratios (and the error in this value), it is easier to first store these values into a class in Python. When a source falls within multiple classifications, it retains all classifications that it satisfies, e.g. a source may be classified as soft, hard and ultrahard due to the associated error. It is only after further investigation of a source that the classification may be constrained further. Sources with high error tend to fall within multiple categories.

The `emllist` (section 2.4.1) is read into Python using the `astropy` package. As mentioned in appendix A, this information is stored into a class object. The class function will read in the `emllist` and will store information as strings (camera name, source IDs, etc.) and arrays (source location, hardness-ratios, etc.). This class may then be passed through the sorting algorithm, and new arrays are then appended to the class. These new arrays are the hardness-ratio categories (table B.1) which now contain the categorised source IDs. Due to the error on the hardness-ratio, a source may exist in two separate arrays (categories).

Once the sources have been sorted, new FITS files may be created for each hardness ratio category and for each camera. These files which contain

Table B.1: Source classification based on the Hardness Ratios of various sources defined in Sturm et al. (2013).

Spectrum	Selection criteria
Super Soft (ss)	$8HR_1 + 3HR_2 < -3$ or ($HR_1 < -0.75$ & HR_2 not def.)
Soft (s)	$8HR_2 + 3HR_3 < -3$ or ($HR_2 < -0.75$ & HR_3 not def.)
Hard (h)	($8HR_2 + 3HR_3 > -3$ or ($HR_2 > 0$ & HR_3 not def.)) & not ss
Ultra Hard (uh)	($8HR_3 + 3HR_4 > -1.4$ or ($HR_3 < 0.2$ & HR_2 not def.)) & not ss & not s
Unclassified	Not contained in any of the above expressions

the classified sources may then be read into other programs, such as Aladin: Sky Atlas[1], and may be cross-matched with other optical surveys, namely Harris (2007).

[1] `aladin.u-strasbg.fr/`

Appendix C

X-ray Source Lists

C.1 Field MB1

Table C.1: X-ray point source list of all detections in the MOS1 camera in dataset MB1, corresponding image and HR plots are found in figure 2.6.

MOS1 Sources in Dataset MB1													
Source ID	R.A. [J2000]	Dec. [J2000]	σ(pos) [″]	Flux [erg cm^{-2} s^{-1}]	σ(Flux) [erg cm^{-2} s^{-1}]	HR_1	$\sigma(HR_1)$	HR_2	$\sigma(HR_2)$	HR_3	$\sigma(HR_3)$	HR_4	$\sigma(HR_4)$
1	01 49 05.3	-74 29 51	0.56	1.08×10^{-13}	1.67×10^{-14}	0.765	0.138	0.502	0.082	-0.253	0.127	-0.537	0.127
2	01 48 38.2	-74 25 22	0.95	3.70×10^{-14}	1.05×10^{-14}	0.515	0.192	0.439	0.12	-0.36	0.239	-0.828	0.239
3	01 47 49.2	-74 33 25	0.93	3.44×10^{-14}	8.46×10^{-15}	0.458	0.217	0.44	0.135	-0.32	0.209	-0.659	0.209
4	01 48 20.3	-74 20 07	1.2	9.23×10^{-14}	3.16×10^{-14}	1	0.211	0.553	0.14	-0.107	0.258	-0.483	0.258
5	01 45 47.1	-74 25 33	0.91	5.50×10^{-14}	2.29×10^{-14}	0.421	0.223	0.315	0.144	-0.382	0.393	-0.45	0.393
6	01 46 47.6	-74 40 17	1.28	3.48×10^{-14}	1.82×10^{-14}	0.463	0.266	0.476	0.139	-0.793	0.767	-0.222	0.767
7	01 48 12.0	-74 33 45	1.36	3.05×10^{-14}	1.10×10^{-14}	0.692	0.269	0.297	0.18	-0.29	0.323	-0.372	0.323
8	01 47 35.1	-74 29 36	1.26	1.33×10^{-14}	3.65×10^{-15}	1	0.158	0.206	0.199	-0.128	0.148	-1	0.148
9	01 51 17.6	-74 29 53	1.32	2.26×10^{-13}	7.20×10^{-14}	0.053	0.324	0.489	0.199	-0.283	0.217	0.447	0.217
10	01 50 58.7	-74 25 14	1.57	5.34×10^{-14}	2.47×10^{-14}	0.292	0.352	0.508	0.167	-0.176	0.331	-0.858	0.331
11	01 46 21.1	-74 42 12	1.82	6.04×10^{-14}	3.55×10^{-14}	0.586	0.256	-0.316	0.264	-1	0.428	1	0.428
12	01 50 46.8	-74 25 28	1.8	2.29×10^{-14}	2.01×10^{-14}	0.146	0.396	0.446	0.234	-0.328	0.755	-1	0.755
13	01 50 18.4	-74 30 15	2.4	3.30×10^{-14}	2.27×10^{-14}	-0.035	0.315	0.305	0.264	-0.589	0.656	0.16	0.656
14	01 49 09.7	-74 28 11	1.42	3.74×10^{-14}	1.44×10^{-14}	1	1.126	0.649	0.262	0.036	0.304	-0.148	0.304
15	01 48 49.8	-74 29 05	1.58	1.27×10^{-14}	6.47×10^{-15}	0.847	0.246	-0.077	0.288	-0.051	0.406	-0.702	0.406
16	01 45 35.9	-74 30 20	1.82	4.82×10^{-14}	2.50×10^{-14}	1	0.831	0.759	0.191	-0.478	0.395	0.305	0.395
17	01 46 30.4	-74 27 50	2.06	2.74×10^{-14}	1.66×10^{-14}	0.187	0.894	0.824	0.187	-0.274	0.474	-0.177	0.474
18	01 48 03.5	-74 30 42	1.66	2.64×10^{-14}	8.29×10^{-15}	1	3.952	0.106	0.986	0.855	0.217	-0.431	0.217
19	01 46 29.5	-74 39 48	2.11	4.81×10^{-14}	2.96×10^{-14}	1	0.675	0.667	0.257	-0.146	0.467	-0.21	0.467
20	01 45 29.7	-74 37 48	2.09	1.52×10^{-14}	1.40×10^{-14}	0.666	0.407	0.353	0.274	-0.415	0.867	-0.707	0.867
21	01 45 38.6	-74 27 28	2.43	1.78×10^{-14}	1.84×10^{-14}	0.273	0.295	-1	0.437	1	0.937	0.668	0.937
22	01 49 11.6	-74 22 32	1.94	1.63×10^{-14}	1.42×10^{-14}	1	2.511	0.892	0.251	-0.596	0.825	-0.446	0.825
23	01 48 28.7	-74 29 47	1.98	5.54×10^{-15}	3.84×10^{-15}	0.736	0.316	-0.116	0.339	-0.113	0.531	-1	0.531
24	01 45 22.2	-74 31 24	2.13	5.68×10^{-14}	2.55×10^{-14}	-	-	-	-	1	0.318	-0.033	0.318

Table C.2: X-ray point source list of all detections in the MOS2 camera in dataset MB1, corresponding image and HR plots are found in figure 2.7.

MOS2 Sources in Dataset MB1													
Source ID	R.A. [J2000]	Dec. [J2000]	σ(pos) [″]	Flux [erg cm^{-2} s^{-1}]	σ(Flux) [erg cm^{-2} s^{-1}]	HR_1	$\sigma(HR_1)$	HR_2	$\sigma(HR_2)$	HR_3	$\sigma(HR_3)$	HR_4	$\sigma(HR_4)$
1	01 49 05.4	-74 29 51	0.55	1.07×10^{-13}	1.34×10^{-14}	0.614	0.144	0.51	0.08	-0.151	0.096	-0.729	0.096
2	01 47 49.3	-74 33 25	0.76	3.77×10^{-14}	7.66×10^{-15}	0.755	0.169	0.282	0.127	-0.197	0.162	-0.858	0.162
3	01 48 37.9	-74 25 21	0.97	4.31×10^{-14}	1.36×10^{-14}	0.66	0.187	0.364	0.129	-0.434	0.336	-0.502	0.336
4	01 45 47.4	-74 25 31	0.9	5.50×10^{-14}	1.62×10^{-14}	0.344	0.214	0.297	0.14	-0.415	0.342	-0.802	0.342
5	01 48 20.9	-74 20 06	1.09	8.72×10^{-14}	2.90×10^{-14}	1	0.275	0.452	0.153	-0.256	0.291	-0.25	0.291
6	01 46 47.5	-74 40 18	1.03	6.15×10^{-14}	2.35×10^{-14}	0.594	0.177	0.204	0.149	-0.424	0.422	-0.42	0.422
7	01 50 58.9	-74 25 15	1.17	1.07×10^{-13}	4.67×10^{-14}	0.824	0.181	0.247	0.175	-0.447	0.396	0.027	0.396
8	01 48 35.8	-74 40 39	1.37	7.77×10^{-14}	2.73×10^{-14}	0.528	0.325	0.152	0.267	0.079	0.285	-0.004	0.285
9	01 50 18.5	-74 30 12	1.33	2.31×10^{-14}	1.17×10^{-14}	0.714	0.242	0.081	0.208	-0.387	0.604	-1	0.604
10	01 51 17.4	-74 29 52	1.51	6.24×10^{-14}	3.55×10^{-14}	1	0.309	0.307	0.231	-0.08	0.466	-0.471	0.466
11	01 47 39.9	-74 40 18	1.61	1.57×10^{-14}	6.90×10^{-15}	0.607	0.356	0.529	0.178	-0.644	0.616	-1	0.616
12	01 47 35.2	-74 29 36	1.3	1.33×10^{-14}	4.55×10^{-15}	-0.38	0.387	0.736	0.192	-0.527	0.391	-0.724	0.391
13	01 49 09.5	-74 28 11	1.35	3.15×10^{-14}	1.01×10^{-14}	-	-	1	0.079	0.059	0.228	-0.569	0.228
14	01 48 49.4	-74 29 04	1.47	1.41×10^{-14}	5.91×10^{-15}	0.087	1.036	0.848	0.213	0.006	0.25	-0.896	0.25
15	01 47 13.3	-74 22 31	6.06	2.01×10^{-13}	1.61×10^{-13}	0.447	0.146	-0.507	0.179	-0.428	0.991	0.127	0.991
16	01 47 54.3	-74 43 56	1.55	2.27×10^{-14}	2.01×10^{-14}	-1	3.026	1	0.158	0.277	0.45	-1	0.45
17	01 47 16.4	-74 23 49	5.24	7.57×10^{-14}	4.14×10^{-14}	0.131	0.158	-0.691	0.235	0.171	1.159	-0.939	1.159
18	01 48 08.8	-74 42 45	1.61	2.45×10^{-14}	1.71×10^{-14}	1	0.944	0.866	0.17	-0.557	0.699	-0.561	0.699
19	01 46 41.2	-74 17 58	7.01	3.14×10^{-12}	1.42×10^{-12}	0.251	0.14	-0.53	0.184	-0.463	0.293	0.71	0.293
20	01 48 07.0	-74 35 24	1.67	8.13×10^{-15}	6.48×10^{-15}	0.238	0.489	0.501	0.272	-0.325	0.759	-1	0.759
21	01 48 10.6	-74 38 07	1.87	1.59×10^{-14}	1.01×10^{-14}	0.644	1.034	0.624	0.318	0.189	0.421	-0.726	0.421
22	01 50 47.6	-74 25 33	1.43	7.79×10^{-14}	3.55×10^{-14}	0.421	0.384	0.34	0.269	-0.605	0.355	0.533	0.355
23	01 49 25.2	-74 30 37	2.12	8.00×10^{-15}	4.29×10^{-15}	1	0.851	0.794	0.243	-0.321	0.368	-0.961	0.368
24	01 47 25.4	-74 23 00	2.24	4.14×10^{-14}	2.26×10^{-14}	-	-	1	0.259	0.284	0.397	-0.291	0.397
25	01 49 04.0	-74 31 10	1.78	1.51×10^{-14}	7.52×10^{-15}	-	-	1	0.129	0.023	0.333	-0.671	0.333
26	01 48 02.4	-74 40 53	1.97	3.07×10^{-14}	2.10×10^{-14}	-0.832	0.366	0.92	0.18	-0.557	0.588	0.257	0.588
27	01 48 14.3	-74 32 58	1.79	2.42×10^{-14}	9.51×10^{-15}	1	1.073	0.834	0.221	-0.397	0.385	0.208	0.385
28	01 48 21.4	-74 43 17	2.04	5.12×10^{-14}	2.78×10^{-14}	0.464	0.392	0.273	0.276	-0.314	0.479	0.016	0.479
29	01 48 04.0	-74 30 44	2.33	2.68×10^{-14}	9.50×10^{-15}	-	-	1	0.311	0.394	0.295	0.071	0.295
30	01 46 30.3	-74 27 48	2.04	3.32×10^{-14}	1.76×10^{-14}	-	-	1	0.264	0.374	0.385	-0.175	0.385
31	01 46 18.4	-74 30 05	2.02	1.60×10^{-14}	1.02×10^{-14}	0.139	0.477	-0.196	0.535	0.539	0.419	-0.884	0.419
32	01 48 54.9	-74 42 32	3.07	1.96×10^{-14}	9.60×10^{-15}	0.38	0.526	0.186	0.398	0.337	0.247	-1	0.247

Table C.3: X-ray point source list of all detections in the pn camera in dataset MB1, corresponding image and HR plots are found in figure 2.8. Table continued C.4.

pn Sources in Dataset MB1													
Source ID	R.A. [J2000]	Dec. [J2000]	σ(pos) [″]	Flux [erg cm^{-2} s^{-1}]	σ(Flux) [erg cm^{-2} s^{-1}]	HR_1	$\sigma(HR_1)$	HR_2	$\sigma(HR_2)$	HR_3	$\sigma(HR_3)$	HR_4	$\sigma(HR_4)$
1	01 49 05.4	-74 29 51	0.39	1.21×10^{-13}	1.11×10^{-14}	0.703	0.064	0.172	0.057	-0.205	0.09	-0.262	0.09
2	01 47 49.2	-74 33 25	0.68	3.72×10^{-14}	5.41×10^{-15}	0.666	0.12	0.179	0.091	-0.239	0.146	-0.425	0.146
3	01 48 38.1	-74 25 22	0.71	5.38×10^{-14}	1.02×10^{-14}	0.617	0.097	-0.063	0.093	-0.355	0.186	0.032	0.186
4	01 48 21.1	-74 20 07	0.81	7.49×10^{-14}	1.72×10^{-14}	0.907	0.112	0.481	0.085	-0.369	0.226	-0.341	0.226
5	01 46 47.7	-74 40 17	0.73	5.88×10^{-14}	1.39×10^{-14}	0.661	0.097	-0.137	0.104	-0.088	0.23	-0.35	0.23
6	01 48 11.2	-74 33 44	0.92	1.16×10^{-14}	3.47×10^{-15}	0.558	0.14	-0.064	0.12	-0.296	0.355	-1	0.355
7	01 50 18.4	-74 30 13	1	2.85×10^{-14}	1.11×10^{-14}	0.32	0.172	0.3	0.123	-0.42	0.438	-0.471	0.438
8	01 47 40.2	-74 40 17	1.07	2.82×10^{-14}	1.14×10^{-14}	0.748	0.127	-0.007	0.129	-0.399	0.43	-0.232	0.43
9	01 47 35.0	-74 29 39	1.05	1.80×10^{-14}	4.72×10^{-15}	0.723	0.146	0.04	0.135	-0.522	0.336	-0.341	0.336
10	01 48 36.2	-74 40 39	1.07	4.48×10^{-14}	1.44×10^{-14}	0.497	0.198	0.318	0.142	-0.283	0.291	-0.092	0.291
11	01 45 47.6	-74 25 29	1.3	2.13×10^{-14}	1.23×10^{-14}	0.434	0.173	0.053	0.152	-0.633	1.233	-1	1.233
12	01 51 17.2	-74 29 52	1.45	5.35×10^{-14}	2.49×10^{-14}	0.934	0.112	-0.138	0.15	0.036	0.415	-0.343	0.415
13	01 48 18.1	-74 35 25	1.17	2.23×10^{-14}	7.15×10^{-15}	0.642	0.157	-0.155	0.16	-0.451	0.275	0.375	0.275
14	01 49 09.7	-74 28 10	1.2	2.11×10^{-14}	6.99×10^{-15}	0.358	0.383	0.527	0.191	0.01	0.282	-0.529	0.282
15	01 45 39.4	-74 27 27	1.39	5.26×10^{-15}	6.12×10^{-15}	0.358	0.151	-0.923	0.115	-0.006	6.729	-1	6.729
16	01 49 12.5	-74 22 38	1.43	7.27×10^{-14}	1.78×10^{-14}	0.549	0.313	-0.367	0.297	0.623	0.18	0.181	0.18
17	01 50 58.3	-74 25 09	1.48	4.14×10^{-14}	2.38×10^{-14}	1	0.177	0.446	0.158	-0.231	0.546	-0.933	0.546
18	01 45 27.2	-74 20 02	1.24	5.71×10^{-14}	3.13×10^{-14}	0.74	0.173	0.16	0.155	-0.241	0.486	-0.149	0.486
19	01 50 14.4	-74 19 28	1.52	8.82×10^{-14}	4.63×10^{-14}	0.628	0.187	0.154	0.156	-0.572	0.292	0.557	0.292
20	01 49 56.0	-74 35 58	1.51	2.49×10^{-14}	1.21×10^{-14}	0.43	0.234	-0.029	0.209	-0.141	0.43	-0.064	0.43
21	01 46 29.6	-74 39 51	1.5	2.58×10^{-14}	1.44×10^{-14}	0.811	0.345	0.407	0.178	-0.242	0.507	-0.281	0.507
22	01 48 07.1	-74 35 22	1.65	4.78×10^{-15}	3.44×10^{-15}	0.062	0.346	0.392	0.23	-0.556	1.006	-0.669	1.006
23	01 49 03.8	-74 31 11	1.83	1.76×10^{-14}	6.22×10^{-15}	1	0.336	0.433	0.423	0.421	0.28	-0.354	0.28
24	01 48 03.6	-74 30 46	1.88	1.85×10^{-14}	4.61×10^{-15}	-	-	1	0.514	0.729	0.201	-0.236	0.201
25	01 44 54.2	-74 24 30	1.98	6.91×10^{-14}	2.50×10^{-14}	1	0.499	0.442	0.222	-0.182	0.25	0.406	0.25
26	01 51 41.9	-74 27 18	2.22	4.72×10^{-14}	3.77×10^{-14}	0.575	0.193	-0.118	0.173	-0.433	0.643	0.212	0.643
27	01 48 13.6	-74 21 01	2.5	3.61×10^{-14}	1.41×10^{-14}	1	0.404	0.521	0.273	0.116	0.308	-0.033	0.308
28	01 50 48.1	-74 25 30	1.82	1.29×10^{-14}	1.50×10^{-14}	0.56	0.291	0.188	0.198	-0.428	1.575	-1	1.575
29	01 47 50.6	-74 24 55	1.65	5.89×10^{-15}	3.01×10^{-15}	0.527	0.391	0.437	0.209	-0.356	0.531	-1	0.531
30	01 48 10.6	-74 38 08	1.47	3.39×10^{-14}	1.04×10^{-14}	1	0.212	0.225	0.288	0.014	0.225	0.336	0.225
31	01 47 46.8	-74 16 20	2.09	4.23×10^{-15}	1.37×10^{-14}	0.501	0.244	-1	0.281	1	8.844	-1	8.844
32	01 48 21.5	-74 19 18	2.42	1.32×10^{-14}	1.04×10^{-14}	0.578	0.318	0.178	0.227	-0.508	0.911	-0.313	0.911
33	01 49 37.9	-74 38 12	1.88	5.27×10^{-14}	2.13×10^{-14}	0.83	0.2	-0.376	0.219	-1	0.22	1	0.22
34	01 48 02.8	-74 40 53	2.13	5.51×10^{-15}	3.72×10^{-15}	0.43	0.273	0.059	0.239	-0.573	1.176	-1	1.176
35	01 48 49.5	-74 29 02	1.91	1.16×10^{-14}	5.36×10^{-15}	0.564	0.306	-0.13	0.273	-0.006	0.442	-0.405	0.442
36	01 51 05.4	-74 31 35	2.67	2.85×10^{-14}	2.00×10^{-14}	0.637	0.258	-0.145	0.243	-0.155	0.603	0.014	0.603
37	01 46 29.6	-74 27 54	1.57	2.09×10^{-14}	7.60×10^{-15}	-1	3.332	1	0.302	-0.126	0.281	0.182	0.281
38	01 45 35.3	-74 30 23	2.24	1.49×10^{-14}	1.07×10^{-14}	1	0.797	0.451	0.236	-0.389	0.626	-0.01	0.626
39	01 44 51.4	-74 26 34	2.05	1.05×10^{-13}	2.77×10^{-14}	0.114	0.567	-1	0.605	1	0.161	0.484	0.161
40	01 50 05.7	-74 25 45	2.41	3.70×10^{-15}	9.37×10^{-15}	0.914	0.218	-0.65	0.274	-0.073	4.065	-1	4.065

Table C.4: X-ray point source list of all detections in the pn camera in dataset MB1, corresponding image and HR plots are found in figure 2.8. Continuation of Table C.3.

pn Sources in Dataset MB1													
Source ID	R.A. [J2000]	Dec. [J2000]	σ(pos) [″]	Flux [erg cm^{-2} s^{-1}]	σ(Flux) [erg cm^{-2} s^{-1}]	HR_1	$\sigma(HR_1)$	HR_2	$\sigma(HR_2)$	HR_3	$\sigma(HR_3)$	HR_4	$\sigma(HR_4)$
41	01 47 15.3	-74 21 47	2	2.10×10^{-14}	1.27×10^{-14}	0.496	0.329	0.154	0.249	-0.359	0.496	0.184	0.496
42	01 46 18.6	-74 30 04	2.01	1.03×10^{-14}	6.76×10^{-15}	1	0.581	0.309	0.308	-0.007	0.556	-0.3	0.556
43	01 45 26.4	-74 21 53	1.66	1.11×10^{-13}	4.49×10^{-14}	0.491	0.259	-0.061	0.246	-0.441	0.261	0.664	0.261
44	01 49 25.1	-74 30 38	2.21	4.17×10^{-15}	3.23×10^{-15}	0.38	2.12	0.907	0.184	-0.321	0.707	-1	0.707
45	01 45 30.1	-74 21 07	1.98	9.60×10^{-15}	1.33×10^{-14}	-0.075	0.298	-0.392	0.423	0.068	1.471	-0.317	1.471
46	01 47 39.0	-74 28 51	2.88	1.82×10^{-15}	1.70×10^{-15}	0.175	0.297	-0.066	0.291	-1	> 10	-1	> 10
47	01 50 09.2	-74 39 51	2.14	4.12×10^{-15}	6.69×10^{-15}	-0.677	0.195	-0.735	0.743	-1	-	-	-
48	01 46 14.2	-74 31 58	2.24	4.28×10^{-15}	2.32×10^{-15}	-0.048	0.276	-0.59	0.393	0.445	0.477	-1	0.477
49	01 47 29.1	-74 27 18	1.85	1.98×10^{-14}	5.72×10^{-15}	0.022	0.785	0.536	0.455	-0.383	0.23	0.692	0.23
50	01 48 06.9	-74 42 38	3	3.87×10^{-14}	1.77×10^{-14}	-0.802	0.265	0.379	0.742	0.409	0.337	0.346	0.337
51	01 45 42.9	-74 31 57	2.05	1.43×10^{-15}	2.51×10^{-15}	-1	0.091	-	-	-	-	-	-
52	01 48 06.1	-74 29 30	1.83	8.51×10^{-15}	3.53×10^{-15}	1	0.216	0.432	0.267	-0.619	0.493	0.366	0.493
53	01 49 00.7	-74 37 33	1.81	5.05×10^{-15}	2.74×10^{-15}	0.685	0.33	-0.11	0.297	0.036	0.438	-1	0.438
54	01 48 24.1	-74 38 31	1.88	1.86×10^{-14}	9.50×10^{-15}	0.334	0.384	-0.038	0.343	0.211	0.408	0.015	0.408
55	01 49 16.8	-74 31 23	1.99	9.43×10^{-15}	5.58×10^{-15}	1	0.248	-0.007	0.301	-0.248	0.517	0.066	0.517
56	01 50 27.7	-74 26 29	2.61	1.34×10^{-14}	1.26×10^{-14}	-0.899	0.146	-1	3.261	-	0.229	1	0.229
57	01 47 09.0	-74 23 12	2.12	1.28×10^{-14}	9.35×10^{-15}	1	0.456	-0.233	0.294	-0.092	0.605	0.065	0.605
58	01 45 22.4	-74 31 22	2.46	2.52×10^{-14}	1.27×10^{-14}	1	> 10	0.998	0.184	-0.14	0.378	0.179	0.378
59	01 50 04.9	-74 37 34	1.68	1.33×10^{-14}	1.11×10^{-14}	0.716	0.284	-0.039	0.259	-0.297	0.796	-0.132	0.796
60	01 47 18.2	-74 23 41	2.02	2.02×10^{-14}	1.14×10^{-14}	0.746	0.742	0.519	0.308	-0.064	0.461	-0.035	0.461
61	01 49 58.6	-74 22 58	2.22	6.56×10^{-15}	1.29×10^{-14}	1	0.255	0.293	0.277	-0.349	2.261	-1	2.261

C.2 Field MB2

Table C.5: X-ray point source list of all detections in the MOS1 camera in dataset MB2, corresponding image and HR plots are found in figure 2.9.

MOS1 Sources in Dataset MB2													
Source ID	R.A. [J2000]	Dec. [J2000]	σ(pos) [″]	Flux [erg cm^{-2} s^{-1}]	σ(Flux) [erg cm^{-2} s^{-1}]	HR_1	$\sigma(HR_1)$	HR_2	$\sigma(HR_2)$	HR_3	$\sigma(HR_3)$	HR_4	$\sigma(HR_4)$
1	02 01 07.8	-72 55 45	0.15	2.33×10^{-12}	8.70×10^{-14}	0.185	0.022	0.023	0.021	-0.445	0.045	-0.335	0.045
2	01 59 16.7	-73 08 26	0.49	2.65×10^{-13}	3.87×10^{-14}	0.281	0.07	0.066	0.063	-0.436	0.165	-0.411	0.165
3	02 02 56.0	-72 59 16	0.79	1.06×10^{-13}	3.52×10^{-14}	0.502	0.091	-0.341	0.091	-0.652	1.019	-1	1.019
4	01 58 04.4	-72 51 04	1.05	6.94×10^{-14}	2.75×10^{-14}	0.43	0.191	0.3	0.141	-0.35	0.367	-0.755	0.367
5	01 59 26.3	-73 05 40	1.14	4.55×10^{-14}	1.66×10^{-14}	0.221	0.25	0.498	0.136	-0.707	0.396	0.086	0.396
6	01 57 01.6	-73 00 45	1.27	1.01×10^{-13}	4.13×10^{-14}	0.383	0.217	0.313	0.157	-0.405	0.383	-0.222	0.383
7	02 00 34.1	-72 54 33	1.17	2.67×10^{-14}	1.06×10^{-14}	0.388	0.191	0.054	0.167	-0.558	0.546	-0.608	0.546
8	02 00 54.0	-72 58 50	1.12	4.37×10^{-14}	1.50×10^{-14}	0.414	0.238	0.221	0.185	-0.434	0.327	0.015	0.327
9	01 59 07.2	-72 54 19	1.18	3.23×10^{-14}	1.15×10^{-14}	-	-	1	0.113	-0.168	0.209	-0.883	0.209
10	02 00 23.9	-73 02 18	1.11	1.98×10^{-14}	6.36×10^{-15}	0.871	0.332	0.59	0.163	-0.28	0.215	-0.847	0.215
11	01 58 54.8	-73 07 10	1.3	5.75×10^{-14}	2.57×10^{-14}	0.265	0.256	0.145	0.222	-0.171	0.382	-0.128	0.382
12	01 59 38.3	-73 05 24	1.29	1.90×10^{-14}	1.01×10^{-14}	-0.267	0.281	0.602	0.176	-0.659	0.688	-0.431	0.688
13	01 57 41.4	-72 53 41	1.54	2.91×10^{-14}	9.39×10^{-15}	0.162	0.305	0.426	0.194	-0.283	0.218	-1	0.218
14	01 59 49.2	-72 48 51	1.79	2.74×10^{-14}	1.69×10^{-14}	0.476	0.231	-0.035	0.22	-0.596	0.962	-0.641	0.962
15	02 02 37.2	-73 01 49	2.06	2.32×10^{-14}	1.51×10^{-14}	0.792	0.403	0.618	0.18	-0.806	1.068	-0.573	1.068
16	01 58 11.7	-73 02 58	1.98	4.55×10^{-14}	2.15×10^{-14}	1	8.798	0.967	0.142	-0.011	0.355	-0.269	0.355
17	02 00 55.5	-72 54 57	4.68	5.70×10^{-14}	3.36×10^{-14}	0.828	0.258	0.278	0.178	-0.814	1.519	-1	1.519
18	01 58 25.3	-73 07 58	2.03	2.12×10^{-14}	1.70×10^{-14}	0.272	0.268	-0.295	0.289	-0.57	1.078	0.049	1.078
19	02 01 18.8	-72 55 14	1.67	7.09×10^{-14}	2.98×10^{-14}	0.333	0.606	0.45	0.338	-0.058	0.329	0.094	0.329
20	01 58 28.5	-73 02 02	2.12	9.00×10^{-15}	9.41×10^{-15}	0.289	0.476	0.548	0.22	-0.633	1.372	-1	1.372
21	02 01 37.6	-72 51 59	1.47	6.66×10^{-14}	3.66×10^{-14}	0.249	0.438	0.524	0.214	-0.258	0.459	-0.251	0.459
22	02 01 24.3	-72 55 20	1.84	1.38×10^{-14}	8.59×10^{-15}	0.17	0.379	0.225	0.288	-0.333	0.585	-1	0.585
23	02 00 11.3	-72 48 06	1.88	3.25×10^{-14}	2.74×10^{-14}	1	0.134	-0.363	0.26	-0.412	0.925	-0.108	0.925
24	01 57 26.4	-72 59 31	2.07	1.55×10^{-14}	1.49×10^{-14}	-0.58	0.487	0.822	0.231	-1	1.799	1	1.799
25	02 02 33.0	-72 59 45	1.96	1.25×10^{-13}	4.84×10^{-14}	1	2.415	0.685	0.641	0.556	0.281	0.081	0.281
26	02 00 46.8	-72 49 45	2.2	3.85×10^{-14}	2.75×10^{-14}	1	0.939	0.61	0.226	-0.329	0.592	-0.386	0.592
27	02 00 30.1	-72 49 57	2.12	8.90×10^{-14}	4.02×10^{-14}	1	0.588	0.564	0.271	-0.135	0.351	0.122	0.351
28	01 57 54.9	-73 02 13	1.98	1.83×10^{-14}	1.32×10^{-14}	0.494	0.295	0.104	0.265	-0.41	0.761	-0.54	0.761
29	02 02 18.3	-72 52 22	1.66	3.11×10^{-14}	6.31×10^{-14}	1	0.389	0.157	0.269	-0.342	1.865	-1	1.865
30	02 01 25.9	-73 02 15	1.89	1.09×10^{-14}	6.90×10^{-15}	0.07	0.354	0.279	0.29	-0.447	0.689	-1	0.689
31	02 00 38.5	-73 03 50	2.11	2.19×10^{-14}	1.58×10^{-14}	0.285	0.455	0.298	0.302	-0.535	0.749	-0.148	0.749
32	01 59 15.7	-72 51 37	2.29	3.42×10^{-14}	3.01×10^{-14}	0.303	0.367	0.265	0.283	-0.629	0.697	0.307	0.697
33	01 58 48.9	-73 02 25	1.92	1.29×10^{-14}	8.29×10^{-15}	-0.185	0.358	0.241	0.347	-0.52	0.932	-1	0.932
34	01 59 50.0	-73 04 09	2.32	7.25×10^{-15}	5.23×10^{-15}	1	0.263	0.143	0.274	-1	4.28	1	4.28
35	02 00 40.4	-72 51 36	1.98	1.98×10^{-14}	1.85×10^{-14}	0.189	0.363	-0.013	0.352	-1	0.509	1	0.509
36	01 58 54.2	-72 53 41	2.45	1.19×10^{-14}	7.36×10^{-15}	0.407	0.392	0.133	0.368	0.093	0.357	-1	0.357
37	02 02 43.7	-72 59 47	2.93	1.00×10^{-13}	4.85×10^{-14}	0.016	1.002	0.767	0.278	-0.417	0.363	0.411	0.363
38	02 02 51.9	-72 56 23	2.64	9.39×10^{-14}	5.25×10^{-14}	0.674	0.392	-0.061	0.348	-0.205	0.44	0.423	0.44
39	02 01 15.3	-72 56 34	6.86	1.90×10^{-13}	1.12×10^{-13}	0.669	0.266	-0.544	0.314	0.211	0.493	-0.047	0.493

Table C.6: X-ray point source list of all detections in the MOS2 camera in dataset MB2, corresponding image and HR plots are found in figure 2.9.

MOS2 Sources in Dataset MB2													
Source ID	R.A. [J2000]	Dec. [J2000]	σ(pos) [″]	Flux [erg cm^{-2} s^{-1}]	σ(Flux) [erg cm^{-2} s^{-1}]	HR_1	$\sigma(HR_1)$	HR_2	$\sigma(HR_2)$	HR_3	$\sigma(HR_3)$	HR_4	$\sigma(HR_4)$
1	02 01 08.0	-72 55 46	0.18	2.53×10^{-12}	8.08×10^{-14}	0.212	0.023	0.081	0.02	-0.454	0.044	-0.398	0.044
2	01 59 16.6	-73 08 28	0.41	3.26×10^{-13}	4.32×10^{-14}	0.346	0.072	0.126	0.061	-0.543	0.158	-0.076	0.158
3	02 02 56.0	-72 59 17	0.82	1.51×10^{-13}	2.32×10^{-14}	0.499	0.093	-0.242	0.094	-0.645	0.408	-0.797	0.408
4	01 57 01.7	-73 00 46	1.03	1.48×10^{-13}	4.76×10^{-14}	0.528	0.168	0.075	0.148	-0.209	0.3	-0.148	0.3
5	01 59 37.9	-73 05 24	0.95	7.09×10^{-14}	1.71×10^{-14}	0.771	0.182	0.383	0.142	-0.529	0.246	0.203	0.246
6	02 01 36.7	-73 08 21	1.03	5.56×10^{-14}	2.22×10^{-14}	0.102	0.758	0.903	0.089	-0.305	0.32	-0.745	0.32
7	01 59 26.3	-73 05 39	1.2	5.03×10^{-14}	1.70×10^{-14}	0.478	0.189	0.104	0.172	-0.304	0.345	-0.207	0.345
8	01 58 04.7	-72 51 02	0.88	1.30×10^{-13}	4.31×10^{-14}	0.729	0.208	0.062	0.171	-0.136	0.303	-0.274	0.303
9	02 00 54.0	-72 58 50	1.04	3.31×10^{-14}	9.49×10^{-15}	0.008	0.242	0.323	0.191	-0.253	0.296	-0.625	0.296
10	01 58 55.4	-73 07 11	1.18	6.49×10^{-14}	2.20×10^{-14}	0.491	0.346	0.555	0.166	-0.431	0.315	0.003	0.315
11	02 00 34.0	-72 54 32	1.13	2.87×10^{-14}	1.02×10^{-14}	-0.249	0.256	0.4	0.224	-0.17	0.354	-0.828	0.354
12	01 58 40.3	-72 59 02	1.16	5.67×10^{-14}	2.12×10^{-14}	0.446	0.235	0.24	0.193	-0.317	0.346	-0.01	0.346
13	02 02 29.0	-72 52 05	1.18	9.30×10^{-14}	4.40×10^{-14}	0.089	0.235	0.016	0.242	-0.221	0.509	-0.192	0.509
14	02 00 41.8	-73 05 16	1.32	4.13×10^{-14}	1.66×10^{-14}	0.378	0.318	0.479	0.174	-0.634	0.419	0.135	0.419
15	01 57 41.6	-72 53 40	1.11	6.01×10^{-14}	3.02×10^{-14}	0.622	0.245	0.155	0.195	-0.616	0.583	0.003	0.583
16	02 01 51.7	-73 05 46	1.6	7.31×10^{-14}	3.25×10^{-14}	0.037	0.494	0.63	0.228	-0.101	0.363	-0.075	0.363
17	01 59 48.4	-72 48 50	2.02	2.66×10^{-14}	1.79×10^{-14}	0.492	0.295	0.189	0.21	-1	2.362	1	2.362
18	02 00 59.1	-72 54 58	2.37	1.73×10^{-14}	1.22×10^{-14}	1	0.299	0.586	0.228	-0.693	0.918	-0.454	0.918
19	01 58 25.7	-73 07 58	1.63	3.14×10^{-14}	1.90×10^{-14}	0.549	0.235	-0.334	0.242	-0.415	0.765	-0.051	0.765
20	02 00 23.7	-73 02 18	1.23	3.28×10^{-14}	1.01×10^{-14}	1	0.37	0.708	0.196	-0.236	0.278	-0.284	0.278
21	01 59 08.4	-72 54 16	4.86	3.88×10^{-13}	1.79×10^{-13}	0.304	0.162	-0.376	0.173	0.171	0.381	0.003	0.381
22	02 01 38.1	-72 52 00	1.35	8.27×10^{-14}	4.11×10^{-14}	1	0.386	0.685	0.198	-0.138	0.399	-0.355	0.399
23	02 02 36.8	-73 01 44	1.43	6.68×10^{-14}	3.83×10^{-14}	0.691	0.482	0.629	0.172	-0.566	0.512	0.049	0.512
24	02 02 18.6	-72 52 23	1.39	5.22×10^{-14}	3.38×10^{-14}	0.257	0.441	0.546	0.208	-0.449	0.665	-0.411	0.665
25	02 02 42.5	-72 59 46	1.78	3.36×10^{-14}	2.10×10^{-14}	0.267	0.313	-0.069	0.329	-0.045	0.637	-0.641	0.637
26	02 01 54.5	-73 07 06	1.51	2.07×10^{-14}	2.39×10^{-14}	0.158	0.326	0.233	0.261	-0.364	1.547	-1	1.547
27	02 00 03.1	-72 55 07	2.54	1.04×10^{-14}	6.04×10^{-15}	1	0.097	-0.091	0.251	-0.499	0.867	-1	0.867
28	02 02 31.2	-73 08 19	1.51	5.49×10^{-14}	3.06×10^{-14}	0.607	0.321	0.077	0.277	0.12	0.441	-0.684	0.441
29	01 57 54.4	-73 02 16	1.46	5.18×10^{-14}	2.54×10^{-14}	0.044	0.369	0.272	0.296	-0.331	0.404	0.3	0.404
30	02 00 11.6	-72 48 04	1.55	1.61×10^{-14}	3.18×10^{-14}	-0.141	0.571	0.829	0.144	-1	-	-	-
31	02 00 15.3	-73 09 50	1.6	5.92×10^{-14}	2.84×10^{-14}	-0.193	0.409	0.549	0.26	-0.473	0.363	0.416	0.363
32	01 58 28.3	-73 02 04	2.44	2.32×10^{-14}	1.50×10^{-14}	0.081	0.586	0.454	0.33	-0.031	0.537	-0.574	0.537
33	01 59 39.6	-72 47 11	2.07	1.67×10^{-13}	6.15×10^{-14}	1	0.266	0.196	0.334	-0.382	0.236	0.695	0.236
34	01 59 15.9	-72 51 38	1.57	1.75×10^{-14}	1.90×10^{-14}	-0.248	0.436	0.535	0.305	-0.192	1.051	-1	1.051
35	02 00 28.8	-72 50 33	1.96	4.57×10^{-14}	3.01×10^{-14}	-1	0.543	1	0.254	0.077	0.509	-0.551	0.509
36	01 58 42.4	-72 47 53	12.47	1.21×10^{-12}	7.61×10^{-13}	0.174	0.338	-0.877	0.249	0.757	0.479	0.211	0.479
37	02 00 52.1	-73 05 45	2.09	1.18×10^{-14}	8.69×10^{-15}	0.605	0.292	-0.283	0.34	-0.839	1.017	0.542	1.017
38	01 59 12.2	-72 52 52	2.06	1.83×10^{-13}	4.52×10^{-13}	0.454	0.254	-0.795	0.246	-1	-	-	-
39	02 01 25.8	-73 02 20	2.45	1.31×10^{-14}	1.01×10^{-14}	-0.372	0.327	0.185	0.421	-1	2.525	1	2.525
40	01 59 54.8	-72 47 13	1.92	5.27×10^{-14}	4.06×10^{-14}	0.351	0.503	0.315	0.356	0.015	0.623	-0.236	0.623

Table C.7: X-ray point source list of all detections in the pn camera in dataset MB2, corresponding image and HR plots are found in figure 2.11. Table continued C.8.

pn Sources in Dataset MB2													
Source ID	R.A. [J2000]	Dec. [J2000]	σ(pos) [″]	Flux [erg cm^{-2} s^{-1}]	σ(Flux) [erg cm^{-2} s^{-1}]	HR_1	$\sigma(HR_1)$	HR_2	$\sigma(HR_2)$	HR_3	$\sigma(HR_3)$	HR_4	$\sigma(HR_4)$
1	02 01 07.9	-72 55 45	0.11	2.03×10^{-12}	5.16×10^{-14}	0.179	0.014	-0.198	0.015	-0.455	0.037	-0.366	0.037
2	01 59 16.8	-73 08 27	0.36	3.00×10^{-13}	2.83×10^{-14}	0.258	0.047	-0.177	0.047	-0.295	0.104	-0.162	0.104
3	02 02 55.9	-72 59 14	0.53	1.25×10^{-13}	2.54×10^{-14}	0.521	0.043	-0.483	0.044	-0.73	0.544	-0.297	0.544
4	02 00 34.2	-72 54 33	0.64	4.61×10^{-14}	1.04×10^{-14}	0.335	0.097	-0.105	0.093	-0.308	0.257	-0.381	0.257
5	01 58 04.7	-72 51 05	0.62	1.06×10^{-13}	2.46×10^{-14}	0.478	0.096	-0.062	0.093	-0.243	0.227	-0.164	0.227
6	01 59 26.3	-73 05 39	0.69	3.72×10^{-14}	8.36×10^{-15}	0.49	0.107	0.007	0.097	-0.474	0.261	-0.198	0.261
7	01 59 38.0	-73 05 24	0.96	3.03×10^{-14}	8.72×10^{-15}	0.414	0.143	0.157	0.109	-0.549	0.317	-0.074	0.317
8	01 59 49.3	-72 48 49	0.99	3.56×10^{-14}	1.45×10^{-14}	0.541	0.096	-0.355	0.099	-0.561	0.664	-0.32	0.664
9	02 00 54.3	-72 58 51	0.86	1.54×10^{-14}	2.84×10^{-15}	0.274	0.131	0.091	0.116	-0.462	0.227	-1	0.227
10	02 00 58.7	-72 54 58	1.27	2.67×10^{-14}	9.97×10^{-15}	0.606	0.181	-0.195	0.171	0.003	0.361	-0.557	0.361
11	01 58 40.6	-72 59 02	0.94	1.58×10^{-14}	3.19×10^{-15}	0.256	0.135	-0.119	0.129	-0.152	0.19	-1	0.19
12	01 59 07.5	-72 54 20	0.92	5.00×10^{-14}	1.21×10^{-14}	0.622	0.195	0.323	0.131	-0.071	0.215	-0.282	0.215
13	02 00 23.8	-73 02 18	0.95	2.30×10^{-14}	5.30×10^{-15}	0.717	0.34	0.55	0.144	-0.038	0.193	-0.649	0.193
14	02 01 54.9	-72 54 03	1.02	8.31×10^{-15}	4.16×10^{-15}	-0.95	0.068	-1	2.057	-	-	-	-
15	02 02 31.0	-73 08 21	1.23	6.94×10^{-14}	3.41×10^{-14}	0.276	0.136	-0.707	0.14	0.177	0.382	0.287	0.382
16	02 00 42.0	-73 05 15	0.96	4.86×10^{-14}	1.10×10^{-14}	0.549	0.144	0.029	0.133	-0.431	0.19	0.364	0.19
17	02 01 52.5	-73 05 45	1.37	1.60×10^{-14}	8.44×10^{-15}	-0.13	0.24	0.506	0.159	-0.407	0.645	-1	0.645
18	02 01 24.6	-72 55 21	1.31	3.86×10^{-14}	1.47×10^{-14}	0.153	0.198	0.096	0.174	-0.745	0.283	0.662	0.283
19	02 01 37.9	-72 51 56	1.17	3.49×10^{-14}	1.64×10^{-14}	1	0.117	0.33	0.159	-0.193	0.443	-0.549	0.443
20	02 01 17.6	-72 55 17	2	1.49×10^{-14}	9.85×10^{-15}	0.215	0.329	-0.1	0.328	-0.019	0.624	-0.311	0.624
21	02 02 29.0	-72 52 06	1.14	2.94×10^{-14}	1.94×10^{-14}	0.348	0.157	-0.021	0.144	-0.266	0.82	-1	0.82
22	01 58 55.0	-72 53 44	1.22	2.00×10^{-14}	1.01×10^{-14}	0.222	0.189	0.033	0.172	-0.472	0.538	-0.06	0.538
23	02 00 52.2	-73 05 44	1.46	6.23×10^{-15}	6.44×10^{-15}	0.396	0.158	-0.622	0.168	-0.166	2.058	-1	2.058
24	02 00 29.5	-72 50 34	1.4	5.59×10^{-14}	1.96×10^{-14}	0.471	0.233	0.224	0.168	-0.29	0.286	0.166	0.286
25	01 58 41.7	-73 08 33	1.35	1.98×10^{-14}	1.18×10^{-14}	-0.107	0.161	-0.441	0.209	-1	0.257	1	0.257
26	01 57 54.8	-73 02 14	1.34	7.15×10^{-15}	4.33×10^{-15}	0.277	0.207	0.127	0.171	-0.855	2.998	-1	2.998
27	01 59 15.4	-72 51 38	1.4	2.17×10^{-14}	1.34×10^{-14}	0.147	0.204	0.087	0.178	-0.653	0.589	0.245	0.589
28	02 01 19.3	-72 58 28	1.27	8.78×10^{-15}	5.27×10^{-15}	0.364	0.187	-0.113	0.164	-0.653	1.216	-0.604	1.216
29	01 57 13.6	-72 58 33	1.7	7.86×10^{-14}	2.18×10^{-14}	0.466	0.289	0.25	0.195	-0.044	0.219	0.159	0.219
30	01 58 49.2	-73 02 26	1.31	1.45×10^{-14}	6.16×10^{-15}	0.086	0.194	-0.119	0.2	-0.265	0.447	-0.11	0.447
31	02 02 18.1	-72 52 23	1.27	3.72×10^{-14}	2.25×10^{-14}	0.605	0.292	0.336	0.159	-0.302	0.609	-0.505	0.609
32	02 03 08.3	-73 03 53	2	7.07×10^{-14}	4.66×10^{-14}	-0.064	0.215	-0.056	0.259	0.176	0.521	-0.033	0.521
33	02 01 54.7	-73 07 04	1.47	9.39×10^{-15}	7.59×10^{-15}	0.074	0.178	-0.395	0.231	-0.26	1.465	-1	1.465
34	02 01 26.1	-73 02 15	1.51	1.42×10^{-14}	6.80×10^{-15}	0.195	0.241	0.162	0.207	-0.206	0.491	-0.564	0.491
35	02 01 37.1	-73 08 17	1.78	3.46×10^{-14}	2.32×10^{-14}	1	0.087	0.167	0.182	-0.739	0.705	0.18	0.705
36	01 59 19.3	-72 57 44	1.82	1.29×10^{-14}	5.29×10^{-15}	0.634	0.256	-0.052	0.215	-0.139	0.397	-0.246	0.397
37	02 02 42.5	-72 59 50	2.26	6.48×10^{-14}	4.14×10^{-14}	0.211	0.238	-0.187	0.236	-0.156	0.527	0.137	0.527
38	02 00 38.4	-73 03 50	1.51	7.61×10^{-15}	3.83×10^{-15}	0.249	0.199	-0.158	0.196	-0.546	0.785	-0.39	0.785
39	02 02 37.2	-73 01 46	1.79	1.75×10^{-14}	1.35×10^{-14}	0.487	0.272	0.213	0.187	-0.191	0.789	-1	0.789
40	01 57 41.1	-73 04 34	2.24	1.34×10^{-14}	8.44×10^{-15}	0.178	0.245	0.068	0.211	-0.134	0.66	-1	0.66

Table C.8: X-ray point source list of all detections in the pn camera in dataset MB2, corresponding image and HR plots are found in figure 2.11. Continuation of table C.7.

pn Sources in Dataset MB2													
Source ID	R.A. [J2000]	Dec. [J2000]	σ(pos) [″]	Flux [erg cm^{-2} s^{-1}]	σ(Flux) [erg cm^{-2} s^{-1}]	HR_1	$\sigma(HR_1)$	HR_2	$\sigma(HR_2)$	HR_3	$\sigma(HR_3)$	HR_4	$\sigma(HR_4)$
41	02 01 31.6	-72 46 53	1.51	9.37×10^{-14}	5.65×10^{-14}	0.038	0.211	-0.187	0.242	-0.06	0.357	0.46	0.357
42	02 00 55.1	-72 54 25	2.09	5.69×10^{-15}	5.49×10^{-15}	-0.333	0.261	0.098	0.342	-1	3.995	1	3.995
43	01 58 12.3	-73 03 03	1.41	3.64×10^{-14}	1.21×10^{-14}	-1	3.654	1	0.112	0.027	0.264	0.003	0.264
44	01 59 41.4	-72 47 07	1.7	1.52×10^{-14}	8.42×10^{-15}	0.271	0.25	0.116	0.207	-0.321	0.657	-1	0.657
45	01 57 38.9	-73 02 29	1.57	6.68×10^{-15}	7.51×10^{-15}	-0.105	0.2	-0.247	0.239	-0.441	2.579	-1	2.579
46	02 00 55.9	-73 08 26	1.29	7.79×10^{-15}	9.16×10^{-15}	0.774	0.204	-0.113	0.183	-0.44	1.857	-1	1.857
47	02 01 47.1	-72 53 52	1.67	5.00×10^{-15}	7.03×10^{-15}	-0.888	0.164	-1	3.268	1	1.762	-1	1.762
48	02 01 31.6	-73 03 22	1.89	6.37×10^{-15}	5.87×10^{-15}	0.309	0.236	-0.176	0.237	-0.228	1.213	-1	1.213
49	02 01 34.8	-72 55 27	1.69	5.04×10^{-15}	1.08×10^{-14}	0.409	0.262	0.049	0.219	-1	-	-	-
50	01 59 36.5	-72 46 22	1.64	6.47×10^{-15}	3.77×10^{-14}	0.265	0.204	-0.462	0.266	-1	-	-	-
51	01 58 46.3	-72 59 28	1.56	4.31×10^{-15}	3.64×10^{-15}	-0.001	0.26	0.201	0.228	-0.668	1.993	-1	1.993
52	02 00 10.6	-72 48 06	1.87	4.65×10^{-14}	2.65×10^{-14}	0.461	0.254	0.019	0.238	0.069	0.509	-0.743	0.509
53	01 59 50.1	-73 04 07	2.21	5.43×10^{-15}	3.21×10^{-15}	1	0.337	-0.127	0.257	-0.02	0.532	-1	0.532
54	02 01 23.0	-72 52 41	1.69	2.51×10^{-14}	1.58×10^{-14}	0.711	0.389	0.423	0.229	-0.374	0.533	0.049	0.533
55	02 02 33.5	-72 59 44	2.57	3.65×10^{-14}	1.79×10^{-14}	-0.25	0.446	-1	0.406	1	0.375	-0.265	0.375
56	02 03 20.4	-72 58 04	1.91	1.24×10^{-14}	3.36×10^{-14}	0.593	0.225	-0.031	0.203	-0.668	6.755	-1	6.755
57	02 00 46.7	-72 49 44	1.89	1.13×10^{-14}	1.42×10^{-14}	0.445	0.437	0.375	0.25	-0.185	1.234	-1	1.234
58	02 00 21.6	-72 47 00	2.02	3.90×10^{-14}	3.59×10^{-14}	0.132	0.218	-0.607	0.468	0.11	1.315	-1	1.315
59	01 57 26.0	-72 59 34	1.94	2.49×10^{-14}	1.65×10^{-14}	0.289	0.267	0.025	0.243	-0.769	0.39	0.724	0.39
60	02 00 31.1	-72 50 00	2.02	2.94×10^{-14}	1.65×10^{-14}	1	0.261	0.208	0.226	-0.157	0.498	-0.228	0.498
61	01 59 57.2	-72 59 51	1.86	7.19×10^{-15}	3.73×10^{-15}	-0.281	0.283	0.175	0.313	-0.267	0.556	-0.213	0.556
62	02 00 59.5	-72 53 54	2.26	7.46×10^{-14}	5.22×10^{-14}	0.385	0.285	-0.352	0.252	-0.807	0.479	0.795	0.479
63	01 58 18.1	-72 57 09	2.03	1.11×10^{-14}	9.05×10^{-15}	0.48	0.312	0.102	0.269	-0.415	0.768	-0.007	0.768
64	01 59 58.4	-73 03 02	1.98	7.60×10^{-15}	3.88×10^{-15}	0.198	0.462	0.449	0.268	-0.66	0.565	0.174	0.565
65	02 00 21.2	-72 53 24	2.35	5.25×10^{-15}	7.49×10^{-15}	0.166	0.417	0.388	0.279	-0.393	1.773	-1	1.773
66	02 03 10.7	-72 55 07	1.51	4.84×10^{-12}	1.05×10^{-12}	-1	0.297	-	-	1	0.089	0.856	0.089
67	02 00 24.4	-72 47 32	2.7	1.79×10^{-14}	3.32×10^{-14}	0.196	0.29	-0.218	0.295	-1	-	-	-
68	02 00 35.2	-73 08 49	2.05	8.56×10^{-15}	6.66×10^{-15}	0.332	0.44	0.302	0.283	-0.189	0.761	-0.673	0.761
69	01 58 35.2	-73 03 44	5.5	8.79×10^{-14}	7.63×10^{-14}	-0.255	0.192	-0.429	0.34	-1	0.521	1	0.521
70	02 00 29.2	-72 48 37	5.12	3.92×10^{-14}	4.55×10^{-14}	0.125	0.198	-0.923	0.252	0.864	1.174	-1	1.174
71	01 57 56.1	-72 58 56	2.25	8.79×10^{-15}	5.41×10^{-15}	0.473	0.355	0.051	0.286	0.153	0.485	-1	0.485
72	02 00 47.6	-73 04 21	1.81	2.91×10^{-14}	8.82×10^{-15}	-	-	-	-	1	0.225	0.279	0.225
73	02 01 18.3	-72 57 28	2.1	8.28×10^{-15}	6.41×10^{-15}	0.723	0.344	-0.365	0.305	-0.085	0.855	-1	0.855
74	01 59 8	-73 00 57	1.8	1.08×10^{-14}	4.41×10^{-15}	-1	1.053	1	0.194	-0.182	0.369	-0.323	0.369

C.3 Field MB3

Table C.9: X-ray point source list of all detections in the MOS1 camera in dataset MB3, corresponding image and HR plots are found in figure 2.12.

MOS1 Sources in Dataset MB3													
Source ID	R.A. [J2000]	Dec. [J2000]	σ(pos) [″]	Flux [erg cm^{-2} s^{-1}]	σ(Flux) [erg cm^{-2} s^{-1}]	HR_1	$\sigma(HR_1)$	HR_2	$\sigma(HR_2)$	HR_3	$\sigma(HR_3)$	HR_4	$\sigma(HR_4)$
1	02 24 27.7	-73 54 08	0.27	1.94×10^{-13}	7.88×10^{-15}	0.405	0.042	-0.205	0.041	-0.759	0.053	-1	0.053
2	02 21 41.2	-73 56 33	0.58	1.12×10^{-13}	2.49×10^{-14}	-0.745	0.051	-0.929	0.125	-0.384	0.537	0.786	0.537
3	02 22 48.5	-73 48 58	0.79	9.73×10^{-14}	2.38×10^{-14}	0.452	0.157	0.191	0.126	-0.225	0.218	-0.337	0.218
4	02 22 55.4	-73 47 53	1.29	6.85×10^{-14}	2.65×10^{-14}	0.491	0.191	0.04	0.155	-0.342	0.393	-0.504	0.393
5	02 26 33.8	-73 51 38	1.19	9.16×10^{-14}	3.67×10^{-14}	0.294	0.218	0.254	0.167	-0.45	0.393	-0.159	0.393
6	02 21 01.5	-73 59 59	1.52	2.15×10^{-14}	2.73×10^{-14}	0.499	0.164	-0.811	0.164	-0.796	> 10	-1	> 10
7	02 23 39.5	-73 51 33	1.04	1.80×10^{-14}	3.55×10^{-15}	0.483	0.235	0.289	0.169	-0.348	0.104	-1	0.104
8	02 23 55.2	-73 54 02	1.21	1.63×10^{-14}	5.18×10^{-15}	0.335	0.264	0.16	0.209	-0.202	0.248	-0.837	0.248
9	02 22 49.8	-73 51 22	1.34	1.05×10^{-13}	3.08×10^{-14}	1	1.053	0.721	0.209	-0.008	0.238	-0.038	0.238
10	02 24 57.7	-73 59 32	1.88	9.06×10^{-15}	8.19×10^{-15}	0.817	0.21	-0.628	0.238	-0.867	11.86	-1	11.86
11	02 25 07.0	-74 00 38	1.94	5.04×10^{-14}	2.68×10^{-14}	0.302	0.362	0.154	0.288	0.132	0.411	-0.335	0.411
12	02 25 48.3	-73 52 46	1.65	3.89×10^{-14}	2.36×10^{-14}	0.437	0.308	0.114	0.26	-0.366	0.545	0.002	0.545
13	02 23 33.3	-73 56 03	1.57	2.45×10^{-14}	9.40×10^{-15}	0.627	0.298	0.267	0.231	-0.458	0.392	-0.096	0.392
14	02 21 30.3	-74 02 17	1.57	4.25×10^{-14}	3.15×10^{-14}	0.545	0.295	0.11	0.239	-0.237	0.669	-0.598	0.669
15	02 21 07.8	-73 48 59	1.78	2.75×10^{-14}	1.47×10^{-14}	0.34	0.385	0.153	0.321	0.22	0.299	-0.981	0.299
16	02 24 01.4	-73 53 17	1.24	1.56×10^{-14}	6.38×10^{-15}	0.475	0.489	0.538	0.22	-0.195	0.284	-0.803	0.284
17	02 24 31.1	-73 44 49	1.69	4.84×10^{-14}	2.47×10^{-14}	0.533	0.287	-0.207	0.335	-0.227	0.425	0.29	0.425
18	02 24 58.0	-73 52 46	1.72	1.29×10^{-14}	6.85×10^{-15}	0.083	0.341	0.233	0.285	-0.509	0.642	-0.486	0.642
19	02 22 57.2	-73 43 09	3.32	4.26×10^{-13}	2.36×10^{-13}	0.231	0.159	-0.604	0.212	-0.583	2.684	-1	2.684
20	02 24 02.0	-73 49 39	1.83	1.33×10^{-14}	7.77×10^{-15}	0.726	0.323	0.045	0.298	-0.226	0.524	-0.577	0.524
21	02 23 20.3	-73 58 14	2.31	2.06×10^{-14}	1.14×10^{-14}	0.587	0.58	0.618	0.238	-0.44	0.507	-0.338	0.507
22	02 24 46.0	-73 47 49	2.37	2.40×10^{-14}	1.53×10^{-14}	1	0.76	0.786	0.214	-0.63	0.63	0.007	0.63
23	02 26 11.7	-73 48 09	1.66	3.55×10^{-14}	2.59×10^{-14}	0.069	0.308	0.142	0.276	-0.412	0.772	-0.244	0.772
24	02 25 05.4	-74 05 17	2.39	2.32×10^{-14}	2.11×10^{-14}	-0.244	0.61	0.628	0.359	-0.033	0.582	-0.955	0.582
25	02 25 44.9	-74 03 55	1.7	1.76×10^{-14}	1.30×10^{-14}	-0.038	0.341	-0.042	0.388	-0.054	0.665	-1	0.665
26	02 24 40.7	-73 58 06	1.56	2.53×10^{-14}	1.24×10^{-14}	1	0.287	0.562	0.275	-0.645	0.474	0.325	0.474
27	02 21 52.4	-73 50 54	1.88	5.86×10^{-14}	3.03×10^{-14}	1	3.879	0.857	0.427	0.343	0.368	-0.062	0.368
28	02 27 01.7	-73 56 12	1.93	4.11×10^{-12}	1.41×10^{-12}	0.693	0.553	0.027	0.528	-0.198	0.139	0.861	0.139

Table C.10: X-ray point source list of all detections in the MOS2 camera in dataset MB3, corresponding image and HR plots are found in figure 2.12.

MOS2 Sources in Dataset MB3													
Source ID	R.A. [J2000]	Dec. [J2000]	σ(pos) [″]	Flux [erg cm^{-2} s^{-1}]	σ(Flux) [erg cm^{-2} s^{-1}]	HR_1	$\sigma(HR_1)$	HR_2	$\sigma(HR_2)$	HR_3	$\sigma(HR_3)$	HR_4	$\sigma(HR_4)$
1	02 24 27.9	-73 54 08	0.27	2.43×10^{-13}	9.38×10^{-15}	0.451	0.041	-0.182	0.041	-0.757	0.04	-1	0.04
2	02 21 41.6	-73 56 34	0.52	1.50×10^{-13}	1.24×10^{-14}	-0.635	0.052	-0.784	0.133	-1	-	-	-
3	02 22 50.1	-73 51 23	0.88	7.62×10^{-14}	1.86×10^{-14}	0.393	0.337	0.718	0.113	-0.308	0.219	-0.324	0.219
4	02 22 56.1	-73 47 52	1.02	1.28×10^{-13}	3.96×10^{-14}	0.272	0.213	0.244	0.162	-0.385	0.313	-0.08	0.313
5	02 22 48.5	-73 48 59	1.01	1.25×10^{-13}	5.14×10^{-14}	0.316	0.218	0.361	0.148	-0.555	0.401	0.108	0.401
6	02 23 53.8	-74 01 56	1.2	4.71×10^{-14}	1.91×10^{-14}	0.531	0.246	0.301	0.166	-0.464	0.43	-0.212	0.43
7	02 22 53.1	-74 01 33	1.08	4.38×10^{-14}	1.74×10^{-14}	0.919	0.394	0.771	0.127	-0.211	0.307	-0.699	0.307
8	02 23 39.8	-73 51 32	0.98	3.49×10^{-14}	1.17×10^{-14}	0.437	0.295	0.474	0.162	-0.443	0.349	-0.306	0.349
9	02 23 08.6	-73 48 02	1.15	5.18×10^{-14}	2.26×10^{-14}	-0.022	0.288	0.524	0.173	-0.454	0.45	-0.178	0.45
10	02 24 57.9	-73 59 32	1.37	1.52×10^{-14}	1.26×10^{-14}	0.46	0.182	-0.537	0.215	-1	-	-	-
11	02 21 01.3	-74 00 02	1.43	2.57×10^{-14}	1.34×10^{-14}	0.692	0.15	-0.554	0.186	-0.872	8.142	-1	8.142
12	02 22 51.8	-73 43 30	1.43	8.68×10^{-14}	3.74×10^{-14}	1	1.15	0.651	0.219	-0.023	0.336	-0.313	0.336
13	02 21 07.4	-73 49 00	1.44	7.66×10^{-14}	3.85×10^{-14}	0.835	0.212	-0.075	0.226	-0.488	0.477	0.305	0.477
14	02 23 00.6	-74 05 17	1.55	3.18×10^{-14}	1.22×10^{-14}	0.673	0.276	0.436	0.184	-0.365	0.339	-1	0.339
15	02 26 33.5	-73 51 38	1.86	3.96×10^{-14}	2.70×10^{-14}	0.526	0.276	0.063	0.229	-0.478	1.072	-1	1.072
16	02 24 02.1	-73 53 15	1.26	3.87×10^{-14}	1.07×10^{-14}	0.394	0.314	-0.008	0.296	0.228	0.251	-0.247	0.251
17	02 25 04.9	-74 05 14	1.56	4.26×10^{-14}	2.75×10^{-14}	0.446	0.279	-0.093	0.296	0.235	0.518	-0.734	0.518
18	02 24 58.3	-73 52 44	1.44	1.62×10^{-14}	9.61×10^{-15}	1	0.13	0.316	0.232	-0.114	0.429	-1	0.429
19	02 23 19.8	-73 58 11	1.5	9.24×10^{-15}	5.01×10^{-15}	0.639	0.316	0.088	0.253	-0.428	0.686	-1	0.686
20	02 23 05.8	-74 02 05	1.77	6.16×10^{-14}	2.66×10^{-14}	1	1.199	0.855	0.192	-0.392	0.323	0.297	0.323
21	02 25 44.5	-74 03 51	1.66	2.66×10^{-14}	2.23×10^{-14}	0.588	0.425	0.172	0.374	0.266	0.518	-1	0.518
22	02 23 33.0	-73 56 01	1.61	1.94×10^{-14}	7.49×10^{-15}	-1	1.409	1	0.594	0.416	0.254	-0.636	0.254
23	02 23 38.5	-73 47 44	1.74	4.64×10^{-14}	2.24×10^{-14}	0.705	0.422	0.134	0.266	-0.329	0.435	0.083	0.435
24	02 21 52.3	-73 50 55	1.43	1.73×10^{-13}	4.38×10^{-14}	-	-	1	0.318	0.307	0.166	0.646	0.166
25	02 24 30.2	-73 41 30	6.68	1.08×10^{-13}	1.31×10^{-13}	0.323	0.166	-0.836	0.225	-0.578	19.925	-1	19.925
26	02 25 07.6	-74 00 36	1.74	1.27×10^{-13}	5.88×10^{-14}	-0.303	0.452	0.657	0.251	-0.498	0.32	0.514	0.32
27	02 23 02.4	-74 06 57	1.57	2.20×10^{-14}	1.54×10^{-14}	1	>10	0.991	0.157	-0.058	0.399	-1	0.399
28	02 24 56.8	-73 57 10	1.32	2.10×10^{-14}	8.83×10^{-15}	-	-	1	0.147	0.074	0.28	-0.662	0.28
29	02 22 43.7	-74 06 06	1.66	9.47×10^{-14}	4.04×10^{-14}	-0.122	2.213	0.825	0.615	0.653	0.311	-0.139	0.311
30	02 22 00.7	-73 44 02	1.31	6.34×10^{-14}	3.38×10^{-14}	0.082	1.182	0.902	0.161	-0.458	0.452	0.1	0.452
31	02 23 17.3	-73 52 06	2.7	1.10×10^{-14}	6.26×10^{-15}	1	>10	0.997	0.183	-0.07	0.299	-1	0.299
32	02 22 11.7	-74 02 40	1.7	2.71×10^{-14}	2.11×10^{-14}	0.67	0.401	-0.143	0.371	-0.002	0.701	-0.276	0.701
33	02 24 09.3	-74 08 05	6.82	6.89×10^{-13}	1.61×10^{-13}	-0.969	0.53	0.981	0.34	-1	0.106	1	0.106
34	02 23 24.9	-73 53 05	1.82	1.50×10^{-14}	9.94×10^{-15}	0.648	0.491	0.48	0.271	-0.482	0.661	-0.2	0.661
35	02 23 54.5	-73 54 00	1.84	1.07×10^{-14}	4.61×10^{-15}	1	0.219	0.105	0.313	-0.359	0.342	-1	0.342
36	02 22 28.8	-74 01 23	1.61	3.46×10^{-14}	3.50×10^{-14}	0.331	0.399	0.224	0.313	-0.946	0.402	0.925	0.402
37	02 24 07.7	-73 47 16	2.25	4.58×10^{-13}	2.23×10^{-13}	0.189	0.333	-1	0.238	1	0.64	0.496	0.64
38	02 26 53.9	-73 56 15	2.45	1.40×10^{-14}	2.49×10^{-14}	1	0.814	0.543	0.236	-0.765	3.791	-1	3.791
39	02 23 04.5	-73 52 41	1.99	2.52×10^{-14}	1.18×10^{-14}	0.584	0.912	0.773	0.21	-1	0.324	1	0.324

Table C.11: X-ray point source list of all detections in the pn camera in dataset MB3, corresponding image and HR plots are found in figure 2.14. Table continued C.12.

pn Sources in Dataset MB3													
Source ID	R.A. [J2000]	Dec. [J2000]	σ(pos) [″]	Flux [erg cm^{-2} s^{-1}]	σ(Flux) [erg cm^{-2} s^{-1}]	HR_1	$\sigma(HR_1)$	HR_2	$\sigma(HR_2)$	HR_3	$\sigma(HR_3)$	HR_4	$\sigma(HR_4)$
1	02 21 41.5	-73 56 34	0.36	6.41×10^{-14}	1.10×10^{-14}	-0.564	0.033	-0.937	0.043	-1	-	-	-
2	02 22 48.6	-73 48 58	0.52	6.60×10^{-14}	1.18×10^{-14}	0.447	0.091	0.056	0.077	-0.455	0.206	-0.233	0.206
3	02 22 55.6	-73 47 53	0.7	6.26×10^{-14}	1.35×10^{-14}	0.363	0.099	0.023	0.087	-0.524	0.257	-0.152	0.257
4	02 24 27.7	-73 54 07	0.74	1.80×10^{-13}	1.87×10^{-14}	0.478	0.059	-0.484	0.059	-0.529	0.203	-0.845	0.203
5	02 22 50.2	-73 51 26	0.93	4.92×10^{-14}	8.94×10^{-15}	0.783	0.212	0.55	0.1	-0.176	0.165	-0.468	0.165
6	02 23 39.7	-73 51 34	0.77	2.47×10^{-14}	4.70×10^{-15}	0.364	0.124	0.081	0.105	-0.417	0.23	-0.572	0.23
7	02 26 33.9	-73 51 37	0.95	4.01×10^{-14}	1.40×10^{-14}	0.187	0.122	0.036	0.113	-0.575	0.547	-0.511	0.547
8	02 23 08.7	-73 48 01	0.81	2.52×10^{-14}	8.15×10^{-15}	0.344	0.116	-0.176	0.115	-0.4	0.441	-0.55	0.441
9	02 22 58.8	-74 05 11	0.97	4.55×10^{-14}	1.84×10^{-14}	0.502	0.147	0.102	0.117	-0.407	0.471	-0.471	0.471
10	02 25 07.5	-74 00 35	1.06	4.38×10^{-14}	1.44×10^{-14}	0.47	0.174	0.13	0.14	-0.366	0.305	0.02	0.305
11	02 25 48.5	-73 52 45	1.13	1.59×10^{-14}	1.15×10^{-14}	0.48	0.157	0.13	0.132	-0.574	1.307	-1	1.307
12	02 23 53.7	-74 01 54	1.05	2.80×10^{-14}	9.67×10^{-15}	0.462	0.15	0.051	0.133	-0.383	0.386	-0.368	0.386
13	02 24 57.7	-73 59 33	1.1	2.27×10^{-14}	9.97×10^{-15}	0.562	0.116	-0.819	0.108	-1	0.121	1	0.121
14	02 23 20.0	-73 58 14	1.16	2.31×10^{-14}	7.23×10^{-15}	0.737	0.187	-0.049	0.15	-0.384	0.315	0.025	0.315
15	02 23 21.6	-73 47 55	2.45	1.33×10^{-13}	2.53×10^{-14}	0.244	0.22	0.31	0.155	0.064	0.156	0.01	0.156
16	02 24 57.9	-73 52 43	1.01	3.11×10^{-14}	8.31×10^{-15}	0.663	0.182	0.114	0.154	-0.267	0.257	-0.064	0.257
17	02 23 32.9	-73 56 02	1.14	1.32×10^{-14}	4.14×10^{-15}	0.894	0.215	0.423	0.139	-0.436	0.339	-0.585	0.339
18	02 25 05.4	-74 05 15	1.26	1.99×10^{-14}	1.14×10^{-14}	0.619	0.255	0.366	0.162	-0.365	0.647	-1	0.647
19	02 23 09.0	-73 47 09	1.38	1.10×10^{-14}	6.85×10^{-15}	0.321	0.204	0.122	0.166	-0.479	0.947	-1	0.947
20	02 24 31.4	-73 44 52	1.28	1.10×10^{-14}	8.36×10^{-15}	0.513	0.157	-0.321	0.166	-0.401	1.367	-1	1.367
21	02 24 22.7	-73 51 17	1.18	5.81×10^{-14}	9.63×10^{-15}	0.667	0.563	-0.363	0.595	0.788	0.138	0.378	0.138
22	02 23 06.2	-74 02 04	1.42	1.32×10^{-14}	6.06×10^{-15}	1	0.12	0.473	0.163	-0.286	0.434	-1	0.434
23	02 26 11.5	-73 48 10	1.24	6.01×10^{-14}	2.17×10^{-14}	0.343	0.191	-0.097	0.172	-0.793	0.233	0.813	0.233
24	02 23 54.9	-73 54 01	1.26	1.72×10^{-14}	4.54×10^{-15}	0.614	0.212	-0.084	0.193	0.013	0.253	-0.313	0.253
25	02 23 52.0	-74 02 52	1.63	1.81×10^{-14}	1.16×10^{-14}	0.852	0.153	-0.175	0.169	-0.654	0.691	0.209	0.691
26	02 22 00.7	-73 44 01	1.41	3.06×10^{-14}	1.58×10^{-14}	0.711	0.233	0.138	0.189	-0.267	0.519	-0.421	0.519
27	02 24 39.9	-74 00 47	2.04	4.19×10^{-14}	1.43×10^{-14}	0.108	0.359	0.239	0.289	0.107	0.261	0.198	0.261
28	02 22 11.6	-74 02 39	1.52	1.58×10^{-14}	1.02×10^{-14}	0.081	0.26	0.152	0.226	-0.246	0.703	-0.599	0.703
29	02 23 17.5	-73 52 05	1.85	7.23×10^{-15}	2.52×10^{-15}	-1	2.672	1	0.162	-0.132	0.232	-0.987	0.232
30	02 22 36.2	-73 43 22	1.83	3.97×10^{-14}	1.96×10^{-14}	0.45	0.297	0.039	0.239	-0.01	0.425	-0.088	0.425
31	02 24 42.4	-73 47 17	1.76	9.94×10^{-15}	6.87×10^{-15}	0.461	0.238	0.158	0.206	-0.869	1.028	0.295	1.028
32	02 23 56.4	-74 05 32	1.59	1.32×10^{-14}	5.76×10^{-15}	-0.16	0.363	0.593	0.205	-0.336	0.427	-1	0.427
33	02 22 07.8	-73 58 05	1.84	6.19×10^{-15}	7.45×10^{-15}	0.66	0.238	-0.372	0.238	-0.082	1.473	-1	1.473
34	02 22 12.3	-73 43 42	1.84	7.41×10^{-15}	1.11×10^{-14}	0.636	0.215	-0.164	0.236	-0.628	3.654	-1	3.654
35	02 22 29.3	-74 01 22	1.6	1.64×10^{-14}	1.21×10^{-14}	0.249	0.207	-0.675	0.247	-1	0.432	1	0.432
36	02 27 48.6	-73 51 02	2.86	1.50×10^{-13}	6.17×10^{-14}	0.669	0.291	0.33	0.2	-0.342	0.231	0.542	0.231
37	02 23 38.2	-73 47 42	1.79	3.73×10^{-14}	1.23×10^{-14}	0.318	0.527	0.4	0.349	-0.419	0.21	0.676	0.21
38	02 24 47.2	-73 47 54	2.43	4.58×10^{-14}	2.75×10^{-14}	1	0.452	0.134	0.239	-0.344	0.656	-0.787	0.656
39	02 22 00.8	-73 51 49	2.16	2.32×10^{-14}	1.17×10^{-14}	-0.85	1.132	0.971	0.236	-0.185	0.377	0.229	0.377
40	02 21 32.3	-73 59 06	1.85	5.32×10^{-14}	1.92×10^{-14}	0.731	0.293	0.049	0.268	-0.233	0.232	0.556	0.232

Table C.12: X-ray point source list of all detections in the pn camera in dataset MB3, corresponding image and HR plots are found in figure 2.14. Continuation of Table C.11.

pn Sources in Dataset MB3													
Source ID	R.A. [J2000]	Dec. [J2000]	σ(pos) [″]	Flux [erg cm^{-2} s^{-1}]	σ(Flux) [erg cm^{-2} s^{-1}]	HR_1	$\sigma(HR_1)$	HR_2	$\sigma(HR_2)$	HR_3	$\sigma(HR_3)$	HR_4	$\sigma(HR_4)$
41	02 22 42.0	-73 42 25	2.06	1.00×10^{-14}	5.50×10^{-15}	0.601	0.249	0.011	0.233	-0.395	0.636	-1	0.636
42	02 25 43.3	-74 03 56	1.69	5.13×10^{-14}	2.49×10^{-14}	0.796	0.272	0.198	0.244	-0.299	0.339	0.34	0.339
43	02 24 40.2	-74 03 33	1.92	5.13×10^{-15}	3.72×10^{-15}	0.494	0.191	-0.731	0.195	-0.336	2.198	-1	2.198
44	02 25 27.7	-73 46 37	2	8.31×10^{-15}	9.08×10^{-15}	0.36	0.364	0.261	0.266	-0.305	1.245	-1	1.245
45	02 21 52.6	-73 50 59	2.28	5.00×10^{-14}	1.76×10^{-14}	1	1.323	0.634	0.393	0.003	0.25	0.39	0.25
46	02 21 52.0	-73 54 17	2.11	1.19×10^{-14}	9.35×10^{-15}	0.742	0.287	-0.392	0.241	-0.333	0.713	0.164	0.713
47	02 24 19.7	-73 59 41	1.97	1.88×10^{-14}	8.50×10^{-15}	0.733	0.229	-0.532	0.262	-0.407	0.31	0.737	0.31
48	02 26 04.2	-74 01 42	1.89	3.66×10^{-14}	2.29×10^{-14}	0.2	0.329	0.216	0.259	-0.438	0.459	0.415	0.459
49	02 25 31.0	-73 41 50	1.89	7.63×10^{-14}	5.06×10^{-14}	0.05	0.247	-0.984	0.264	-1	0.064	1	0.064
50	02 22 43.8	-73 52 32	2.22	1.60×10^{-14}	7.05×10^{-15}	1	0.892	0.474	0.47	0.184	0.356	-0.101	0.356
51	02 23 17.8	-73 58 55	1.64	2.42×10^{-14}	8.45×10^{-15}	0.506	0.378	-0.146	0.319	-0.028	0.265	0.422	0.265
52	02 25 56.0	-73 51 00	2.03	1.09×10^{-14}	8.63×10^{-15}	0.729	0.293	-0.387	0.286	-0.093	0.827	-0.27	0.827
53	02 26 55.2	-73 56 12	2.78	1.00×10^{-14}	1.57×10^{-14}	1	0.959	0.745	0.219	-0.734	2.684	-0.73	2.684
54	02 24 56.3	-73 57 10	1.89	2.21×10^{-14}	8.25×10^{-15}	1	0.688	0.623	0.358	0.103	0.305	0.027	0.305
55	02 26 56.1	-73 55 15	3.37	6.06×10^{-14}	3.33×10^{-14}	0.81	0.244	-0.856	0.233	0.679	0.331	0.483	0.331
56	02 22 47.1	-73 46 12	2.4	1.36×10^{-14}	9.93×10^{-15}	0.994	0.21	0.298	0.265	-0.295	0.701	-0.323	0.701
57	02 22 52.3	-73 43 28	2.1	2.23×10^{-14}	2.09×10^{-14}	0.643	0.609	0.732	0.192	-0.826	0.964	0.28	0.964
58	02 23 01.8	-73 46 18	2.44	5.00×10^{-15}	3.74×10^{-15}	0.873	0.32	0.255	0.261	-0.536	1.03	-1	1.03
59	02 26 15.8	-73 52 02	2.57	1.97×10^{-14}	1.60×10^{-14}	-1	>10	1	0.146	-0.181	0.68	-0.23	0.68
60	02 27 07.2	-73 49 14	3.24	1.96×10^{-14}	2.85×10^{-14}	1	>10	0.751	0.878	0.79	0.882	-1	0.882
61	02 26 15.6	-73 59 30	2.51	9.39×10^{-15}	8.64×10^{-15}	0.022	0.341	-0.153	0.352	0.155	0.869	-0.924	0.869
62	02 26 17.3	-74 02 03	2.15	7.68×10^{-14}	5.77×10^{-14}	0.366	0.458	0.339	0.297	-0.801	0.342	0.795	0.342
63	02 24 02.2	-73 49 36	1.74	4.65×10^{-15}	2.77×10^{-15}	-0.325	0.312	0.23	0.348	-0.167	0.618	-0.917	0.618

Appendix D

Calculating Signal-to-Noise

Following the IRAF Reduction Guide by Titus and Woudt (2018), the signal-to-noise ratio (SNR) of a spectrum may be extracted by taking the spectrum counts and dividing by the standard deviation of the signal. Since the counts and standard deviation of the incoming signal is wavelength dependent, a SNR per wavelength graph must be created.

A FITS file not only contains the background subtracted spectrum, but also contains other information, such as the sky background and standard deviation of the spectrum which are retained through the reduction process. These can be accessed by appending [*,1,x] to the filename within IRAF, where x ranges from 1 to 4. For the background subtracted spectrum, $x = 1$, and for the standard deviation of the signal, $x = 4$.

Thus in order to obtain a signal-to-noise graph, the IRAF command `sarith` is used, which will divide the spectrum by the standard deviation. The following command is used:

```
> sarith input.fits[*,1,1] / input.fits[*,1,4] output.fits
```

Where `input.fits[*,1,1]` is the back-ground subtracted spectrum, `input.fits[*,1,4]` contains the standard deviation per wavelength, and `output.fits` is the SNR file that is wavelength dependent.

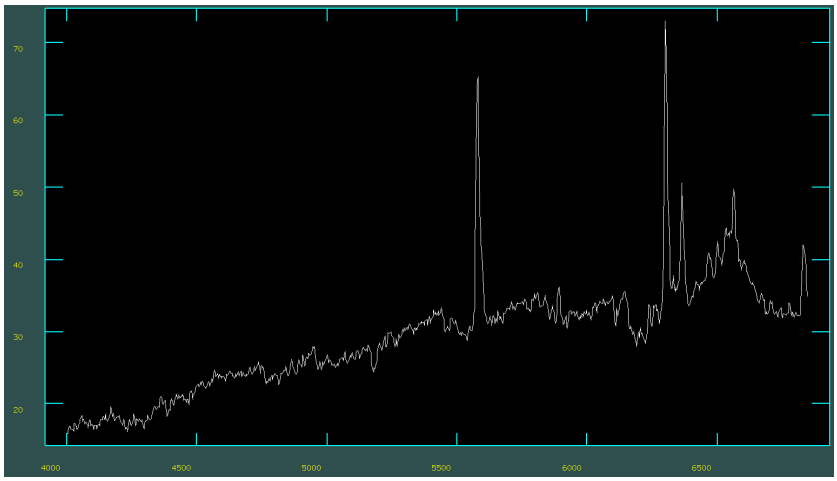

Figure D.1: Standard deviation of object 5355, the associated spectrum can be found in figure 3.1.

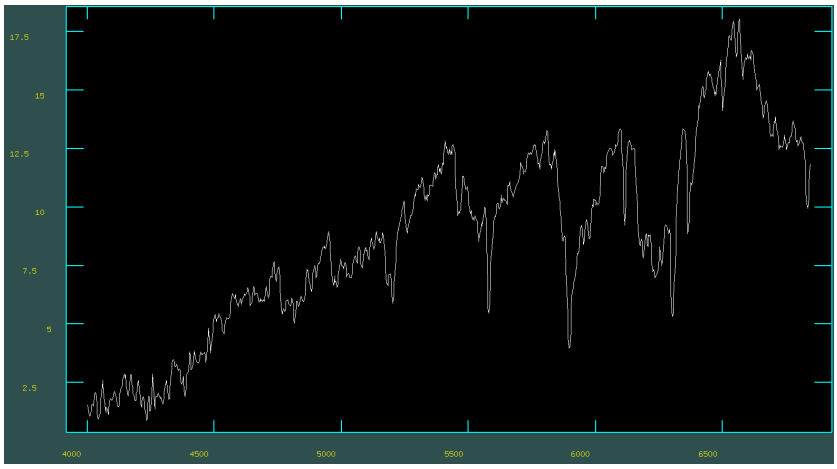

Figure D.2: SNR graph of object 5355, this was obtained by dividing figure 3.1 by the standard deviation, figure D.1, using the `sarith` command, as explained earlier.

The average SNR FITS file is converted to a text file which may then be read into Python. Using the `numpy` module, the SNR text file is averaged over all wavelengths, this is the final value quoted for each spectrum within chapter 3. The standard deviation of all SNR values are also included since the SNR of some spectra can vary by large degrees, such as in figure D.2.

Bibliography

K. Bekki and S. Stanimirović. The total mass and dark halo properties of the Small Magellanic Cloud. *Monthly Notices of the Royal Astronomical Society*, 395(1):342–350, May 2009. doi: 10.1111/j.1365-2966.2009.14514.x.

M. S. Bessell. Standard Photometric Systems. *Annual Review of Astronomy and Astrophysics*, 43(1):293–336, Sep 2005. doi: 10.1146/annurev.astro.41.082801.100251.

E. L. D. Bica and H. R. Schmitt. A Revised and Extended Catalog of Magellanic System Clusters, Associations, and Emission Nebulae. I. Small Magellanic Cloud and Bridge. *The Astrophysical Journal Supplement Series*, 101:41, Nov 1995. doi: 10.1086/192233.

R. Blandford, D. Meier, and A. Readhead. Relativistic Jets from Active Galactic Nuclei. *Annual Review of Astronomy and Astrophysics*, 57:467–509, August 2019. doi: 10.1146/annurev-astro-081817-051948.

R. Cayrel. Data Analysis. In G. Cayrel de Strobel and Monique Spite, editors, *The Impact of Very High S/N Spectroscopy on Stellar Physics*, volume 132 of *IAU Symposium*, page 345, Jan 1988.

S. Choudhury, A. Subramaniam, and A. A. Cole. Photometric metallicity map of the Large Magellanic Cloud. *Monthly Notices of the Royal Astronomical Society*, 455(2):1855–1880, Jan 2016. doi: 10.1093/mnras/stv2414.

S. Choudhury, A. Subramaniam, A. A. Cole, and Y. J. Sohn. Photometric metallicity map of the Small Magellanic Cloud. *Monthly Notices of the Royal Astronomical Society*, 475(4):4279–4297, Apr 2018. doi: 10.1093/mnras/sty087.

M. J. Coe. Be stars in X-ray binary systems. In Myron A. Smith, Huib F. Henrichs, and Juan Fabregat, editors, *IAU Colloq. 175: The Be Phenomenon in Early-Type Stars*, volume 214 of *Astronomical Society of the Pacific Conference Series*, page 656, January 2000.

M. J. Coe, W. R. T. Edge, J. L. Galache, and V. A. McBride. Optical properties of Small Magellanic Cloud X-ray binaries. *Monthly Notices of the Royal Astronomical Society*, 356(2):502–514, Jan 2005. doi: 10.1111/j.1365-2966.2004.08467.x.

M. J. Coe, V. A. McBride, A. J. Bird, and R. H. D. Corbet. Discovery of a new HMXB in the Magellanic Bridge. *The Astronomer's Telegram*, 1882: 1, Dec 2008.

M. J. Coe, R. H. D. Corbet, K. E. McGowan, V. A. McBride, M. P. E. Schurch, L. J. Townsend, J. L. Galache, I. Negueruela, and D. Buckley. Optical properties of High-Mass X-ray Binaries (HMXBs) in the Small Magellanic Cloud. In Jacco Th. Van Loon and Joana M. Oliveira, editors, *The Magellanic System: Stars, Gas, and Galaxies*, volume 256 of *IAU Symposium*, pages 367–372, Mar 2009. doi: 10.1017/S174392130802872X.

G. de Vaucouleurs and K. C. Freeman. Structure and dynamics of barred spiral galaxies, in particular of the Magellanic type. *Vistas in Astronomy*, 14(1):163–294, Jan 1972. doi: 10.1016/0083-6656(72)90026-8.

DENIS Consortium. VizieR Online Data Catalog: The DENIS database (DENIS Consortium, 2005). *VizieR Online Data Catalog*, art. II/263, September 2005.

D. Erkal, V. Belokurov, C. F. P. Laporte, S. E. Koposov, T. S. Li, C. J. Grillmair, N. Kallivayalil, A. M. Price-Whelan, N. W. Evans, and K. Hawkins. The total mass of the Large Magellanic Cloud from its perturbation on the Orphan stream. *Monthly Notices of the Royal Astronomical Society*, 487 (2):2685–2700, Aug 2019. doi: 10.1093/mnras/stz1371.

European Space Agency. What is SAS, a. URL `https://www.cosmos.esa.int/web/xmm-newton/what-is-sas`. Accessed: 2020-06-23.

European Space Agency. Science analysis system, b. URL `https://www.cosmos.esa.int/web/xmm-newton/sas-download`. Accessed: 2020-06-24.

European Space Agency. How to filter EPIC event lists for flaring particle background, c. URL `https://www.cosmos.esa.int/web/xmm-newton/sas-thread-epic-filterbackground`. Accessed: 2020-06-24.

European Space Agency. Science analysis system start-up, d. URL `https://www.cosmos.esa.int/web/xmm-newton/sas-thread-startup`. Accessed: 2020-06-24.

European Space Agency. Science analysis system threads, e. URL `https://www.cosmos.esa.int/web/xmm-newton/sas-threads`. Accessed: 2020-06-24.

European Space Agency. XMM newton overview, f. URL `https://www.esa.int/Science_Exploration/Space_Science/XMM-Newton_overview`. Accessed: 2020-06-23.

European Space Agency. XMM-newton science archive, g. URL `nxsa.esac.esa.int/nxsa-web`. Accessed: 2020-06-24.

European Space Agency. XMM newton fact sheet, h. URL `http://sci.esa.int/xmm-newton/47370-fact-sheet/`. Accessed: 2020-06-23.

C. J. Evans, I. D. Howarth, M. J. Irwin, A. W. Burnley, and T. J. Harries. A 2dF survey of the Small Magellanic Cloud. *Monthly Notices of the Royal Astronomical Society*, 353(2):601–623, Sep 2004. doi: 10.1111/j.1365-2966.2004.08096.x.

L. W. Frederick, M. R. Myers, B. Berman, D. W. Jenkins, E. R. Schmerling, A. W. Schardt, A. G. Opp, R. Horowitz, R. F. Fellows, H. F. Hipsher, L. S. Walter, Jr. Lowman, P. D., P. J. Dickerman, E. Thornton, and H. Glaser. *Significant Achievements in Solar Physics*. 1966.

L. T. Gardiner and M. Noguchi. N-body simulations of the Small Magellanic Cloud and the Magellanic Stream. *Monthly Notices of the Royal Astronomical Society*, 278(1):191–208, Jan 1996. doi: 10.1093/mnras/278.1.191.

A. Georgakakis, P. Pérez-González, N. Fanidakis, J. Salvato, Mara, J. Aird, H. Messias, J. Lotz, G. Barro, Li-Ting Hsu, K. Nandra, Dalton Rosario, M. Cooper, D. Kocevski, and J. Newman. Investigating evidence for different black hole accretion modes since redshift z 1. *Monthly Notices of the Royal Astronomical Society*, 440, 02 2014. doi: 10.1093/mnras/stu236.

R. Giacconi, H. Gursky, F. R. Paolini, and B. B. Rossi. Evidence for x Rays From Sources Outside the Solar System. *Physical Review Letters*, 9(11):439–443, Dec 1962. doi: 10.1103/PhysRevLett.9.439.

C. Grant. CCDs for X-ray Astronomy, 2007. URL `https://www.astro.umd.edu/~richard/ASTR680/grant_ccds.pdf`.

S. A. Grebenev, A. A. Lutovinov, S. S. Tsygankov, and I. A. Mereminskiy. Deep hard X-ray survey of the Large Magellanic Cloud. *Monthly Notices of the Royal Astronomical Society*, 428(1):50–57, Jan 2013. doi: 10.1093/mnras/sts008.

H. J. Grimm, M. Gilfanov, and R. Sunyaev. X-ray binaries in the Milky

Way and other galaxies. *Chinese Journal of Astronomy and Astrophysics Supplement*, 3:257–269, Dec 2003a. doi: 10.1088/1009-9271/3/S1/257.

H. J. Grimm, M. Gilfanov, and R. Sunyaev. High-mass X-ray binaries as a star formation rate indicator in distant galaxies. *Monthly Notices of the Royal Astronomical Society*, 339(3):793–809, Mar 2003b. doi: 10.1046/j.1365-8711.2003.06224.x.

M. Gudel. Radio and X-ray emission from main-sequence K stars. *Astronomy and Astrophysics*, 264:L31–L34, Oct 1992.

M. Güdel, J. A. Bookbinder, J. H. M. M. Schmitt, and T. A. Fleming. *Correlation between Radio and X-ray Luminosities among Late-Type Stars: A ROSAT-VLA Survey of M Dwarfs*, volume 183 of *Astrophysics and Space Science Library*, page 383. 1993. doi: 10.1007/978-94-011-1964-1_52.

F. Haberl and R. Sturm. High-mass X-ray binaries in the Small Magellanic Cloud. *Astronomy and Astrophysics*, 586:A81, February 2016. doi: 10.1051/0004-6361/201527326.

J. Harris. The Magellanic Bridge: The Nearest Purely Tidal Stellar Population. *The Astrophysical Journal*, 658(1):345–357, Mar 2007. doi: 10.1086/511816.

J. Harris and D. Zaritsky. The Star Formation History of the Small Magellanic Cloud. *The Astronomical Journal*, 127(3):1531–1544, Mar 2004. doi: 10.1086/381953.

J. Harris and D. Zaritsky. The Star Formation History of the Large Magellanic Cloud. *The Astronomical Journal*, 138(5):1243–1260, Nov 2009. doi: 10.1088/0004-6256/138/5/1243.

R. W. Hilditch, I. D. Howarth, and T. J. Harries. Forty eclipsing binaries in the Small Magellanic Cloud: fundamental parameters and Cloud distance.

Monthly Notices of the Royal Astronomical Society, 357(1):304–324, Feb 2005. doi: 10.1111/j.1365-2966.2005.08653.x.

J. V. Hindman, R. X. McGee, A. W. L. Carter, E. C. J. Holmes, and M. Beard. A Low Resolution Hydrogen-line Survey of the Magellanic System. I. Observations and Digital Reduction Procedures. *Australian Journal of Physics*, 16:552, Jan 1963. doi: 10.1071/PH630552.

M. J. Irwin, W. E. Kunkel, and S. Demers. A blue stellar population in the HI bridge between the two Magellanic Clouds. *Nature*, 318(6042):160–161, Nov 1985. doi: 10.1038/318160a0.

P. Kahabka and M. Hilker. Discovery of an X-ray binary in the outer SMC wing. *Astronomy and Astrophysics*, 435(1):9–16, May 2005. doi: 10.1051/0004-6361:20042408.

S. Lépine and E. Gaidos. An All-sky Catalog of Bright M Dwarfs. *The Astronomical Journal*, 142(4):138, October 2011. doi: 10.1088/0004-6256/142/4/138.

W. H. G. Lewin, J. van Paradijs, and E. P. J. van Den Heuvel. *X-ray Binaries*. Cambridge University Press, 1997. ISBN 9780521599344.

D. H. Lumb, N. Schartel, and F. A. Jansen. X-ray Multi-mirror Mission (XMM-Newton) observatory. *Optical Engineering*, 51(1):011009-011009-11, Jan 2012. doi: 10.1117/1.OE.51.1.011009. URL `https://arxiv.org/pdf/1202.1651.pdf`.

L. Macri. FITS Reduction Script for the South African Astronomical Observatory (SAAO) 1.9 m Telescope & CCDSpec, Aug 2016.

M. Massi. Active Galaxies, Nov 2013. URL `https://www3.mpifr-bonn.mpg.de/staff/mmassi/QUASARS1small.pdf`.

V. A. McBride, M. J. Coe, I. Negueruela, M. P. E. Schurch, and K. E. McGowan. Spectral distribution of Be/X-ray binaries in the Small Magellanic Cloud. *Monthly Notices of the Royal Astronomical Society*, 388(3):1198–1204, Aug 2008. doi: 10.1111/j.1365-2966.2008.13410.x.

V. A. McBride, A. J. Bird, M. J. Coe, L. J. Townsend, R. H. D. Corbet, and F. Haberl. The Magellanic Bridge: evidence for a population of X-ray binaries. *Monthly Notices of the Royal Astronomical Society*, 403(2): 709–713, Apr 2010. doi: 10.1111/j.1365-2966.2009.16178.x.

A. W. McConnachie. The Observed Properties of Dwarf Galaxies in and around the Local Group. *The Astronomical Journal*, 144(1):4, Jul 2012. doi: 10.1088/0004-6256/144/1/4.

A. W. McConnachie, M. J. Irwin, A. M. N. Ferguson, R. A. Ibata, G. F. Lewis, and N. Tanvir. Distances and metallicities for 17 Local Group galaxies. *Monthly Notices of the Royal Astronomical Society*, 356(3):979–997, 01 2005. ISSN 0035-8711. doi: 10.1111/j.1365-2966.2004.08514.x. URL `https://doi.org/10.1111/j.1365-2966.2004.08514.x`.

S. J. Meatheringham, M. A. Dopita, H. C. Ford, and B. Louise Webster. The Kinematics of the Planetary Nebulae in the Large Magellanic Cloud. *The Astrophysical Journal*, 327:651, Apr 1988. doi: 10.1086/166222.

D. J. Mink and M. J. Kurtz. RVSAO 2.0 - A Radial Velocity Package for IRAF. In Rudolf Albrecht, Richard N. Hook, and Howard A. Bushouse, editors, *Astronomical Data Analysis Software and Systems VII*, volume 145 of *Astronomical Society of the Pacific Conference Series*, page 93, Jan 1998.

N. Mizuno, E. Muller, H. Maeda, A. Kawamura, T. Minamidani, T. Onishi, A. Mizuno, and Y. Fukui. Detection of Molecular Clouds in the Magellanic Bridge: Candidate Star Formation Sites in a Nearby Low-Metallicity

System. *Astrophysical Journal, Letters*, 643(2):L107–L110, Jun 2006. doi: 10.1086/505298.

D. G. Monet. The 526,280,881 Objects In The USNO-A2.0 Catalog. In *American Astronomical Society Meeting Abstracts*, volume 193 of *American Astronomical Society Meeting Abstracts*, page 120.03, Dec 1998.

W. W. Morgan, P. C. Keenan, and E. Kellman. *An atlas of stellar spectra, with an outline of spectral classification*. 1943.

E. Muller and Q. A. Parker. Hα Emission from the Magellanic Bridge. *Publications of the Astronomical Society of Australia*, 24(2):69–76, Jul 2007. doi: 10.1071/AS07010.

NASA/IPAC Extragalactic Database. Iii zw 002 information. URL `https://ned.ipac.caltech.edu/cgi-bin/objsearch?objname=III+Zw+2&extend=no&out_csys=Equatorial&out_equinox=J2000.0&obj_sort=RA+or+Longitude&zv_breaker=30000.0&list_limit=5&img_stamp=YES`. Accessed: 2020-07-07.

National Aeronautics and Space Administration. HEASOFT software, a. URL `https://heasarc.gsfc.nasa.gov/lheasoft/download.html`. Accessed: 2020-06-24.

National Aeronautics and Space Administration. Xspec: An x-ray spectral fitting package, b. URL `https://heasarc.gsfc.nasa.gov/xanadu/xspec/`. Accessed: 2020-07-07.

Y. Nazé, P. S. Broos, L. Oskinova, L. K. Townsley, D. Cohen, M. F. Corcoran, N. R. Evans, M. Gagné, A. F. J. Moffat, J. M. Pittard, G. Rauw, A. ud-Doula, and N. R. Walborn. Global X-ray Properties of the O and B Stars in Carina. *The Astrophysical Journal Supplement Series*, 194(1):7, May 2011. doi: 10.1088/0067-0049/194/1/7.

G. Neugebauer, J. B. Oke, E. E. Becklin, and K. Matthews. Absolute spectral energy distribution of quasi-stellar objects from 0.3 to 10 microns. *The Astrophysical Journal*, 230:79–94, May 1979. doi: 10.1086/157063.

A. T. Okazaki, K. Hayasaki, and Y. Moritani. Origin of Two Types of X-Ray Outbursts in Be/X-Ray Binaries. I. Accretion Scenarios. *Publications of the Astronomical Society of Japan*, 65:41, Apr 2013. doi: 10.1093/pasj/65.2.41.

D. E. Osterbrock. The luminosity function of Seyfert galaxies and the cluster 3C 295. *Astrophysical Journal, Letters*, 280:L43–L45, May 1984. doi: 10.1086/184266.

S. A. Pardy, E. D'Onghia, E. Athanassoula, E. M. Wilcots, and K. Sheth. Tidally Induced Offset Disks in Magellanic Spiral Galaxies. *The Astrophysical Journal*, 827(2):149, Aug 2016. doi: 10.3847/0004-637X/827/2/149.

T. Park, Vinay L. Kashyap, A. Siemiginowska, D. A. van Dyk, A. Zezas, C. Heinke, and B. J. Wargelin. Bayesian Estimation of Hardness Ratios: Modeling and Computations. *The Astrophysical Journal*, 652(1):610–628, Nov 2006. doi: 10.1086/507406.

J. L. Payne, M. D. Filipović, W. Reid, P. A. Jones, L. Staveley-Smith, and G. L. White. An ATCA radio-continuum study of the Small Magellanic Cloud - II. Source identification and classification. *Monthly Notices of the Royal Astronomical Society*, 355(1):44–50, November 2004. doi: 10.1111/j.1365-2966.2004.08287.x.

A. J. Pickles. A Stellar Spectral Flux Library: 1150-25000 Å. *The Publications of the Astronomical Society of the Pacific*, 110(749):863–878, Jul 1998. doi: 10.1086/316197.

G. Pietrzyński, D. Graczyk, W. Gieren, I. B. Thompson, B. Pilecki, A. Udalski, I. Soszyński, S. Kozłowski, P. Konorski, and K. Suchomska. An

eclipsing-binary distance to the Large Magellanic Cloud accurate to two per cent. *Nature*, 495(7439):76–79, Mar 2013. doi: 10.1038/nature11878.

M. E. Putman, L. Staveley-Smith, K. C. Freeman, B. K. Gibson, and D. G. Barnes. The Magellanic Stream, High-Velocity Clouds, and the Sculptor Group. *The Astrophysical Journal*, 586(1):170–194, Mar 2003. doi: 10.1086/344477.

S. Rappaport and E. P. J. van den Heuvel. X-ray observations of Be stars. In M. Jaschek and H. G. Groth, editors, *Be Stars*, volume 98 of *IAU Symposium*, pages 327–344, April 1982.

W. Röntgen. On a New Kind of Rays. *Nature*, 53(1369):274–276, Jan 1896. doi: 10.1038/053274b0.

S. R. Rosen, N. A. Webb, M. G. Watson, J. Ballet, D. Barret, V. Braito, F. J. Carrera, M. T. Ceballos, M. Coriat, and R. Della Ceca. VizieR Online Data Catalog: XMM-Newton Serendipitous Source Catalogue 3XMM-DR6 (XMM-SSC, 2016). *VizieR Online Data Catalog*, art. IX/50, Sep 2016.

R. A. Schommer, N. B. Suntzeff, E. W. Olszewski, and H. C. Harris. Spectroscopy of Giants in LMC Clusters. II Kinematics of the Cluster Sample. *The Astronomical Journal*, 103:447, Feb 1992. doi: 10.1086/116074.

V. Singh, P. Shastri, and G. Risaliti. X-ray spectral properties of Seyfert galaxies and the unification scheme. *Astronomy and Astrophysics*, 532: A84, Aug 2011. doi: 10.1051/0004-6361/201016387.

D. M. Skowron, A. M. Jacyszyn, A. Udalski, M. K. Szymański, J. Skowron, R. Poleski, S. Kozłowski, M. Kubiak, G. Pietrzyński, and I. Soszyński. OGLE-ING the Magellanic System: Stellar Populations in the Magellanic Bridge. *The Astrophysical Journal*, 795(2):108, Nov 2014. doi: 10.1088/0004-637X/795/2/108.

Sloan Digital Sky Survey. Spectral cross-correlation templates. URL `http://classic.sdss.org/dr5/algorithms/spectemplates/`. Accessed: 2020-06-24.

South African Astronomical Observatory. SpUpNIC user manual. URL `https://topswiki.saao.ac.za/index.php/SPUPNIC`. Accessed: 2020-06-24.

S. Stanimirovic, L. Staveley-Smith, J. M. Dickey, R. J. Sault, and S. L. Snowden. The large-scale HI structure of the Small Magellanic Cloud. *Monthly Notices of the Royal Astronomical Society*, 302(3):417–436, January 1999. doi: 10.1046/j.1365-8711.1999.02013.x.

R. Sturm, F. Haberl, W. Pietsch, J. Ballet, D. Hatzidimitriou, D. A. H. Buckley, M. Coe, M. Ehle, M. D. Filipović, and N. La Palombara. The XMM-Newton survey of the Small Magellanic Cloud: The X-ray point-source catalogue. *Astronomy and Astrophysics*, 558:A3, Oct 2013. doi: 10.1051/0004-6361/201219935.

J. R. Thorstensen, W. H. Fenton, and C. J. Taylor. Spectroscopy of Seven Cataclysmic Variables with Periods above 5 Hours. *The Publications of the Astronomical Society of the Pacific*, 116(818):300–310, Apr 2004. doi: 10.1086/382792.

N. Titus and P. Woudt. IRAF Reduction Guide, Apr 2018.

L. J. Townsend, M. J. Coe, R. H. D. Corbet, V. A. McBride, A. B. Hill, A. J. Bird, M. P. E. Schurch, F. Haberl, R. Sturm, D. Pathak, B. van Soelen, E. S. Bartlett, S. P. Drave, and A. Udalski. The orbital solution and spectral classification of the high-mass X-ray binary IGR J01054-7253 in the Small Magellanic Cloud. *Monthly Notices of the Royal Astronomical Society*, 410(3):1813–1824, Jan 2011. doi: 10.1111/j.1365-2966.2010.17563.x.

J. Trümper, G. Hasinger, B. Aschenbach, H. Bräuninger, U. G. Briel, W. Burkert, H. Fink, E. Pfeffermann, W. Pietsch, P. Predehl, J. H. M. M. Schmitt, W. Voges, U. Zimmermann, and K. Beuermann. X-ray survey of the Large Magellanic Cloud by ROSAT. *Nature*, 349(6310):579–583, Feb 1991. doi: 10.1038/349579a0.

University of Strasbourg. Aladin sky atlas. URL `aladin.u-strasbg.fr/`. Accessed: 2020-06-24.

C. Urry. AGN Unification: An Update. In Gordon T. Richards and Patrick B. Hall, editors, *AGN Physics with the Sloan Digital Sky Survey*, volume 311 of *Astronomical Society of the Pacific Conference Series*, page 49, June 2004.

E. P. J. van den Heuvel. Formation and evolution of X-ray binaries. In W. H. G. Lewin and E. P. J. van den Heuvel, editors, *Accretion-Driven Stellar X-ray Sources*, pages 303–341, January 1983.

P. G. van Dokkum. Cosmic-Ray Rejection by Laplacian Edge Detection. *The Publications of the Astronomical Society of the Pacific*, 113(789):1420–1427, Nov 2001. doi: 10.1086/323894.

G. Vasilopoulos, P. Maggi, F. Haberl, R. Sturm, W. Pietsch, E. S. Bartlett, and M. J. Coe. Swift J053041.9-665426, a new Be/X-ray binary pulsar in the Large Magellanic Cloud. *Astronomy and Astrophysics*, 558:A74, October 2013. doi: 10.1051/0004-6361/201322335.

F. Verbunt and E. P. J. van den Heuvel. Formation and evolution of neutron stars and black holes in binaries. In *X-ray Binaries*, pages 457–494, January 1995.

J. Vink. Supernova remnants: the X-ray perspective. *Astronomy and Astrophysics Reviews*, 20:49, December 2012. doi: 10.1007/s00159-011-0049-1.

M. Wade. Aerobee, 1997-2019. URL `http://www.astronautix.com/a/aerobee.html`.

R. Walker. *Spectral Atlas for Amateur Astronomers: A Guide to the Spectra of Astronomical Objects and Terrestrial Light Sources*. Cambridge University Press, 2018. ISBN 1107165903.

W. Wegner. Absolute magnitudes of OB and Be stars based on Hipparcos parallaxes - II. *Monthly Notices of the Royal Astronomical Society*, 371: 185–192, 2006.

R. M. Williams and Y. H. Chu. Supernova Remnants in the Magellanic Clouds. VI. The DEM L316 Supernova Remnants. *The Astrophysical Journal*, 635(2):1077–1086, Dec 2005. doi: 10.1086/497681.

XMM-Newton Science Operations Centre. EPIC event grade selection, a. URL `http://xmm-tools.cosmos.esa.int/external/xmm_user_support/documentation/uhb/epic_evgrades.html`. Accessed: 2020-06-23.

XMM-Newton Science Operations Centre. Pile-up, b. URL `https://heasarc.gsfc.nasa.gov/docs/xmm/sas/USG/epicpileup.html`. Accessed: 2020-06-23.

N. Zacharias, D. G. Monet, S. E. Levine, S. E. Urban, R. Gaume, and G. L. Wycoff. VizieR Online Data Catalog: NOMAD Catalog (Zacharias+ 2005). *VizieR Online Data Catalog*, art. I/297, Nov 2005.

S. A. Zhekov and F. Palla. X-rays from massive OB stars: thermal emission from radiative shocks. *Monthly Notices of the Royal Astronomical Society*, 382(3):1124–1132, December 2007. doi: 10.1111/j.1365-2966.2007.12286.x.